

VLA-ANGST: A high-resolution H I Survey of Nearby Dwarf Galaxies

Jürgen Ott

National Radio Astronomy Observatory, P.O. Box O, 1003 Lopezville Road, Socorro, NM
87801, USA

`jott@nrao.edu`

Adrienne M. Stilp

Department of Astronomy, Box 351580, University of Washington, Seattle, WA 98195, USA

`adrienne@astro.washington.edu`

Steven R. Warren

Minnesota Institute for Astrophysics, University of Minnesota, 116 Church St. SE,
Minneapolis, MN 55455, USA

`warren@astro.umn.edu`

Evan D. Skillman

Minnesota Institute for Astrophysics, University of Minnesota, 116 Church St. SE,
Minneapolis, MN 55455, USA

`skillman@astro.umn.edu`

Julianne J. Dalcanton

Department of Astronomy, Box 351580, University of Washington, Seattle, WA 98195, USA

`jd@astro.washington.edu`

Fabian Walter

Max-Planck-Institut für Astronomie, Königstuhl 17, D-69117 Heidelberg, Germany

`walter@mpia.de`

W.J.G. de Blok

Netherlands Institute for Radio Astronomy, Oude Hoogeveensedijk 4, 7991 PD Dwingeloo,
The Netherlands

`blok@astron.nl`

Bärbel Koribalski

Australia Telescope National Facility, CSIRO Astronomy and Space Science, PO Box 76,
Epping NSW 1710, Australia

`Baerbel.Koribalski@csiro.au`

and

Andrew A. West

Department of Astronomy, Boston University, 725 Commonwealth Avenue, Boston, MA
02215, USA

`aawest@bu.edu`

Received _____; accepted _____

ABSTRACT

We present the “Very Large Array survey of Advanced Camera for Surveys Nearby Galaxy Survey Treasury galaxies (VLA-ANGST).” VLA-ANGST is a National Radio Astronomy Observatory Large Program consisting of high spectral ($0.6 - 2.6 \text{ km s}^{-1}$) and spatial ($\sim 6''$) resolution observations of neutral, atomic hydrogen (H I) emission toward 35 nearby dwarf galaxies from the ANGST survey. ANGST is a systematic Hubble Space Telescope survey to establish a legacy of uniform multi-color photometry of resolved stars for a volume-limited sample of nearby galaxies ($D \lesssim 4 \text{ Mpc}$). VLA-ANGST provides VLA H I observations of the sub-sample of ANGST galaxies with recent star formation that are observable from the northern hemisphere and that were not observed in the “The H I Nearby Galaxy Survey” (THINGS). The overarching scientific goal of VLA-ANGST is to investigate fundamental characteristics of the neutral interstellar medium (ISM) of dwarf galaxies. Here we describe the VLA observations, the data reduction, and the final VLA-ANGST data products. We present an atlas of the integrated H I maps, the intensity-weighted velocity fields, the second moment maps as a measure for the velocity dispersion of the H I, individual channel maps, and integrated H I spectra for each VLA-ANGST galaxy. We closely follow the observational setup and data reduction of THINGS to achieve comparable sensitivity and angular resolution. A major difference between VLA-ANGST and THINGS, however, is the high velocity resolution of the VLA-ANGST observations (0.65 and 1.3 km s^{-1} for the majority of the galaxies). The VLA-ANGST data products are made publicly available through a dedicated webpage¹. With available star formation histories from resolved stellar populations and lower resolution

¹<https://science.nrao.edu/science/surveys/vla-angst>

ancillary observations from the far infrared to the ultraviolet, VLA-ANGST will enable detailed studies of the relationship between the ISM and star formation in dwarf galaxies on a ~ 100 pc scale.

Subject headings: galaxies: ISM — galaxies: structure — galaxies: irregular — ISM: atoms — radio lines: galaxies — surveys — galaxies: dwarf — galaxies: individual(NGC 247, DDO 6, NGC 404, KKH 37, UGC 4483, KK 77, BK 3N, AO 0952+69, Sextans B, NGC 3109, Antlia, KDG 63, Sextans A, HS 117, DDO 82, KDG 73, NGC 3741, DDO 99, NGC 4163, NGC 4190, DDO 113, MCG +09-20-131, DDO 125, UGCA 292, GR 8, UGC 8508, DDO 181, DDO 183, KKH 86, UGC 8833, KK 230, DDO 187, DDO 190, KKR 25, KKH 98)

NGC 247 DDO 6 NGC 404 KKH 37 UGC 4483 KK 77 BK 3N AO 0952+69 Sextans B
 NGC 3109 Antlia KDG 63 Sextans A HS 117 DDO 82 KDG 73 NGC 3741 DDO 99 NGC
 4163 NGC 4190 DDO 113 MCG +09-20-131 DDO 125 UGCA 292 GR 8 UGC 8508 DDO
 181 DDO 183 KKH 86 UGC 8833 KK 230 DDO 187 DDO 190 KKR 25 KKH 98

1. Introduction

Star formation is driven by complicated interactions between gas and stars. Untangling the interplay between these processes is difficult, because in most cases, the events that trigger star formation are not obvious, nor are those that shape the structure and dynamics of the ISM. For a full understanding it is therefore indispensable to obtain a comprehensive view of all processes that come together to form stars, stellar associations, and stellar clusters. Observationally, one requires knowledge of the gas distribution and kinematics as well as the stellar energy input into the ISM over time.

In recent years, large systematic surveys have made superb progress on the first of these requirements. The number of nearby galaxies for which high-quality H I data is available has dramatically increased in the last few years, including campaigns such as THINGS (“The H I Nearby Galaxy Survey”; Walter et al. 2008), FIGGS (“Faint Irregular Galaxies GMRT Survey”; Begum et al. 2008), LITTLE-THINGS (“LITTLE: Local Irregulars That Trace Luminosity Extremes”; Hunter et al. 2007), SHIELD (“Survey of H I in Extremely Low-mass Dwarfs”; Cannon et al. 2011), LVHIS (“The Local Volume H I Survey”; Koribalski 2008), WHISP (“Westerbork observations of neutral Hydrogen in Irregular and Spiral galaxies”; van der Hulst et al. 2001), and HALOGAS (“The Westerbork Hydrogen Accretion in Local Galaxies”; Heald et al. 2011). The difficult work of mapping the molecular medium in the brighter galaxies has begun as well, e.g. in BIMA SONG (“The BIMA Survey of Nearby Galaxies” Helfer et al. 2003), HERACLES, (“The HERA

CO Line Extragalactic Survey”; Leroy et al. 2009), and STING (“CARMA Survey Toward Infrared-bright Nearby Galaxies”; Rahman et al. 2012).

Unfortunately, the needed measurements of time-resolved stellar energy input are more difficult to acquire. Large systematic surveys in the far-ultraviolet (e.g., obtained with the *GALEX* telescope) and the far-infrared (e.g., the Local Volume Legacy survey (LVL; Dale et al. 2009), SINGS (“Spitzer Infrared Nearby Galaxies Survey”; Kennicutt et al. 2003), Kingfish (“Key Insights on Nearby Galaxies: a Far-Infrared Survey with Herschel”; Kennicutt et al. 2011), etc) have made excellent progress in measuring the recent star formation rate (SFR), while surveys like 11HUGS (“The 11 Mpc H α UV Galaxy Survey”; Lee et al. 2004) have provided the H α mapping needed to trace star formation (SF) on much shorter timescales. However, these approaches to measuring star formation lack all but the broadest time resolution, with the different tracers being sensitive to SF over different timescales. H α is emitted on the timescale of O-star lifetimes ($\lesssim 5$ Myr) and the far-ultraviolet on the timescale of A-star lifetimes ($\lesssim 100$ Myr). The far-infrared is sensitive to timescales similar to the $\lesssim 100$ Myr of far-ultraviolet heating. These timescales are not necessarily well-matched to the relevant energy input timescales for the gas.

For the survey presented here, we take a different approach, and focus H I observations on galaxies which are sufficiently close that their stellar populations can be resolved with the *Hubble Space Telescope* (HST). The resulting color–magnitude diagrams (CMDs) allow one to construct spatially-resolved star formation histories (SFHs) via analyses of galaxies’ stellar populations, and thus reveal the time-resolved SFR of these nearby galaxies over timescales of several hundred Myr at $\sim 5 - 10''$ spatial resolution (e.g., Dohm-Palmer et al. 2002; Cannon et al. 2003; Weisz et al. 2008; Williams et al. 2010; McQuinn et al. 2010; Crnojević et al. 2011; Cannon et al. 2011; Weisz et al. 2011). With nearly 300 orbits of *HST* time, one of the most ambitious programs to obtain spatially-resolved SFHs is the

ACS Nearby Galaxy Survey Treasury program (ANGST; Dalcanton et al. 2009). The ANGST observations enable to map spatially-resolved SFHs for a volume-limited sample of 69 nearby (< 4 Mpc) galaxies, probing both group and field environments. These data provide an entirely new, statistically significant view on the SFH of the local universe dwarf galaxy population.

The survey presented here, VLA-ANGST (“Very Large Array survey of ACS Nearby Galaxy Survey Treasury galaxies”), complements ANGST with high spatial and spectral resolution data cubes of the atomic gas traced by the 21 cm line of neutral atomic hydrogen (H I). VLA-ANGST was designed to aim for the best available resolution and sensitivity, using the NRAO Very Large Array (VLA) in multiple configurations in a Large Program worth ~ 500 hours of observing time to achieve that goal. VLA-ANGST is designed to match the H I spatial resolution ($\sim 6''$) to the cell sizes over which the SFHs can be determined. Furthermore, the majority of the VLA-ANGST galaxies were observed at very high spectral resolution of $0.6 - 1.3 \text{ km s}^{-1}$ which is important for detailed ISM dynamic modeling studies of the rather low-mass objects which dominate the galaxy population within 4 Mpc.

The VLA-ANGST survey has a number of features that make it a valuable addition to the many other H I surveys, beyond the existence of resolved stellar population data. First, the galaxies in VLA-ANGST are all quite close, which ensures high linear resolution for studying small-scale features in the H I distribution. Second, because care was taken to match the observational setups of THINGS, the VLA-ANGST survey can be readily combined with the THINGS survey, giving much broader coverage towards low galaxy masses. When further combined with surveys like LITTLE-THINGS and SHIELD, which have used a similar observational strategy, we will have a relatively uniform database of H I toward > 100 objects spanning a large variety of galaxy types that is comparable in terms

of sensitivity, angular, and spectral resolution.

The variety of galaxy types in the sample allows the study of (1) the response of gas and star formation to the propagation of spiral arms and to interactions, as seen in massive spirals and starburst galaxies (2) star formation propagation in the absence of strong perturbations of the gas density; gas rich dwarves are ideal for such a study due to their lack of internal shear and spiral density waves (3) star formation triggered in unusual kinematic environments such as in tidal dwarfs, and (4) dIrr/dSph transition-type galaxies, whose lack of current SF but ample gas reservoirs allow studies of galaxies that possess the raw material for star formation, but somehow remain dormant.

In the following we present the data of the VLA-ANGST survey, and in-depth scientific analyses will follow in subsequent publications. First analyses based on VLA-ANGST data cubes are provided by Warren et al. (2011) on the energy requirements of large H I holes, by Warren et al. (2012) on the distribution of cold and warm H I, and by Stilp et al. (2012) on the global H I velocity dispersion profiles correlated to the properties of the galaxies. Section 2 describes the selection of the targets, followed by the observational setup and data reduction (Section 3). Our data products are presented in Section 4 and a summary of the VLA-ANGST given in Section 5.

2. Target Selection

The ANGST survey targeted a complete volume-limited sample of 69 galaxies. The volume consists of those galaxies above a Galactic latitude of $|b| > 20^\circ$, outside the Local Group but within 3.5 Mpc, with additional cones out to 4 Mpc in the directions of the M81 and Sculptor groups. This volume provides a wide variety of gas-rich galaxies of all morphological types (Sb, dIrr, dSph/dE types, and tidal dwarfs), spanning a range

of 10 magnitudes in luminosity, 10^4 in current star formation rate (SFR), and 1.3 dex in metallicity.

To complement the ANGST HST data with interferometric H I observations, for VLA-ANGST we selected a sub-sample of ANGST targets that comprises galaxies with known H I content and galaxies with indications of recent star formation, even if H I was not previously detected by single dish observations. We excluded galaxies that are too far south for the VLA ($\delta < -30^\circ$) and galaxies that were previously covered by THINGS.

Due to the volume limited nature of ANGST, most of the objects that fit our selection criteria are rather low-mass, low-luminosity dwarf galaxies. An exception is the ANGST galaxy NGC 253, a massive barred starburst galaxy. The H I properties of NGC 253, in particular its large linewidth, are very different to the rest of our sample and can only be adequately observed with the new correlator capabilities of the upgraded Karl G. Jansky Very Large Array². Thus, we excluded the massive starburst galaxy NGC 253 from our sample. In total, the VLA-ANGST sample amounts to 35 galaxies, approximately half the objects that comprise the entire ANGST *HST* survey.

We list all VLA-ANGST galaxies and their basic properties in Table 1. Column (1) contains the galaxy names, and column (2) a range of alternative names as found on the “NASA/IPAC Extragalactic Database” (NED)³. Columns (3) and (4) are the central equatorial J2000 coordinates, followed by the distance D of the galaxies in column (derived using the tip of the red giant branch [TRGB] method) (5). The optical diameters at

²The “Very Large Array” was recently renamed to “The Karl G. Jansky Very Large Array (VLA)” to mark the end of the construction phase of the VLA upgrade. During construction, the project carried the name “Expanded Very Large Array” (EVLA).

³<http://ned.ipac.caltech.edu/>

$25 \text{ mag}''^2$ (D_{25}) surface brightness and the absolute B magnitudes M_B are listed in columns (6) and (7), respectively. Column (8) contains the galaxies' $3.6 \mu\text{m}$ infrared luminosities, which is a rough measure for the old, unobscured stellar population, followed by the morphological types in numerical code according to de Vaucouleurs et al. (1991) taken from Karachentsev et al. (2004) in column (9). Finally, we list the UV-based star formation rate in column (10).

In the VLA-ANGST sample, 29 galaxies are classified as T-type = 10, 2 as T-type = 9, 1 as T-type = 7, 1 as T-type = -3 , and 2 as T-type = -3 , where negative T-types are early type galaxies and positive T-types are late-type galaxies. Gas-rich irregulars are at the upper end of the -10 to 10 scale. Six galaxies were not detected in our H I observations. The two galaxies classified as T-type = -3 were non-detections, and the other 4 non-detections were T-type = 10. DDO 82 was a single dish H I non-detection but we detected the atomic hydrogen gas in VLA-ANGST.

Fig. 1 shows the distributions of VLA-ANGST galaxies as a function of distance, T-type, logarithmic stellar mass (based on the $3.6 \mu\text{m}$ emission), and logarithmic H I mass, as compared to the THINGS sample. VLA-ANGST galaxies are on average more nearby, late type, and low mass galaxies, both in terms of stellar and H I mass. The VLA-ANGST sample is thus much more dominated by low-mass dwarf irregulars and thus provides a complementary sample to THINGS. Comparison with LITTLE THINGS and SHIELD are shown in Fig. 2. Given the volume filling sample selection constraints, the VLA-ANGST galaxies are much more tightly located at distances of $\sim 2 - 4 \text{ Mpc}$, whereas LITTLE THINGS and SHIELD have a larger distance spread. Galaxy sizes are also broader distributed in LITTLE THINGS as compared to VLA-ANGST. LITTLE THINGS galaxies are on average brighter and SHIELD galaxies are at the faint end of optical absolute B magnitudes when compared to the VLA-ANGST sample. LITTLE THINGS contains more

H I-massive galaxies than VLA-ANGST and SHIELD is again at the fainter H I end. We include the SHIELD VLA Pilot galaxies in this plot, which are brighter than the proper SHIELD targets (see Cannon et al. 2011). The high mass end of the final SHIELD H I mass distribution is thus somewhat fainter than depicted in Fig. 2.

3. Observations and Data Reduction

The vast majority of the observations in VLA-ANGST are new. In a few cases, archival data were used in place of obtaining new observations to improve efficiency. Here we describe both the new and archival observations.

3.1. Description of Observations

The parameters for our new observations and the subsequent data reduction strategy closely followed the design of the THINGS survey (Walter et al. 2008), with the goal of obtaining comparable sensitivity and spatial resolution. A significant difference between the two surveys, however, is the ~ 5 times better velocity resolution of VLA-ANGST. Each of the VLA-ANGST galaxies was observed with the NRAO’s VLA in the B- (9 h total observing time per galaxy), C- (3 h), and D- (3 h) array configurations (under project code AO215). The compact D-configuration exhibits the largest number of short baselines with antenna separations down to 35 m. D-configuration is thus the most sensitive antenna configuration to image spatial scales of up to $\sim 16'$, which is the maximum for the VLA at 1.4 GHz. The addition of B-configuration observations yield spatial resolutions $\sim 6''$ or ~ 100 pc for the nearby ($D \sim 3$ Mpc) objects. This scale is necessary to compare star forming regions with their H I counterparts and matches well the resolution of surveys at other wavelengths such as LVL (SPITZER) and 11HUGS (GALEX). The southern sources

NGC 3109, NGC 247, Antlia, and DDO 6 were observed mostly in the hybrid BnA-, CnB-, and DnC-array configurations that feature elongated placements of the antennas along the northern arm. The projected baselines of these antenna configurations produce a more circular beam toward southern targets.

At the time of the observations, 2007 October to 2008 August, the VLA was in the process of being upgraded EVLA. This transition implied that the observations were taken with a mix of already converted EVLA and original VLA antennas. The conversion period mostly affected the signal distribution from the front-ends to the correlator. At the time, the old VLA correlator was still in use, and we configured it in the 2AC or 2AD modes to capture both RR and LL polarization products. Doppler tracking in the transition phase would have introduced phase jumps on baselines involving EVLA antennas. Consequently, we calculated and fixed the appropriate observing frequency for each observing run such that the H I emission line was well placed within a VLA bandpass at the start of an observation (Doppler setting). Line shifts during a single observation are minimal ($< 0.5 \text{ km s}^{-1}$) and are corrected in post-processing (§.3.2).

The observational parameters for each galaxy were based on its H I linewidth as taken from single dish H I spectra, plus $\sim 20\%$ additional line free channels to enable a good continuum subtraction. To reach our goal of the best possible velocity resolution, we used a correlator mode with 0.78 MHz bandwidth and 256 channels for 15 galaxies in our sample. This corresponds to a channel width of $\sim 0.65 \text{ km s}^{-1}$ over a total velocity range of $\sim 120 \text{ km s}^{-1}$ after cropping about 20% edge channels, 10% on each side. Eight galaxies had wider H I linewidths and were therefore observed with a bandwidth of 1.56 MHz and 256 channels ($\sim 300 \text{ km s}^{-1}$ velocity range and $\sim 1.3 \text{ km s}^{-1}$ channel width; see Table 3). The systemic velocity of KK 77 is unknown. To maximize on the range of velocities for this source, we used the 4IF mode for this galaxy, a correlator mode that enables observing with

two simultaneous frequencies. NGC 247 was also observed in the 4IF mode because of its extreme H I linewidth of $\sim 200 \text{ km s}^{-1}$, by far the widest line of our sample. In the presence of extremely strong, narrow line features, the response of the VLA can include signs of the Gibbs phenomenon, a *sinc* function that oscillates between channels. This oscillation can be suppressed by “Hanning” smoothing the data with a triangular smoothing kernel. We decided not to use online Hanning smoothing as the lines are too weak to show any signs of the Gibbs phenomenon. Some of the archival observations that we added in, however, were observed with online Hanning smoothing turned on. We also applied a 25 MHz frontend filter to reduce the impact on radio frequency interference (RFI) in our data.

For flux and bandpass calibration purposes, we observed the VLA standard flux calibrators 3C286 and/or 3C48 (with fluxes of $\sim 15.0 \text{ Jy}$ and $\sim 16.5 \text{ Jy}$, respectively) depending on their visibility at the time of the observations. Typical integration times were 12 minutes on the flux calibrator, split between the beginning and end of a track. We observed our target galaxies in 40 minute intervals alternating with 3 minutes on a nearby phase/complex gain calibrator. The complex gain calibrators were chosen to be nearby point sources with a minimum flux of $\sim 1 \text{ Jy}$. B-configuration observations were obtained in single 9 hour programs, or, in the case of southern galaxies, two 4.5 hour observations. In C- and D-configurations we combined sources into a few observations to reduce overhead and to obtain an improved *uv*-coverage.

During the VLA to EVLA transition time, the EVLA-EVLA baselines showed considerable aliasing and were largely unusable. Since the D-configuration observations had the largest number of EVLA antennas and therefore EVLA-EVLA baselines, we obtained an additional hour of observing time per object to reach our original sensitivity goals. Overall we obtained a total of 3 h in D-configuration per galaxy. The aliasing is a monotonic function that affects the first $\sim 0.5 \text{ MHz}$ (or $\sim 100 \text{ km s}^{-1}$ at the H I frequency), decreasing

from the bandpass edge toward the center⁴. In addition to the make-up time and using mostly baselines with old VLA antennas, we placed the H I lines away from the affected frequency ranges but could not fully eliminate the effects. As a result, the noise levels in our data products are not entirely uniform across all channels and increase toward lower frequencies where aliasing is strongest. Across the full width of our most narrow 0.78 MHz bandwidths the noise can vary up to 35%. For the smaller width of the spectral line feature, the effect is smaller. In addition, for part of the observations, we tried to place the H I signal away from the most affected frequency ranges and for most galaxies the noise level changes could be constrained to an rms variation of $\lesssim 15\%$ over the width of the H I line. For the two galaxies that were observed in the 4IF mode, KK 77 and NGC 247, the full bandwidths were required to cover the requested velocity ranges. The aliased signal appears in each IF and, consequently, the full noise variations of up to 35% are visible across the combined spectrum. Overall, however, this will not have a huge impact on most of the data analysis; KK 77 is a non-detection, and NGC 247 is one of our brightest objects such that the signal-to-noise ratio is only moderately affected.

A few galaxies (marked “a” in Table 2) had H I emission whose velocity range overlapped with Galactic H I line features. We addressed this problem by observing the bandpass calibrator at two different frequencies, offset by ± 4 MHz from the source frequency, in order to interpolate the calibration to the source frequency.

In addition to the new observations, in preparing for the program, we identified a few archival VLA observations which would be of use to the program. Most archival data, however, were observed at the relatively lower spectral resolution of 2.6 km s^{-1} with online Hanning smoothing applied. To avoid interpolation, we kept the lower velocity resolution of the archival data and rebinned our new VLA-ANGST observations after calibration for

⁴see <http://www.vla.nrao.edu/astro/guides/evlareturn/aliasing.shtml>

the final cube.

Table 2 lists all of our observational setups. Column (1) lists the galaxy names followed by the array configurations of the observations and the project codes in columns (2) and (3). AO215 is the genuine VLA-ANGST project, while other project codes refer to archival data. The observing dates are listed in column (4). Asterisks denote observations that span across midnight, for which we refer to the start dates. The equatorial pointing positions are provided in columns (5) and (6) and the appropriate equinox is tabulated in column (7). Column (8) gives the phase calibrators that were used for the observations. The correlator setups are displayed in columns (9) through (14) with (9) the correlator modes, (10) the bandwidths, (11) the number of channels, and (12) the channel widths in km s^{-1} (for the rest frequency of H I at 1.420405752 GHz). VLA-ANGST data were taken at the fixed sky frequencies listed in column (13) whereas many archival observations were Doppler tracked at the velocities listed in column (14). Finally, column (15) provides the number of converted EVLA antennas in the dataset with the remaining antennas being old, not yet converted, VLA antennas at the time.

3.2. Data Calibration

Data calibration was performed using the AIPS⁵ package and deviated from the “standard” VLA data reduction procedure due to the effects from the VLA to EVLA transition period. As mentioned above, EVLA-EVLA baselines showed considerable aliasing that affected primarily the narrow bandwidth observations. Our reduction scheme followed the following steps.

To avoid low signal-to-noise solutions during calibration, we started by eliminating

⁵The Astronomical Image Processing System (AIPS) has been developed by the NRAO.

edge channels. About 20% of the entire bandwidths were cropped, $\sim 10\%$ at the upper and $\sim 10\%$ at the lower frequency ends (task UVCOP). After correcting the absolute antenna positions (VLANT), the absolute flux scale of the primary flux calibrators 3C286 and 3C48 (see §. 3.1) were calculated by the task SETJY using NRAO-provided models and “Perley-Taylor 99” flux scales. We manually inspected all calibrator data in each array configuration for bad visibilities due to RFI or cross-talk between antennas (AIPS tasks TVFLAG, SPFLG, UVFLAG, WIPER). If calibrators showed higher than expected signal on short baselines due to solar interference, we excluded baselines with a uv range between 0 and 1 k λ in the calibration. Solar RFI was usually well removed by continuum subtraction in the source visibilities, so we performed no additional source flagging due to solar interference.

The data were then bandpass-corrected by deriving a channel-based, normalized gain solution from the flux calibrator data via BPASS. We produced a new broad band “channel zero” (CH0) map from these bandpass corrected data (AVSPC), and utilized the new CH0 map in all subsequent calibration steps. Next, we calculated the complex antenna gain as a function of time for all calibrators (CALIB). The complex gain is a solution for both gain and phase, and for all solutions we assumed that the complex gain calibrators are point-like. With CLCAL we linearly interpolated all phase/gain solutions for across all time intervals. GETJY transferred the flux calibration to the complex gain calibrator. At this stage, we manually inspected the quality of the calibration and repeated the above procedure if RFI corrupted the solution and further flagging was required. Finally, we applied all calibration solutions to the target galaxies. We estimate the calibration flux uncertainties to be $\sim 5\%$.

For galaxies whose H I emission is within the velocity range of the foreground Galactic emission (marked “a” in Table 2), the flux and bandpass calibrators were observed at offsets of ± 4 MHz relative to the frequency of the targets. The calibration of these data followed the

same steps as above with each observed frequency calibrated separately. We then obtained an interpolated flux and bandpass solution calibration from a linear interpolation across these offset frequencies. The EVLA uses different internal local oscillator settings than the VLA. For our observations during the VLA to EVLA transition phase, this difference had the unfortunate effect that, for some observations, the 25 MHz frontend filter overlapped in frequency with the upper frequency offset bandpass observations. This resulted in an extreme phase gradient across that particular offset frequency and the affected observations were unusable. In these cases, we calibrated the source data by extrapolating the calibration from the single offset frequency that most closely matched the bandpass derived from the phase calibrator. This method provided bandpasses that are accurate to few percent. For observations where the *complex gain* calibrator was contaminated by Galactic H I, we simply flagged the affected channels before calculating a new CH0 to be used for the gain and phase solutions.

After applying all calibration tables to the source, the galaxy data were separated (SPLIT) from the flux and phase calibrator data for further processing. Both NGC 247 and KK 77 were observed in the 4IF mode. We calibrated each of the 2IF windows separately as described above, and “stitched” the data together, averaging overlapping velocity ranges in the process (UJOIN) prior to continuum subtraction.

To determine the continuum level, we fit a linear function to the line-free channels, typically 20 channels on each side of the spectrum. The fit was then subtracted from the complex *uv*-data (task UVLSF). Since the frequencies for each observing set up were fixed (see §3.1), we regridded the H I data to a common heliocentric, optical velocity system (CVEL). Finally, data from all observations and array configurations were combined (DBCON) into a single data set for imaging. We produced dirty images with IMAGR and inspected the cubes for artifacts. If further flagging was required, we went back to the

original source data, flagged, and reapplied the calibration.

3.3. Mapping and Deconvolution

After satisfactory calibration and source editing, we used the AIPS task IMAGR to generate data cubes and final data products. We followed the THINGS protocol when possible so that the two data sets could be easily compared. For each VLA-ANGST galaxy, we imaged the visibilities with two different weighting schemes: one using natural weighting and one using the “robust” weighting (originally described by Briggs 1995, with small modifications as described in the AIPS help files). Natural weighting yields high sensitivity at moderate resolution (typically $\sim 6 - 12''$ for our galaxies, or about $\sim 90 - 170$ pc for a distance of 3 Mpc), while robust weighting decreases the size of the synthesized beam at the cost of reduced surface brightness sensitivity. We applied a robust parameter of 0.5, which was found to be a good compromise between resolution and sensitivity and matches the maps generated by THINGS. When compared to the naturally-weighted cubes, the noise in the robust-weighted cubes is typically $\sim 20\%$ higher and the beam size $\sim 40\%$ smaller. Depending on the angular extent of each galaxy’s H I emission, the cubes were imaged with either 1024^2 pixels at $1.5''$ per pixel or 2048^2 pixels at $1.0''$ per pixel. The cubes were deconvolved using the Clark CLEAN deconvolution algorithm (Clark 1980), stopping at a residual flux threshold of 2.5 times the noise level as measured in the cubes. Finally, we produced primary beam corrected data cubes that were later used in the moment map analysis (§ 4).

The properties of all data cubes are listed in Table 3 where column (1) lists the galaxy names followed by columns (2), (3), (4), and (5) that contain the weighting algorithms and the resulting beam major and minor axes sizes as well as the position angles of the deconvolved data. The average root mean squared noise per channel is shown in column (6)

and the channel width in (7), the number of pixels in each plane in column (8) followed by the pixel size in column (9).

The most important difference between the VLA-ANGST datacubes and the THINGS datacubes is the higher velocity resolution in the majority of the VLA-ANGST datacubes which was possible because of the overall smaller range in velocity of detectable H I in the VLA-ANGST sample of galaxies. The sensitive and spatial resolution of THINGS and VLA-ANGST are very similar. The spatial resolution of LITTLE THINGS and SHIELD are similar to VLA-ANGST, too, since all surveys share the same VLA array configuration setups. Given the wider lines of the somewhat more massive galaxies in LITTLE THINGS (see Fig. 2), the bandwidth had to be slightly increased for this survey and their velocity resolution hovers around the upper limit of ours at $\sim 2 \text{ km s}^{-1}$. On the other hand, LITTLE THINGS has about 1/3 longer integration times than VLA-ANGST. The two Westerbork surveys HALOGAS and WHISP exhibit 2 to 5 times lower spatial resolution than the VLA surveys but their sensitivity limits are comparable, observed at a lower velocity resolution of $\sim 5 \text{ km s}^{-1}$. FIGGS has a velocity resolution of $\sim 1.5 \text{ km s}^{-1}$ and a beam 2-8 times larger than VLA-ANGST.

To ensure that our datacubes would be as directly comparable to the THINGS datacubes as possible, we reduced THINGS observations using our calibration, mapping, and deconvolution protocols. Comparisons of our reductions of THINGS observations with the publicly available THINGS datacubes showed no significant differences.

3.4. Mask Generation

To suppress noise for the production of moment maps, we generated image cube masks that defined regions containing detectable H I emission from the galaxies. To do

so, we convolved the natural-weighted images to twice the original beam major axis and applied spectral Hanning smoothing with a three channel wide kernel. New “mask” cubes containing predominantly H I signal were constructed by keeping all regions corresponding to H I emission above the 1σ noise level and blanking all other regions. To remove the effects of sidelobes, noise spikes, or other spurious signals from the masks, any individual regions with an area smaller than the beam size were automatically removed. We then eliminated any remaining non-emission regions by eye inspection.

The result is a single mask cube per galaxy that we applied prior to the generation of the integrated spectra and moment maps. The same mask is used for both the natural and robust data cubes. New cubes containing predominantly H I signal were constructed by keeping all H I emission corresponding to unblanked regions in the mask cube. For our data, this method discriminated well between significant, low level emission and pure noise. Note that this process produces a lower limit to the total H I emission. Some very low surface brightness H I may have been eliminated from these data cubes.

Note that mask generation is not entirely automatic, and, therefore, our mask generation cannot be said to be strictly following THINGS protocols. This is exacerbated by the differences in typical channel widths, which leads to differences between VLA-ANGST and THINGS in average noise levels in the individual channels. Nonetheless, we have followed the intentions of the THINGS project to use masking to suppress the noise and to provide optimal moment maps. However, one should be aware that small differences in masks are possible and that the resulting moment maps have a small inherent systematic uncertainty.

3.5. Flux Densities

Recovery of the total H I flux from each channel and the resulting H I spectra is more complicated than simply summing up the total emission. Jörsäter & van Moorsel (1995) have shown that standard CLEAN maps do not in actuality yield correct flux measurements. Maps in AIPS are created by summing the CLEAN components, convolved with the CLEAN beam, to the signal that is still present in the residuals. While both maps are purportedly measured in Jansky (beam area)^{−1}, the relevant beam is different in each map: the convolved CLEAN component map is measured in Jy (CLEAN beam area)^{−1} while the residual map has units of Jy (dirty beam area)^{−1}. Because the areas of the CLEAN beam and the dirty beam are different, the flux in the CLEAN components and in the residuals must be corrected to obtain the proper H I flux. A full discussion of the following correction technique is given in Jörsäter & van Moorsel (1995). The corrected flux of a channel is given by:

$$G = C + \epsilon \times R \quad (1)$$

where G is the corrected flux, C is the flux in the convolved CLEAN components [with units of Jy (CLEAN beam)^{−1}], R is the flux in the residual map [with units of Jy (dirty beam)^{−1}], and ϵ is the correction factor that takes into account the ratio of the dirty beam area to the CLEAN beam area. IMAGR provides a method to automatically apply this correction and, following the THINGS protocol, we determined ϵ within the inner 50×50 pixels of the dirty and CLEAN beams. This produces a set of two new natural and robust weighted cubes with the above correction applied in addition to our standard cubes. When the residuals are scaled by ϵ , the noise in the corrected cubes is artificially suppressed. We thus produced two sets of data cubes for different analyses:

1. “Standard” cube: the standard output from our pipeline, with uncorrected H I fluxes but uniform noise properties. No primary beam correction is applied to these data.

This cube should be used for any analysis that requires uniform noise properties or uses selection based on noise (e.g., fitting of individual profiles in order to construct velocity fields or measure profile shapes).

2. “Rescaled” cube: the cube with the flux correction applied, to be used only in regions with genuine H I emission. The flux values in this cube are correct, and therefore any analysis that requires selection based on H I fluxes should use this cube (e.g., mass and column density measurements). The “rescaled” cube is corrected for the attenuation from the primary beam.

The data products that we make available follow this recipe; all global H I spectra (§ 3.6) and moment maps (§ 4) were derived using the masked, “rescaled cubes”. The online data cubes themselves are the “standard” cubes, without primary beam attenuation or flux corrections.

3.6. Global H I Spectra and Masses

Global H I spectra are derived from the masked, rescaled data cubes. The spectra are used to derive velocity widths at 20% (w_{20}) and 50% (w_{50}) of the peak. The central H I velocity of each galaxy is calculated by taking the mid-point of the w_{20} boundaries.

We also use the integrated H I spectra to calculate the total H I masses of our galaxies using the following equation:

$$M_{\text{HI}} [M_{\odot}] = 2.36 \times 10^5 D^2 \times \sum_i S_i \Delta v \quad (2)$$

where D is the distance to the galaxy in Mpc (as given in Table 1) and $S_i \Delta v$ is the total flux of a single channel in Jy km s^{-1} (e.g. Rohlfs & Wilson 2004). This formula assumes that the H I emission is optically thin, an assumption that is valid over a large flux range

and may begin to fail at very extreme column densities of $\gtrsim 10^{22} \text{ cm}^{-2}$ (e.g. Allen et al. 2012; Braun 2012). At our spatial resolution, we do not observe column densities of this magnitude.

In Table 4, we present all of the derived H I parameters starting with the galaxy names in column (1), followed by the integrated H I flux densities S_{HI} and the derived H I masses in columns (2) and (3). For comparison, we compiled single dish fluxes $S_{\text{HI}}^{\text{SD}}$ from the literature and list them in column (4). The w_{20} and w_{50} values as well as the central velocities are shown in columns (5), (6), and (7), respectively, followed by the peak H I column density (§ 4.3.1) taken from the natural-weighted map in the final column (8). To derive upper limits for the non-detections, we assume an H I disk the same size as the optical diameter D_{25} and a hypothetical linewidth of 20 km s^{-1} . Galaxies typically exhibit H I dispersions of $5\text{--}10 \text{ km s}^{-1}$ and a linewidth of 20 km s^{-1} thus implies little rotation or face-on orientation.

In $\sim 70\%$ of all cases the single dish fluxes are somewhat larger than the interferometric VLA flux measurements. This difference is expected to some level given that the VLA can only image structures with an extent of up to $\sim 16'$ in D-configuration at 1.4 GHz (limited by the minimum distance between two antennas). Missing flux may therefore only be a significant issue for the most extended objects in our sample. Some single dish flux measurements deviate substantially from the trend of being slightly larger than the VLA fluxes. The deviations can be either way: galaxies like DDO 6, UGC 4483, DDO 113, and KK 230 have much larger single dish measurements whereas others like BK 3N, AO 0952+69, Sextans B, DDO 82, and DDO 190, have smaller single dish fluxes. Such discrepancies may be explained by difficulties in single dish baseline subtraction or by the larger single dish beam that tends to pick up larger fractions of Galactic H I emission as well as flux from nearby objects.

4. Data Products

4.1. H I Spectra

We used the naturally-weighted data cubes to derive H I spectra (§ 3.6) for our galaxies given their higher surface brightness sensitivity compared to the robust-weighted data. This approach captures as much low-level, extended emission as is possible with interferometric VLA data. All fluxes are calculated from the rescaled cubes described in § 3.5 and are presented in Fig. 3. In the case of NGC 247, velocities around 108 km s^{-1} were strongly contaminated with RFI; to estimate the H I flux in this channel, we interpolated the emission from the adjacent channels.

Since our sample is composed primarily of dwarf galaxies, the galaxy spectra typically show narrow, singly-peaked profiles. Extreme cases like KDG 73 and KKH 86 exhibit linewidths of $< 10 \text{ km s}^{-1}$, which implies very little velocity dispersion, maybe due to low signal to noise in the line wings. On the other end of the mass spectrum, a few galaxies (NGC 404, NGC 3741, DDO 190, Sextans A, DDO 181, NGC 3109, NGC 247) exhibit hints of the more familiar double-horned profile expected from larger spiral disks. The maximum linewidth is observed in NGC 247 with $w_{20} \sim 200 \text{ km s}^{-1}$.

4.2. Channel Maps

Channel maps of the galaxies are presented in Figs. 4 through 32 (natural weighting). Given the high spectral resolution of our data, there is typically only little flux in each velocity bin. Some galaxies, mainly the more massive ones such as NGC 247 or NGC 3109 show the classic “butterfly” pattern of a spiral galaxy, a tell-tale sign for a flat rotation curve. The bulk of galaxies exhibit rotation despite the fact that the dispersion adds a stochastic component to the velocity structure. NGC 247 also features a H I absorption

feature along the line of sight to the background quasar NVSS J004713-205114 at RA (J2000)= $00^h : 47^m : 13.6^s$ and DEC (J2000)= $-20^\circ : 51' : 15''$ (e.g., Dickey et al. 1992). Some data cubes are contaminated by Galactic foreground emission, but only for NGC 404 is the Galactic H I close to the systemic velocity of the source. Other data cubes, such as that for AO 0952+69, contain emission from a nearby object. AO 0952+69, in fact, is likely not a real galaxy but might be a feature within a spatially coincident spiral arm that belongs to the massive M 81 galaxy.

4.3. Moment Maps

We used the AIPS task XMOM to generate moment maps from the masked, flux-corrected cubes. For all calculations we require that each pixel in a moment map is calculated from at least four unmasked channels; pixels with fewer channels are masked in all moment maps.

4.3.1. Integrated HI Maps

Integrated H I column density maps are created from the masked, rescaled data cube by integrating along the velocity axis to generate the moment 0 map:

$$I_{\text{HI}} = \sum_i S_i \times \Delta v \quad (3)$$

where i is the channel, S_i is the flux density in the i th channel in Jy beam^{-1} , and Δv is the channel spacing in km s^{-1} . We then convert the moment maps to column density with

$$N_{\text{HI}} = 1.104 \times 10^{24} \frac{1}{b_{\text{maj}} b_{\text{min}}} \sum_i S_i \Delta v \quad (4)$$

where b_{maj} and b_{min} are the beam major and minor axes in arcseconds and $\sum_i S_i \Delta v$ is the value of moment 0 map at each pixel in units of $\text{Jy beam}^{-1} \text{km s}^{-1}$. In Figs. 4 to 32 we show

column density maps for all galaxies with detected H I (upper left panels on the second page of each figure) We also show column density contours overlaid on optical images for each galaxy. On these maps (upper right), we placed the footprints of the HST observations that are available through ANGST.

The maps exhibit resolved H I structures comparable to their beam sizes. Some galaxies, like KK 230, or NGC 404 have low columns with peak values of a few times 10^{20} cm^{-2} . Other galaxies like DDO 190, or UGCA 292 reach columns of a few times 10^{21} cm^{-2} (or $\sim 10 \text{ M}_{\odot} \text{ pc}^{-2}$), which is a canonical threshold for star formation (e.g., Skillman 1987; Kennicutt 1989; Bigiel et al. 2008; Leroy et al. 2008).

4.3.2. *Intensity-weighted Velocity Field Maps*

The H I intensity-weighted velocity fields (moment 1) maps are calculated using

$$\langle v \rangle = \frac{\sum_i S_i \times v_i}{\sum_i S_i}. \quad (5)$$

For well-behaved disks this equation gives a good indication of the average velocity of gas in a given pixel. However, bulk motions, outflows, and other non-circular motions can shift the derived velocity to unexpected values. Therefore, profile fitting in order to determine the velocity of the peak of the emission is a more reliable method for finding the average rotational velocity of the gas at a given location in the galaxy. While the velocity fields of lower mass dwarfs are less ordered than those of their larger disk counterparts, most still show velocity gradients across their disks that are indicative of rotation, which is typical for H I in dwarf galaxies (Begum et al. 2008; Walter et al. 2008). The H I intensity-weighted velocity maps are shown in the lower right panels of the second page of for each galaxy in Figs. 4 to 32.

4.3.3. Second Moment Maps

The linewidth of H I emission can be characterized by the intensity-weighted second velocity moment as given by:

$$\sigma = \sqrt{\frac{\sum_i S_i \times (v_i - \langle v \rangle)^2}{\sum_i S_i}} \quad (6)$$

where $\langle v \rangle$ indicates the intensity-weighted velocity derived in the first moment map. While the second moment can be indicative of the turbulence of the ISM, it also reflects the influence of large scale gas flows such as expanding shells or tidal material. At lower resolution, the velocity dispersion can be artificially inflated by beam smearing over the gradient in the velocity field, especially towards the centers of the galaxies, where this gradient is steepest. Overall, the velocity dispersion values fall in a relatively narrow range of 5-15 km s⁻¹, as seen in the lower right panel on the second page of Figs. 4 to 32).

Pixels which yield first velocity moments outside the velocity range of the data cube are blanked in all moment maps. The first and second moment maps generated from the robust data cubes are noisier than those from natural-weighted cubes and occasionally have pixels with unrealistic values in low column density regions. To counter this problem, we blanked all pixels with column densities $N_{\text{HI}} < 3 \times 10^{19} \text{ cm}^{-2}$ in the robust moment maps.

5. Summary

Here we present the sample selection criteria, observational parameters, data reduction procedures, and data product description of the VLA-ANGST survey, a Large VLA project that targets nearby, mostly dwarf irregular galaxies. Of the 35 galaxies in the survey, we detect H I in 29. The calibrated VLA data for these objects are publicly available at <https://science.nrao.edu/science/surveys/vla-angst>. This leads to the following

data products:

- Global H I spectra for all galaxies, derived from the masked, flux-corrected, primary beam corrected, natural-weighted data cubes.
- H I data cubes of both natural and robust weighting. The cubes are not primary beam or flux corrected and they are unmasked.
- Integrated intensity maps (moment 0 maps) in units of $\text{Jy beam}^{-1} \text{ km s}^{-1}$ as well as converted to H I column densities. These maps were derived from the masked, flux-corrected, primary beam corrected data cubes. We offer both, natural and robust-weighted maps for download.
- The intensity-weighted velocity field maps (moment 1 maps), derived from the same data products as the integrated intensity maps.
- Second moment maps which give a measure for the velocity dispersion of the gas; derived from the same data products as the integrated intensity maps.

This paper presents the observations; scientific analyses will follow in subsequent publications. A study that compares the H I kinematics of large H I shells to the supernovae and stellar wind output of the underlying stellar populations is presented in Warren et al. (2011). Detection and characterization of narrow H I components that presumably trace cold H I are provided in Warren et al. (2012). Stilp et al. (2012) correlate averaged H I dispersion values to the physical properties of the host galaxies. The true value of our H I survey is further unlocked by the extensive, multi-wavelength ancillary data that is available for many of our objects. The VLA-ANGST, THINGS, LITTLE THINGS, and SHIELD data products are furthermore similar in sensitivity, spatial and spectral resolution and provide H I data cubes for > 100 galaxies.

Table 1. General properties of the VLA-ANGST galaxy sample.

(1) Name	(2) Alt. Name	(3) RA (J2000) [$^{\circ}$, $'$, $''$, s]	(4) DEC (J2000) [$^{\circ}$, $'$, $''$]	(5) D [Mpc]	(6) D_{25} [kpc]	(7) M_B [mag]	(8) νL_{ν} ($3.6 \mu\text{m}$) [$10^6 L_{\odot}$]	(9) Type	(10) SFR (UV) [$10^{-3} M_{\odot} \text{ yr}^{-1}$]
NGC 247	ESO 540-G022, UGCA 11	00:47:08.3	-20:45:36	3.50	15.7	-17.86	270.52	7	229
DDO 6	ESO 540-G031, UGCA 15	00:49:49.3	-21:00:58	3.31	1.6	-12.41	...	10	1.4
NGC 404	UGC 718	01:09:26.9	35:43:03	3.05	2.2	-16.21	...	-1	6.6
KKH 37	LEDA 95597	06:47:45.8	80:07:26	3.26	1.1 ^a	-11.17	0.69	10	0.3
UGC 4483	CGCG 331-051	08:37:03.0	69:46:31	3.41	1.2	-12.71	0.57	10	4.0
KK 77	LEDA 166101	09:50:10.0	67:30:24	3.55	2.5 ^a	-11.45	...	-3	...
BK3N	PGC 28529	09:53:48.5	68:58:09	3.86	0.6	-9.15	<0.03	10	0.3
AO 0952+69 ^b	Arp's Loop	09:57:29.0	69:16:20	3.78	2.0	-11.09	...	10	1.1
Sextans B	UGC 5373, DDO 70	10:00:00.1	05:19:56	1.39	2.1	-13.87	2.48	10	4.5
NGC 3109	ESO 499-G036, DDO 236	10:03:07.2	-26:09:36	1.26	6.2	-15.11	12.40	10	28.7
Antlia	PGC 29194	10:04:04.0	-27:19:55	1.29	0.8	-9.36	...	10	1.8
KDG 63	UGC 5428 DDO 71	10:05:07.3	66:33:18	3.53	1.7	-11.73	1.36	-3	...
Sextans A	UGCA 205, DDO 075	10:11:00.8	-04:41:34	1.38	2.2	-13.84	1.82	10	12.3
HS 117	...	10:21:25.2	71:06:58	3.82	1.7	-11.41	1.08	10	...
DDO 82	UGC 5692	10:30:35.0	70:37:10	3.80	3.8	-14.33	...	9	2.6
KDG 73	PGC 32667	10:52:55.3	69:32:45	4.03	0.7	-10.94	0.81	10	0.3
NGC 3741	UGC 6572	11:36:06.4	45:17:07	3.24	1.9	-13.17	1.29	10	6.2
DDO 99	UGC 6817	11:50:53.0	38:52:50	2.59	3.1	-13.37	1.43	10	5.5
NGC 4163	NGC 4167, UGC 7199	12:12:08.9	36:10:10	2.86	1.6	-13.65	3.66	10	4.0
NGC 4190	UGC 07232	12:13:44.6	36:38:00	3.50 ^c	1.7	-14.20	5.80	10	10.1
DDO 113	UGCA 276	12:14:57.9	36:13:08	2.95	1.3	-11.65	0.61	10	...
MCG +09-20-131	CGCG 269-049	12:15:46.7	52:23:15	1.60 ^d	0.6	-10.72	...	10	0.4
DDO 125	UGC 7577	12:27:41.8	43:29:38	2.58	3.2	-14.11	4.15	10	5.3
UGCA 292	PGC 42275	12:38:40.0	32:46:00	3.62	1.1	-11.69	0.48	10	2.9
GR 8	UGC 8091, DDO 155	12:58:40.4	14:13:03	2.08	0.7	-11.98	0.34	10	2.4
UGC 8508	IZw 60	13:30:44.4	54:54:36	2.58	1.3	-12.94	1.40	10	...
DDO 181	UGC 8651	13:39:53.8	40:44:21	3.14	2.1	-13.03	1.51	10	3.8
DDO 183	UGC 8760	13:50:51.1	38:01:16	3.22	2.1	-13.09	1.63	9	3.2
KKH 86	LEDA 2807150	13:54:33.6	04:14:35	2.59	0.5 ^a	-10.19	0.22	10	0.1
UGC 8833	PGC 49452	13:54:48.7	35:50:15	3.08	0.8	-12.29	0.60	10	1.4
KK 230	KKR 3	14:07:10.7	35:03:37	1.97	0.3 ^a	-8.57	0.05	10	0.2
DDO 187	UGC 9128	14:15:56.5	23:03:19	2.21	1.1	-12.34	0.39	10	1.1

Table 1—Continued

(1) Name	(2) Alt. Name	(3) RA (J2000) [$^h, m, s$]	(4) DEC (J2000) [$^{\circ}, ', ''$]	(5) D [Mpc]	(6) D_{25} [kpc]	(7) M_B [mag]	(8) νL_{ν} ($3.6 \mu\text{m}$) [$10^6 L_{\odot}$]	(9) Type	(10) SFR (UV) [$10^{-3} M_{\odot} \text{ yr}^{-1}$]
DDO 190	UGC 9240	14:24:43.5	44:31:33	2.79	1.5	-14.13	3.12	10	6.1
KKR 25	LEDA 2801026	16:13:47.6	54:22:16	1.93	0.6 ^a	-9.98	<0.02	10	...
KKH 98	LEDA 2807157	23:45:34.0	38:43:04	2.54	0.8 ^a	-10.32	0.40	10	0.6

References. — (5) tip of the red giant branch distances from Dalcanton et al. (2009); (6) taken from Dalcanton et al. (2009) and converted to physical diameters; (7) apparent blue magnitudes from Karachentsev et al. (2004) and converted to absolute blue magnitudes; (8) converted from infrared fluxes given by Dale et al. (2009); (9) T-type from Dalcanton et al. (2009); (10) converted from GALEX FUV asymptotic magnitudes given by Lee et al. (2011) and using $SFR = 1.4 \times 10^{-28} L_{\nu} (\text{erg s}^{-1} \text{ Hz}^{-1})$ (Kennicutt 1998)

^afor the KK-listed objects, the diameters are taken at a $26.5 \text{ mag arcsec}^{-2}$ surface brightness level

^bobject might be a feature in the spiral arm of M 81 rather than a galaxy

^cTRGB distance from Karachentsev et al. (2004)

^dthe TRGB branch was not unambiguously identified in Dalcanton et al. (2009)

Table 2. List of Observations

(1)	(2)	(3)	(4)	(5)	(6)	(7)	(8)	(9)	(10)	(11)	(12)	(13)	(14)	(15)
Galaxy	Conf.	Project	Date	RA	Dec	Equ.	Cal	Mode	BW	Chan	Δv	ν_{obs1}	v_{obs1}	N_{EVLA}
			[yyyy-mm-dd]	[$^{\circ}$: $'$: $''$]	[$^{\circ}$: $'$: $''$]				[MHz]	#	[km s^{-1}]	[MHz]	[km s^{-1}]	
NGC 247	BnA	AO215	2007-10-10	00:47:08.5	-20:45:37	2000	0110-076	4	1.56	128	2.6	1419.098 ^a	...	12
												1420.222 ^a	...	
NGC 247	BnA	AO215	2007-10-11	00:47:08.5	-20:45:37	2000	0110-076	4	1.56	128	2.6	1419.098 ^a	...	12
												1420.222 ^a	...	
NGC 247	B	AO215	2008-01-11	00:47:08.5	-20:45:37	2000	0110-076	4	1.56	128	2.6	1419.008 ^a	...	13
												1420.132 ^a	...	
NGC 247	B	AO215	2008-01-12	00:47:08.5	-20:45:37	2000	0110-076	4	1.56	128	2.6	1419.008 ^a	...	13
												1420.132 ^a	...	
NGC 247	CnB	AO215	2008-02-17	00:47:08.5	-20:45:37	2000	0110-076	4	1.56	128	2.6	1419.059 ^a	...	13
												1420.182 ^a	...	
NGC 247	DnC	AO215	2008-06-12	00:47:08.5	-20:45:37	2000	0116-208	4	1.56	128	2.6	1419.233 ^a	...	15
DDO 6	BnA	AO215	2007-10-05	00:49:49.2	-21:00:54	2000	0145-275	2AD	0.78	256	0.6	1419.010	...	12
DDO 6	BnA	AO215	2007-10-07	00:49:49.2	-21:00:54	2000	0145-275	2AD	0.78	256	0.6	1419.010	...	12
DDO 6	CnB	AO215	2008-02-16	00:49:49.2	-21:00:54	2000	0145-275	2AC	0.78	256	0.6	1418.953	...	13
DDO 6	DnC	AO215	2008-06-12	00:49:49.2	-21:00:54	2000	0116-208	2AC	0.78	256	0.6	1419.158	...	15
DDO 6	DnC	AO215	2008-07-11	00:49:49.2	-21:00:54	2000	0116-208	2AC	0.78	256	0.6	1419.140	...	16
NGC 404	B	AO215	2007-11-13	01:09:27.0	+35:43:04	2000	0119+321	2AD	0.78	256	0.6	1420.598 ^a	...	12
NGC 404	C	AC459	1996-01-01	01:06:39.0	+35:28:00	1950	0116+319	2AD	1.56	128	2.6	...	-56.0	0
NGC 404	D	AO215	2008-08-21	01:09:27.0	+35:43:04	2000	0119+321	2AC	0.78	256	0.6	1420.753 ^a	...	17
NGC 404	D	AC459	1996-07-16	01:06:39.0	+35:28:00	1950	0116+319	2AD	1.56	128	2.6	...	-56.0	0

Table 2—Continued

(1) Galaxy	(2) Conf.	(3) Project	(4) Date [yyyy-mm-dd]	(5) RA [$^{\circ}$, $^{\prime}$, $^{\prime\prime}$, s]	(6) Dec [$^{\circ}$, $^{\prime}$, $^{\prime\prime}$]	(7) Equ.	(8) Cal	(9) Mode	(10) BW [MHz]	(11) Chan #	(12) Δv [km s^{-1}]	(13) ν_{obs1} [MHz]	(14) v_{obs1} [km s^{-1}]	(15) N_{EVLA}
KKH 37	B	AO215	2007-12-15	06:47:45.8	+80:07:26	2000	0410+769	2AD	0.78	256	0.6	1421.121 ^a	...	12
KKH 37	C	AO215	2008-04-11	06:47:45.8	+80:07:26	2000	0410+769	2AC	0.78	256	0.6	1421.033 ^a	...	15
KKH 37	D	AO215	2008-07-12	06:47:45.8	+80:07:26	2000	0410+769	2AC	0.78	256	0.6	1421.150 ^a	...	16
KKH 37	D	AO215	2008-08-11	06:47:45.8	+80:07:26	2000	0410+769	2AC	0.78	256	0.6	1421.161 ^a	...	16
UGC 4483	B	AO215	2007-12-22	08:37:03.0	+69:46:31	2000	0834+555	2AD	1.56	256	1.3	1419.698 ^a	...	12
UGC 4483	B	AZ090	1997-04-01	08:32:06.0	+69:58:00	1950	0831+557	2AD	1.56	128	2.6	...	180.0	29
UGC 4483	B	AZ090	1997-04-11	08:32:06.0	+69:58:00	1950	0831+557	2AD	1.56	128	2.6	...	180.0	29
UGC 4483	B	AZ090	1997-04-12	08:32:06.0	+69:58:00	1950	0831+557	2AD	1.56	128	2.6	...	180.0	0
UGC 4483	C	AZ090	1997-06-28	08:32:06.0	+69:58:00	1950	0831+557	2AD	1.56	128	2.6	...	180.0	0
UGC 4483	C	AZ090	1997-08-14	08:32:06.0	+69:58:00	1950	0831+557	2AD	1.56	128	2.6	...	180.0	0
UGC 4483	D	AO215	2008-07-10	08:37:03.0	+69:46:31	2000	0834+555	2AC	1.56	256	1.3	1419.700 ^a	...	16
UGC 4483	D	AO215	2008-08-16	08:37:03.0	+69:46:31	2000	0834+555	2AC	1.56	256	1.3	1419.200 ^a	...	17
KK 77	B	AO215	2007-12-07	09:50:10.5	+67:30:24	2000	1035+564	4	1.56	128	2.2	1419.174 ^a	...	12
KK 77	C	AO215	2008-03-31	09:50:10.5	+67:30:24	2000	1035+564	4	1.56	128	2.6	1420.298 ^a	...	14
KK 77	D	AO215	2008-08-10	09:50:10.5	+67:30:24	2000	1035+564	4	1.56	128	2.6	1419.025 ^a	...	16
KK 77	D	AO215	2008-08-19	09:50:10.5	+67:30:24	2000	1035+564	4	1.56	128	2.6	1420.148 ^a	...	16
KK 77	D	AO215	2008-08-19	09:50:10.5	+67:30:24	2000	1035+564	4	1.56	128	2.6	1419.139 ^a	...	16
KK 77	D	AO215	2008-08-19	09:50:10.5	+67:30:24	2000	1035+564	4	1.56	128	2.6	1420.262 ^a	...	17

Table 2—Continued

(1)	(2)	(3)	(4)	(5)	(6)	(7)	(8)	(9)	(10)	(11)	(12)	(13)	(14)	(15)
Galaxy	Conf.	Project	Date	RA	Dec	Equ.	Cal	Mode	BW	Chan	Δv	ν_{obs1}	v_{obs1}	$N_{\text{EVL A}}$
			[yyyy-mm-dd]	[$^{\circ}$; $^{\circ}$; $^{\circ}$]	[$^{\circ}$; $^{\circ}$; $^{\circ}$]				[MHz]	#	[km s^{-1}]	[MHz]	[km s^{-1}]	
BK3N	B	AO215	2007-12-18	09:53:48.5	+68:58:08	2000	1035+564	2AD	0.78	256	0.6	1420.644 ^a	...	12
BK3N	C	AO215	2008-03-16	09:53:48.5	+68:58:08	2000	1035+564	2AC	0.78	256	0.6	1420.522 ^a	...	14
BK3N	D	AO215	2008-07-18	09:53:48.5	+68:58:08	2000	1035+564	2AC	0.78	256	0.6	1420.590 ^a	...	16
BK3N	D	AO215	2008-08-15	09:53:48.5	+68:58:08	2000	1035+564	2AC	0.78	256	0.6	1420.631 ^a	...	17
AO 0952+69	B	AO215	2007-12-09	09:57:31.0	+69:16:60	2000	1035+564	2AD	1.56	256	1.3	1419.996 ^a	...	12
AO 0952+69	C	AO215	2008-03-31	09:57:31.0	+69:16:60	2000	1035+564	2AC	1.56	256	1.3	1419.855 ^a	...	14
AO 0952+69	D	AO215	2008-08-11	09:57:31.0	+69:16:60	2000	1035+564	2AC	1.56	256	1.3	1419.967 ^a	...	16
Sextans B	B	AO215	2007-11-16	10:00:00.1	+05:19:56	2000	1024-008	2AD	1.56	256	1.3	1419.103	...	12
Sextans B	C	AM561	1997-08-02	09:59:59.9	+05:19:43	2000	1008+075	2AD	0.78	128	1.3	...	301.0	0
Sextans B	D	AO215	2008-08-03	10:00:00.1	+05:19:56	2000	0943-083	2AC	1.56	256	1.3	1418.890	...	16
NGC 3109	BnA	AO215	2007-10-07	10:03:06.9	-26:09:34	2000	0921-263	2AD	1.56	256	1.3	1418.570	...	12
NGC 3109	BnA	AO215	2007-10-08	10:03:06.9	-26:09:34	2000	0921-263	2AD	1.56	256	1.3	1418.570	...	12
NGC 3109	CnB	AO215	2008-02-26	10:03:06.9	-26:09:34	2000	0921-263	2AC	1.56	256	1.3	1418.526	...	14
NGC 3109	DnC	AO215	2008-06-15	10:03:06.9	-26:09:34	2000	0921-263	2AC	1.56	256	1.3	1418.402	...	15
NGC 3109	DnC	AO215	2008-07-12	10:03:06.9	-26:09:34	2000	0921-263	2AC	1.56	256	1.3	1418.470	...	16
Antlia	BnA	AO215	2007-10-06	10:04:04.1	-27:19:52	2000	0921-263	2AD	0.78	256	0.6	1418.740	...	12

Table 2—Continued

(1)	(2)	(3)	(4)	(5)	(6)	(7)	(8)	(9)	(10)	(11)	(12)	(13)	(14)	(15)
Galaxy	Conf.	Project	Date	RA	Dec	Equ.	Cal	Mode	BW	Chan	Δv	ν_{obs1}	v_{obs1}	N_{EVLA}
			[yyyy-mm-dd]	[^h : ^m : ^s]	[[°] : ['] : ^{''}]				[MHz]	#	[km s ⁻¹]	[MHz]	[km s ⁻¹]	
Antlia	BnA	AO215	2007-10-13	10:04:04.1	-27:19:52	2000	0921-263	2AD	0.78	256	0.6	1418.755	...	12
Antlia	CnB	AA232	1998-11-02	10:01:47.5	-27:05:15	1950	1015-314	2AD	0.78	128	1.3	...	360.0	0
Antlia	CnB	AA232	1998-11-13	10:01:47.5	-27:05:15	1950	1015-314	2AD	0.78	128	1.3	...	360.0	0
Antlia	DnC	AO215	2008-06-15	10:04:04.1	-27:19:52	2000	0921-263	2AC	0.78	256	0.6	1418.578	...	15
Antlia	DnC	AO215	2008-07-26	10:04:04.1	-27:19:52	2000	0921-263	2AC	0.78	256	0.6	1418.614	...	16
KDG 63	B	AO215	2007-11-29	10:05:06.4	+66:33:32	2000	1035+564	2AD	0.78	256	0.6	1421.093 ^a	...	12
KDG 63	C	AO215	2008-04-05	10:05:06.4	+66:33:32	2000	1035+564	2AC	0.78	256	0.6	1420.930 ^a	...	14
KDG 63	D	AO215	2008-08-08	10:05:06.4	+66:33:32	2000	1035+564	2AC	0.78	256	0.6	1421.010 ^a	...	16
KDG 63	D	AO215	2008-08-17	10:05:06.4	+66:33:32	2000	1035+564	2AC	0.78	256	0.6	1421.052 ^a	...	17
Sextans A	B	AO215	2007-11-21	10:11:00.8	-04:41:34	2000	1024-008	2AD	1.56	256	1.3	1418.981	...	12
Sextans A	C	AO215	2008-03-16	10:11:00.8	-04:41:34	2000	1024-008	2AC	1.56	256	1.3	1418.799	...	14
Sextans A	D	AO215	2008-04-12	10:11:00.8	-04:41:34	2000	1024-008	2AC	1.56	256	1.3	1418.770	...	16
Sextans A	D	AO215	2008-08-17	10:11:00.8	-04:41:34	2000	0943-083	2AC	1.56	256	1.3	1418.819	...	17
HS 117	B	AO215	2007-11-28	10:21:25.2	+71:06:51	2000	1035+564	2AD	0.78	256	0.6	1420.649 ^a	...	12
HS 117	C	AO215	2008-04-11	10:21:25.2	+71:06:51	2000	1035+564	2AC	0.78	256	0.6	1420.500 ^a	...	15
HS 117	D	AO215	2008-07-14	10:21:25.2	+71:06:51	2000	1035+564	2AC	0.78	256	0.6	1420.575 ^a	...	16
HS 117	D	AO215	2008-08-11	10:21:25.2	+71:06:51	2000	1035+564	2AC	0.78	256	0.6	1420.608 ^a	...	16
NG														
DDO 82	B	AO215	2007-12-13	10:30:35.0	+70:37:07	2000	1035+564	2AD	1.56	256	1.3	1420.194 ^a	...	12

Table 2—Continued

(1) Galaxy	(2) Conf.	(3) Project	(4) Date [yyyy-mm-dd]	(5) RA [$^h:m:s$]	(6) Dec [$^{\circ}:\prime:\prime$]	(7) Equ.	(8) Cal	(9) Mode	(10) BW [MHz]	(11) Chan #	(12) Δv [km s $^{-1}$]	(13) ν_{obs1} [MHz]	(14) v_{obs1} [km s $^{-1}$]	(15) N_{EVLA}
DDO 82	C	AO215	2008-04-08	10:30:35.0	+70:37:07	2000	1035+564	2AC	1.56	256	1.3	1420.061 ^a	...	14
DDO 82	D	AO215	2008-08-11	10:30:35.0	+70:37:07	2000	1035+564	2AC	1.56	256	1.3	1420.165 ^a	...	16
DDO 82	D	AO215	2008-08-16	10:30:35.0	+70:37:07	2000	1035+564	2AC	1.56	256	1.3	1420.150 ^a	...	16
KDG 73	B	AO215	2007-11-27	10:52:57.1	+69:32:58	2000	1313+675	2AD	0.78	256	0.6	1419.928 ^a	...	12
KDG 73	C	AO215	2008-04-11	10:52:57.1	+69:32:58	2000	1313+675	2AC	0.78	256	0.6	1419.778 ^a	...	15
KDG 73	D	AO215	2008-07-14	10:52:57.1	+69:32:58	2000	1313+675	2AC	0.78	256	0.6	1419.845 ^a	...	16
KDG 73	D	AO215	2008-08-16	10:52:57.1	+69:32:58	2000	1313+675	2AC	0.78	256	0.6	1419.883 ^a	...	17
NGC 3741	B	AO215	2007-11-06	11:36:06.2	+45:17:01	2000	1146+399	2AD	1.56	256	1.3	1419.434 ^a	...	12
NGC 3741	C	AO215	2008-05-05	11:36:06.2	+45:17:01	2000	1146+399	2AC	1.56	256	1.3	1419.218 ^a	...	15
NGC 3741	D	AO215	2008-08-04	11:36:06.2	+45:17:01	2000	1146+399	2AC	1.56	256	1.3	1419.295 ^a	...	17
DDO 99	B	AO215	2007-12-04	11:50:53.0	+38:52:49	2000	1146+399	2AD	1.56	256	1.3	1419.363	...	12
DDO 99	C	AO215	2008-04-05	11:50:53.0	+38:52:49	2000	1146+399	2AC	1.56	256	1.3	1419.180	...	14
DDO 99	D	AO215	2008-08-07	11:50:53.0	+38:52:49	2000	1146+399	2AC	1.56	256	1.3	1419.180	...	16
DDO 99	D	AO215	2008-08-10	11:50:53.0	+38:52:49	2000	1146+399	2AC	1.56	256	1.3	1419.204	...	16
NGC 4163	B	AO215	2007-11-23	12:12:09.1	+36:10:09	2000	1227+365	2AD	0.78	256	0.6	1419.740	...	12
NGC 4163	B	AH927 ^b	2008-02-12	12:12:09.1	+36:10:09	2000	1227+365	2AC	0.78	256	0.6	1419.719 ^a	...	13
NGC 4163	C	AO215	2008-04-08	12:12:09.1	+36:10:09	2000	1227+365	2AC	0.78	256	0.6	1419.563	...	14
NGC 4163	C	AH927 ^b	2008-06-01	12:12:09.1	+36:10:09	2000	1227+365	2AC	0.78	256	0.6	1419.546 ^a	...	15

Table 2—Continued

(1) Galaxy	(2) Conf.	(3) Project	(4) Date [yyyy-mm-dd]	(5) RA [$^{\circ}$: $'$: $''$]	(6) Dec [$^{\circ}$: $'$: $''$]	(7) Equ.	(8) Cal	(9) Mode	(10) BW [MHz]	(11) Chan #	(12) Δv [km s^{-1}]	(13) ν_{obs1} [MHz]	(14) v_{obs1} [km s^{-1}]	(15) N_{EVLA}
NGC 4163	D	AO215	2008-08-06	12:12:09.1	+36:10:09	2000	1227+365	2AC	0.78	256	0.6	1419.540	...	16
NGC 4190	B	AO215	2007-24-24	12:13:44.8	+36:38:03	2000	1227+365	2AD	1.56	256	1.3	1419.441 ^a	...	13
NGC 4190	C	AO215	2008-03-09	12:13:44.8	+36:38:03	2000	1227+365	2AC	1.56	256	1.3	1419.323 ^a	...	14
NGC 4190	D	AO215	2008-08-11	12:13:44.8	+36:38:03	2000	1227+365	2AC	1.56	256	1.3	1419.275 ^a	...	16
DDO 113	B	AO215	2007-12-01	12:14:57.9	+36:13:08	2000	1227+365	2AD	1.56	256	1.3	1419.179	...	12
DDO 113	C	AO215	2008-04-04	12:14:57.9	+36:13:08	2000	1227+365	2AC	1.56	256	1.3	1419.007	...	14
DDO 113	D	AO215	2008-08-15	12:14:57.9	+36:13:08	2000	1227+365	2AC	1.56	256	1.3	1419.040	...	16
DDO 113	D	AO215	2008-08-17	12:14:57.9	+36:13:08	2000	1227+365	2AC	1.56	256	1.3	1419.020	...	17
MCG +09-20-131	B	AO215	2007-11-30	12:15:46.8	+52:23:17	2000	1219+484	2AD	1.56	256	1.3	1419.749 ^a	...	12
MCG +09-20-131	C	AO215	2008-05-05	12:15:46.8	+52:23:17	2000	1219+484	2AC	1.56	256	1.3	1419.566 ^a	...	15
MCG +09-20-131	D	AO215	2008-08-10	12:15:46.8	+52:23:17	2000	1219+484	2AC	1.56	256	1.3	1419.626 ^a	...	16
DDO 125	B	AO215	2007-11-25	12:27:40.9	+43:29:44	2000	1227+365	2AD	0.78	256	0.6	1419.588	...	12
DDO 125	C	AO215	2008-03-09	12:27:40.9	+43:29:44	2000	1227+365	2AC	0.78	256	0.6	1419.478	...	14
DDO 125	D	AO215	2008-08-06	12:27:40.9	+43:29:44	2000	1227+365	2AC	0.78	256	0.6	1419.410	...	16
DDO 125	D	AO215	2008-08-15	12:27:40.9	+43:29:44	2000	1227+365	2AC	0.78	256	0.6	1419.446	...	17
UGCA 292	B	AO215	2007-12-03	12:38:40.0	+32:46:01	2000	1227+365	2AD	0.78	256	0.6	1419.062	...	12
UGCA 292	C	AH927 ^b	2008-02-06	12:38:40.0	+32:46:01	2000	1227+365	2AC	0.78	256	0.6	1419.053	...	13

Table 2—Continued

(1) Galaxy	(2) Conf.	(3) Project	(4) Date [yyyy-mm-dd]	(5) RA [$^{\circ}$: $'$: $''$]	(6) Dec [$^{\circ}$: $'$: $''$]	(7) Equ.	(8) Cal	(9) Mode	(10) BW [MHz]	(11) Chan #	(12) Δv [km s^{-1}]	(13) ν_{obs1} [MHz]	(14) v_{obs1} [km s^{-1}]	(15) N_{EVLA}
UGCA 292	D	AO215	2008-07-11	12:38:40.0	+32:46:01	2000	1227+365	2AC	0.78	256	0.6	1418.865	...	16
UGCA 292	D	AO215	2008-08-16	12:38:40.0	+32:46:01	2000	1227+365	2AC	0.78	256	0.6	1418.892	...	17
UGCA 292	D	AH927 ^b	2008-07-21	12:38:40.0	+32:46:01	2000	1227+365	2AC	0.78	256	0.6	1418.874	...	16
GR 8	B	AO215	2007-11-12	12:58:40.4	+14:13:03	2000	1254+116	2AD	0.78	256	0.6	1419.485	...	11
GR 8	C	AH927 ^b	2008-02-10	12:58:40.4	+14:13:03	2000	1347+122	2AC	0.78	256	0.6	1419.524	...	13
GR 8	D	AO215	2008-08-02	12:58:40.4	+14:13:03	2000	1254+116	2AC	0.78	256	0.6	1419.285	...	16
GR 8	D	AO215	2008-08-17	12:58:40.4	+14:13:03	2000	1254+116	2AC	0.78	256	0.6	1419.304	...	17
GR 8	D	AH927 ^b	2008-08-02	12:58:40.4	+14:13:03	2000	1347+122	2AC	0.78	256	0.6	1419.287	...	16
UGC 8508	B	AO215	2007-12-10	13:30:44.4	+54:54:36	2000	1400+621	2AD	0.78	256	0.6	1420.190 ^a	...	12
UGC 8508	B	AH927 ^b	2008-02-09	13:30:44.4	+54:54:36	2000	1400+621	2AC	0.78	256	0.6	1420.175 ^a	...	13
UGC 8508	C	AO215	2008-03-15	13:30:44.4	+54:54:36	2000	1400+621	2AC	0.78	256	0.6	1420.102 ^a	...	14
UGC 8508	C	AH927 ^b	2008-05-31	13:30:44.4	+54:54:36	2000	1400+621	2AC	0.78	256	0.6	1420.062 ^a	...	15
UGC 8508	D	AO215	2008-07-31	13:30:44.4	+54:54:36	2000	1400+621	2AC	0.78	256	0.6	1420.060 ^a	...	16
UGC 8508	D	AH927 ^b	2008-08-03	13:30:44.4	+54:54:36	2000	1400+621	2AC	0.78	256	0.6	1420.071 ^a	...	16
UGC 8508	D	AO215	2008-08-17	13:30:44.4	+54:54:36	2000	1400+621	2AC	0.78	256	0.6	1420.084 ^a	...	17
DDO 181	B	AO215	2007-12-06	13:39:53.8	+40:44:21	2000	1331+305	2AD	1.56	256	1.3	1419.543 ^a	...	12
DDO 181	C	AO215	2008-03-09	13:39:53.8	+40:44:21	2000	1331+305	2AC	1.56	256	1.3	1419.474 ^a	...	14
DDO 181	D	AO215	2008-08-16	13:39:53.8	+40:44:21	2000	1331+305	2AC	1.56	256	1.3	1419.388 ^a	...	17
DDO 181	D	AO215	2008-08-18	13:39:53.8	+40:44:21	2000	1331+305	2AC	1.56	256	1.3	1419.390 ^a	...	17

Table 2—Continued

(1)	(2)	(3)	(4)	(5)	(6)	(7)	(8)	(9)	(10)	(11)	(12)	(13)	(14)	(15)
Galaxy	Conf.	Project	Date	RA	Dec	Equ.	Cal	Mode	BW	Chan	Δv	ν_{obs1}	v_{obs1}	N_{EVLA}
			[yyyy-mm-dd]	[$^{\text{h}}:^{\text{m}}:^{\text{s}}$]	[$^{\circ}:'''$]				[MHz]	#	[km s^{-1}]	[MHz]	[km s^{-1}]	
DDO 183	B	AO215	2007-12-08	13:50:50.6	+38:01:09	2000	1331+305	2AD	1.56	256	1.3	1419.591 ^a	...	12
DDO 183	C	AO215	2008-03-15	13:50:50.6	+38:01:09	2000	1331+305	2AC	1.56	256	1.3	1419.518 ^a	...	14
DDO 183	D	AO215	2008-08-11	13:50:50.6	+38:01:09	2000	1331+305	2AC	1.56	256	1.3	1419.433 ^a	...	16
DDO 183	D	AO215	2008-08-11	13:50:50.6	+38:01:09	2000	1331+305	2AC	1.56	256	1.3	1419.424 ^a	...	16
KKH 86	B	AO215	2007-11-11	13:54:33.5	+04:14:35	2000	1347+122	2AD	0.78	256	0.6	1419.105	...	11
KKH 86	C	AO215	2008-03-28	13:54:33.5	+04:14:35	2000	1347+122	2AC	0.78	256	0.6	1419.074	...	14
KKH 86	D	AO215	2008-08-08	13:54:33.5	+04:14:35	2000	1347+122	2AC	0.78	256	0.6	1418.944	...	16
UGC 8833	B	AO215	2007-11-18	13:54:48.7	+35:50:15	2000	1331+305	2AD	0.78	256	0.6	1419.406	...	12
UGC 8833	C	AZ121	2000-04-15	13:52:38.2	+36:04:60	1950	1413+349	2AD	1.56	128	2.6	...	225.0	0
UGC 8833	D	AO215	2008-08-05	13:54:48.7	+35:50:15	2000	1331+305	2AC	0.78	256	0.6	1419.265	...	16
UGC 8833	D	AO215	2008-08-15	13:54:48.7	+35:50:15	2000	1331+305	2AC	0.78	256	0.6	1419.259	...	17
KK 230	B ^c	AO215	2007-11-10	14:07:10.5	+35:03:37	2000	1331+305	2AD	0.78	256	0.6	1420.171 ^a	...	12
KK 230	C	AO215	2008-04-03	14:07:10.5	+35:03:37	2000	1331+305	2AC	0.78	256	0.6	1420.114 ^a	...	13
KK 230	D	AO215	2008-08-15	14:07:10.5	+35:03:37	2000	1331+305	2AC	0.78	256	0.65	1420.036 ^a	...	17
DDO 187	B	AO215	2007-11-17	14:15:56.5	+23:03:19	2000	1330+251	2AD	1.56	256	1.3	1419.751 ^a	...	13
DDO 187	B	AH927 ^b	2008-02-10	14:15:56.5	+23:03:19	2000	1330+251	2AC	1.56	256	1.3	1419.805 ^a	...	13
DDO 187	B	AH927 ^b	2008-02-12	14:15:56.5	+23:03:19	2000	1330+251	2AC	1.56	256	1.3	1419.805 ^a	...	13

Table 2—Continued

(1) Galaxy	(2) Conf.	(3) Project	(4) Date [yyyy-mm-dd]	(5) RA [$^{\circ}$: $'$: $''$]	(6) Dec [$^{\circ}$: $'$: $''$]	(7) Equ.	(8) Cal	(9) Mode	(10) BW [MHz]	(11) Chan #	(12) Δv [km s^{-1}]	(13) ν_{obs1} [MHz]	(14) v_{obs1} [km s^{-1}]	(15) N_{EVLA}
DDO 187	C	AO215	2008-03-28	14:15:56.5	+23:03:19	2000	1330+251	2AC	1.56	256	1.3	1419.704 ^a	...	14
DDO 187	C	AH927 ^b	2008-05-30	14:15:56.5	+23:03:19	2000	1330+251	2AC	1.56	256	1.3	1419.674 ^a	...	14
DDO 187	D	AH927 ^b	2008-08-05	14:15:56.5	+23:03:19	2000	1330+251	2AC	1.56	256	1.3	1419.580 ^a	...	16
DDO 187	D	AO215	2008-08-06	14:15:56.5	+23:03:19	2000	1330+251	2AC	1.56	256	1.3	1419.598 ^a	...	16
DDO 187	D	AO215	2008-08-16	14:15:56.5	+23:03:19	2000	1330+251	2AC	1.56	256	1.3	1419.588 ^a	...	17
DDO 190	B	AO215	2007-12-14	14:24:43.4	+44:31:33	2000	1506+375	2AD	0.78	256	0.6	1419.776	...	12
DDO 190	C	AZ121	2000-04-20	14:22:48.8	+44:44:60	1950	1413+349	2AD	1.56	128	2.6	...	160.0	12
DDO 190	D	AO215	2008-08-16	14:24:43.4	+44:31:33	2000	1506+375	2AC	0.78	256	0.6	1419.637	...	17
KKR 25	B	AO215	2008-01-31	16:13:47.9	+54:22:16	2000	1634+627	2AD	0.78	256	0.6	1421.112 ^a	...	13
KKR 25	C	AO215	2008-04-03	16:13:47.9	+54:22:16	2000	1634+627	2AC	0.78	256	0.6	1421.083 ^a	...	13
KKR 25	D	AO215	2008-08-07	16:13:47.9	+54:22:16	2000	1634+627	2AC	0.78	256	0.6	1421.035 ^a	...	16
KKR 25	D	AO215	2008-08-16	16:13:47.9	+54:22:16	2000	1634+627	2AC	0.78	256	0.6	1421.030 ^a	...	17
KKH 98	B	AO215	2007-12-07	23:45:34.0	+38:43:04	2000	0029+349	2AD	0.78	256	0.6	1420.954 ^a	...	12
KKH 98	C	AO215	2008-03-15	23:45:34.0	+38:43:04	2000	0029+349	2AC	0.78	256	0.6	1421.016 ^a	...	14
KKH 98	D	AO215	2008-07-10	23:45:34.0	+38:43:04	2000	0029+349	2AC	0.78	256	0.6	1421.150 ^a	...	16
KKH 98	D	AO215	2008-08-21	23:45:34.0	+38:43:04	2000	0029+349	2AC	0.78	256	0.6	1421.135 ^a	...	17

^aPotential MW Interference; offset flux calibrators^badditional data from the LITTLE THINGS survey

^cSource is named KKR 25 but is actually KK 230

Table 3. Properties of the VLA-ANGST Data Cubes.

(1)	(2)	(3)	(4)	(5)	(6)	(7)	(8)	(9)
Galaxy	Weighting	B_{major} [$''$]	B_{minor} [$''$]	BPA [$^{\circ}$]	Noise [mJy beam $^{-1}$]	Channel Width [km s $^{-1}$]	N_{pixels}	Pixel scale [$''$]
NGC 247	Natural	9.0	6.2	10.5	0.9	2.6	2048 ²	1.0
	Robust	6.5	4.8	12.7	0.9			
DDO 6	Natural	12.3	10.3	52.0	1.9	0.65	1024 ²	1.5
	Robust	7.2	6.3	49.0	2.1			
NGC 404	Natural	13.7	12.4	-34.7	0.9	2.6	1024 ²	1.5
	Robust	7.1	6.1	-32.6	0.9			
KKH 37 ^a	Natural	9.7	8.1	-86.2	1.6	0.65	1024 ²	1.5
	Robust	6.5	5.8	-66.9	1.8			
UGC 4483	Natural	12.2	9.8	61.3	0.5	2.6	1024 ²	1.5
	Robust	7.6	5.7	57.1	0.6			
KK 77 ^a	Natural	12.2	8.1	-79.0	0.9	2.6	1024 ²	1.5
	Robust	6.1	5.8	-66.6	0.7			
BK3N	Natural	12.0	8.1	-85.1	1.8	0.65	1024 ²	1.5
	Robust	6.3	5.8	61.5	1.8			
AO 0952+69	Natural	10.1	8.8	73.5	1.3	1.3	1024 ²	1.5
	Robust	6.4	5.9	-71.0	1.2			
Sextans B	Natural	15.0	14.1	10.5	0.8	1.3	1024 ²	1.5
	Robust	9.5	7.5	41.6	1.0			
NGC 3109	Natural	10.3	8.8	22.0	1.6	1.3	2048 ²	1.0
	Robust	7.6	5.0	8.8	1.7			
Antlia	Natural	14.1	13.9	-81.3	1.0	1.3	1024 ²	1.5
	Robust	10.5	9.6	71.1	1.2			
KDG 63 ^a	Natural	10.8	9.2	85.5	1.4	0.65	1024 ²	1.5
	Robust	6.2	6.0	77.0	1.6			
Sextans A	Natural	11.8	10.1	38.5	1.2	1.3	1024 ²	1.5
	Robust	7.3	6.0	35.1	1.3			
HS 117 ^a	Natural	13.2	8.5	-59.6	1.6	0.65	1024 ²	1.5
	Robust	8.6	6.1	-77.8	1.7			
DDO 82	Natural	9.3	7.7	-81.0	1.3	1.3	1024 ²	1.5
	Robust	5.8	5.7	65.0	1.4			

Table 3—Continued

(1)	(2)	(3)	(4)	(5)	(6)	(7)	(8)	(9)
Galaxy	Weighting	B_{major} [$''$]	B_{minor} [$''$]	BPA [$^{\circ}$]	Noise [mJy beam $^{-1}$]	Channel Width [km s $^{-1}$]	N_{pixels}	Pixel scale [$''$]
KDG 73	Natural	10.0	7.6	84.3	1.6	0.65	1024 ²	1.5
	Robust	6.9	5.6	65.2	1.7			
NGC 3741	Natural	7.6	6.2	81.1	1.0	1.3	1024 ²	1.5
	Robust	5.5	4.8	75.4	1.1			
DDO 99	Natural	12.4	7.6	-86.7	1.0	1.3	1024 ²	1.5
	Robust	7.7	5.2	72.5	1.1			
NGC 4163	Natural	12.3	10.4	-89.6	1.3	0.65	1024 ²	1.5
	Robust	7.6	5.4	-85.2	1.4			
NGC 4190	Natural	10.5	8.9	83.8	0.9	1.3	1024 ²	1.5
	Robust	6.1	5.3	81.4	1.0			
DDO 113 ^a	Natural	15.0	14.0	-55.2	1.4	1.3	1024 ²	1.5
	Robust	9.9	7.7	82.8	1.5			
MCG +09–20–131	Natural	9.7	7.4	69.7	1.0	1.3	1024 ²	1.5
	Robust	6.1	5.3	69.1	1.1			
DDO 125	Natural	11.5	10.6	-68.2	1.5	0.65	1024 ²	1.5
	Robust	6.3	5.4	-80.1	1.5			
UGCA 292	Natural	9.7	6.9	69.4	1.5	0.65	1024 ²	1.5
	Robust	7.0	5.0	65.2	1.6			
GR 8	Natural	7.6	7.3	-55.9	1.5	0.65	1024 ²	1.5
	Robust	5.8	5.4	-28.8	1.6			
UGC 8508	Natural	13.9	12.1	83.6	1.3	0.65	1024 ²	1.5
	Robust	8.2	6.4	86.1	1.5			
DDO 181	Natural	12.8	9.5	-75.7	1.0	1.3	1024 ²	1.5
	Robust	7.6	5.5	-80.4	1.1			
DDO 183	Natural	12.7	10.9	-76.7	1.1	1.3	1024 ²	1.5
	Robust	7.6	6.2	88.2	1.2			
KKH 86	Natural	11.0	9.9	-8.2	1.5	0.65	1024 ²	1.5
	Robust	7.5	5.8	-21.2	1.7			
UGC 8833	Natural	16.4	15.4	-87.4	0.6	2.6	1024 ²	1.5
	Robust	12.4	11.2	81.4	0.6			

Table 3—Continued

(1)	(2)	(3)	(4)	(5)	(6)	(7)	(8)	(9)
Galaxy	Weighting	B_{major}	B_{minor}	BPA	Noise	Channel Width	N_{pixels}	Pixel scale
		[$''$]	[$''$]	[$^{\circ}$]	[mJy beam $^{-1}$]	[km s $^{-1}$]		[$''$]
KK 230	Natural	8.2	7.3	-56.5	1.4	0.65	1024 ²	1.5
	Robust	5.9	5.2	-41.6	1.5			
DDO 187	Natural	12.2	10.4	-82.4	0.9	1.3	1024 ²	1.5
	Robust	7.1	5.7	88.5	1.0			
DDO 190	Natural	15.6	14.2	88.1	0.6	2.6	1024 ²	1.5
	Robust	10.8	9.9	84.1	0.6			
KKR 25 ^a	Natural	8.5	5.0	63.8	0.4	0.65	1024 ²	1.5
	Robust	5.5	4.4	65.0	0.4			
KKH 98	Natural	9.9	7.4	82.2	1.3	0.65	1024 ²	1.5
	Robust	6.2	5.2	80.4	1.4			

^aNon-detection

Table 4. Galaxy H I Properties.

(1) Galaxy	(2) S_{HI} [Jy km s ⁻¹]	(3) M_{HI} [10 ⁶ M _⊙]	(4) $S_{\text{HI}}^{\text{SD}}$ [Jy km s ⁻¹]	(5) w_{20} [km s ⁻¹]	(6) w_{50} [km s ⁻¹]	(7) v_{cen} [km s ⁻¹]	(8) Peak N_{HI} [10 ²¹ cm ⁻²]
NGC 247	382.6	1106.2	608 ^a	201.3	193.9	163.7	5.4
DDO 6	1.2	3.2	3.7 ^b	20.9	13.7	292.5	0.9
NGC 404 ^c	66.7	146.4	76 ^d	80.5	63.2	-54.0	0.5
KKH 37 ^e	< 3.4	< 0.8	1.8 ^{f,g}	< 0.08
UGC 4483	12.0	32.8	13.6 ^h	51.2	34.3	153.9	3.2
KK 77 ^e	< 4.4	< 2.3	< 5.5 ⁱ	< 0.06
BK 3N	6.3	22.0	< 0.75 ^j	44.4	20.0	-42.5	0.7
AO 0952+69 ^k	61.3	206.6	< 0.59 ^j	56.0	45.6	112.8	1.3
Sextans B	91.0	41.5	72.9 ^h	58.1	40.6	302.2	2.6
NGC 3109	720.9	270.1	1148 ^a	127.7	116.0	405.1	6.6
Antlia	1.4	0.5	1.7 ^l	23.4	13.4	363.4	0.3
KDG 63 ^e	< 4.2	< 1.1	< 0.2 ^m	< 0.06
Sextans A	138.1	62.1	169 ^a	59.8	46.2	324.8	6.1
HS 117 ^e	< 1.7	< 0.6	< 0.03
DDO 82	0.8	2.8	< 0.62 ^j	35.8	26.7	56.2	0.9
KDG 73	0.1	0.5	1.0 ^h	9.2	8.5	116.3	0.1
NGC 3741	32.8	81.1	44.6 ^o	85.4	70.6	229.1	3.4
DDO 99	29.7	46.9	47.1 ^o	51.6	28.6	242.1	2.6
NGC 4163	4.8	9.3	9.6 ^p	33.5	22.7	161.6	2.1
NGC 4190	15.5	44.8	23.2 ^p	73.2	52.8	227.0	3.5
DDO 113 ^e	< 1.6	< 0.4	23.6 ^p	< 0.04
MCG +09-20-131	3.1	11.9	5.2 ^q	39.0	26.1	157.6	3.3

Table 4—Continued

(1)	(2)	(3)	(4)	(5)	(6)	(7)	(8)
Galaxy	S_{HI} [Jy km s ⁻¹]	M_{HI} [10 ⁶ M_{\odot}]	$S_{\text{HI}}^{\text{SD}}$ [Jy km s ⁻¹]	w_{20} [km s ⁻¹]	w_{50} [km s ⁻¹]	v_{cen} [km s ⁻¹]	Peak N_{HI} [10 ²¹ cm ⁻²]
DDO 125	18.3	28.7	21.8 ^h	39.7	27.0	196.1	2.1
UGCA 292	12.9	40.0	14.3 ^h	37.1	25.2	308.3	4.2
GR 8	5.8	5.9	7.8 ^h	30.7	21.4	213.7	1.7
UGC 8508	12.3	19.3	14.8 ^p	62.7	48.1	59.8	2.9
DDO 181	10.5	24.4	12.5 ^o	52.1	40.8	201.4	1.7
DDO 183	8.2	20.1	9.6 ^p	42.2	26.4	191.2	2.2
KKH 86	0.1	0.1	0.5 ^h	7.7	6.9	285.5	0.2
UGC 8833	5.9	13.1	6.0 ^h	41.0	29.4	225.9	2.2
KK 230	0.8	0.7	2.6 ^h	17.4	11.5	60.6	0.6
DDO 187	10.1	11.6	12.0 ^h	46.0	31.8	152.2	3.2
DDO 190	22.5	41.3	8.5 ^o	62.3	45.2	148.8	3.6
KKR 25 ^e	< 1.0	< 0.1	2.2 ^{r g}	< 0.03
KKH 98	2.2	3.3	4.1 ^h	25.5	17.0	-137.8	0.8

^r Huchtmeier et al. (2000)

^aHuchtmeier & Richter (1989)

^bMeyer et al. (2004)

^cNGC 404 is contaminated by foreground Milky Way H I emission.

^dBaars & Wendker (1976)

^eVLA-ANGST non-detection. Limits based on a width of 20 km s⁻¹ and the optical diameter D_{25} .

- ^fKarachentsev et al. (2001)
- ^gmight be Galactic H I
- ^hHuchtmeier et al. (2003)
- ⁱHuchtmeier et al. (2000)
- ^jvan Driel et al. (1998)
- ^kAO 0952+62 is contaminated by M81 tidal HI emission.
- ^lBarnes & de Blok (2001)
- ^mSchneider et al. (1990)
- ⁿBarnes & de Blok (2004)
- ^oSpringob et al. (2005)
- ^pKoribalski et al. (2004)
- ^qPustilnik & Martin (2007)

We thank the National Radio Astronomy Observatory for their generous time allocation, observing, and data reduction support for this Large Project. The National Radio Astronomy Observatory is a facility of the National Science Foundation operated under cooperative agreement by Associated Universities, Inc. Support for this work was provided by the National Science Foundation collaborative research grant ‘Star Formation, Feedback, and the ISM: Time Resolved Constraints from a Large VLA Survey of Nearby Galaxies,’ grant number AST-0807710. This material is based on work supported by the National Science Foundation under Grant No. DGE-0718124. SRW is grateful for support from a Penrose Fellowship, a University of Minnesota Degree Dissertation Fellowship, and a NRAO Research Fellowship number 807515. We would like to thank the LITTLE THINGS and THINGS teams for collaboration on the calibration and imaging pipeline. We have made use of the NASA/IPAC Extragalactic Database (NED), which is operated by the Jet Propulsion Laboratory, California Institute of Technology, under contract with NASA. This research has also made use of NASA’s Astrophysics Data System (ADS).

Facilities: VLA, HST

REFERENCES

- Allen, R. J., Ivette Rodríguez, M., Black, J. H., & Booth, R. S. 2012, *AJ*, 143, 97
- Baars, J. W. M., & Wendker, H. J. 1976, *A&A*, 48, 405
- Barnes, D. G., & de Blok, W. J. G. 2001, *AJ*, 122, 825
- Barnes, D. G., & de Blok, W. J. G. 2004, *MNRAS*, 351, 333
- Begum, A., Chengalur, J. N., Karachentsev, I. D., Sharina, M. E., & Kaisin, S. S. 2008, *MNRAS*, 386, 1667
- Bigiel, F., Leroy, A., Walter, F., Brinks, E., de Blok, W. J. G., Madore, B., & Thornley, M. D. 2008, *AJ*, 136, 2846
- Braun, R. 2012, *ApJ*, 749, 87
- Briggs, D. S. 1995, *Bulletin of the American Astronomical Society*, 27, #112.02
- Cannon, J. M., Dohm-Palmer, R. C., Skillman, E. D., Bomans, D. J., Côté, S., & Miller, B. W. 2003, *AJ*, 126, 2806
- Cannon, J. M., Giovanelli, R., Haynes, M. P., et al. 2011, *ApJ*, 739, L22
- Cannon, J. M., Most, H. P., Skillman, E. D., et al. 2011, *ApJ*, 735, 36
- Clark, B. G. 1980, *A&A*, 89, 377
- Crnojević, D., Grebel, E. K., & Cole, A. A. 2011, *A&A*, 530, A59
- Dale, D. A., et al. 2009, *ApJ*, 703, 517
- Dalcanton, J. J., et al. 2009, *ApJS*, 183, 67

- de Vaucouleurs, G., de Vaucouleurs, A., Corwin, H. G., Jr., Buta, R. J., Paturel, G., & Fouqué, P. 1991, *Third Reference Catalogue of Bright Galaxies* (New York: Springer)
- Dickey, J. M., Brinks, E., & Puche, D. 1992, *ApJ*, 385, 501
- Dohm-Palmer, R. C., Skillman, E. D., Mateo, M., Saha, A., Dolphin, A., Tolstoy, E., Gallagher, J. S., & Cole, A. A. 2002, *AJ*, 123, 813
- Heald, G., Józsa, G., Serra, P., et al. 2011, *A&A*, 526, A118
- Helfer, T. T., Thornley, M. D., Regan, M. W., et al. 2003, *ApJS*, 145, 259
- Huchtmeier, W. K., & Richter, O.-G. 1989, *A General Catalog of HI Observations of Galaxies. The Reference Catalog.* Huchtmeier, W.K., Richter, O.-G., pp. 350. ISBN 0-387-96997-7. Springer-Verlag Berlin Heidelberg 1989
- Huchtmeier, W. K., Karachentsev, I. D., Karachentseva, V. E., & Ehle, M. 2000, *A&AS*, 141, 469
- Huchtmeier, W. K., Karachentsev, I. D., & Karachentseva, V. E. 2000, *A&AS*, 147, 187
- Huchtmeier, W. K., Karachentsev, I. D., & Karachentseva, V. E. 2003, *A&A*, 401, 483
- Hunter, D. A., Brinks, E., Elmegreen, B., Rupen, M., Simpson, C., Walter, F., Westpfahl, D., & Young, L. 2007, *Bulletin of the American Astronomical Society*, 38, 895
- Jörsäter, S., & van Moorsel, G. A. 1995, *AJ*, 110, 2037
- Karachentsev, I. D., Karachentseva, V. E., &
- Karachentsev, I. D., Karachentseva, V. E., Huchtmeier, W. K., & Makarov, D. I. 2004, *AJ*, 127, 2031
- Kennicutt, R. C., Jr. 1989, *ApJ*, 344, 685

- Kennicutt, R. C., Jr. 1998, *ARA&A*, 36, 189
- Kennicutt, R. C., Jr., et al. 2003, *PASP*, 115, 928
- Kennicutt, R. C., Calzetti, D., Aniano, G., et al. 2011, *PASP*, 123, 1347
- Koribalski, B. S., Staveley-Smith, L., Kilborn, V. A., et al. 2004, *AJ*, 128, 16
- Koribalski, B. S. 2008, *Galaxies in the Local Volume*, 41
- Lee, J. C., Kennicutt, R. C., Funes, J. G., Sakai, S., Tremonti, C. A., & van Zee, L. 2004, *Bulletin of the American Astronomical Society*, 36, 1442
- Lee, J. C., et al. 2011, *ApJS*, 192, 6
- Leroy, A. K., Walter, F., Brinks, E., Bigiel, F., de Blok, W. J. G., Madore, B., & Thornley, M. D. 2008, *AJ*, 136, 2782
- Leroy, A. K., Walter, F., Bigiel, F., et al. 2009, *AJ*, 137, 4670
- McQuinn, K. B. W., Skillman, E. D., Cannon, J. M., et al. 2010, *ApJ*, 721, 297
- Meyer, M. J., Zwaan, M. A., Webster, R. L., et al. 2004, *MNRAS*, 350, 1195
- Pustilnik, S. A., & Martin, J.-M. 2007, *A&A*, 464, 859
- Rahman, N., Bolatto, A. D., Xue, R., et al. 2012, *ApJ*, 745, 183
- Rohlfs, K., & Wilson, T. L. 2004, *Tools of radio astronomy*, 4th rev. and enl. ed., by K. Rohlfs and T.L. Wilson. Berlin: Springer, 2004
- Schneider, S. E., Thuan, T. X., Magri, C., & Wadiak, J. E. 1990, *ApJS*, 72, 245
- Skillman, E. D. 1987, *NASA Conference Publication*, 2466, 263
- Springob, C. M., Haynes, M. P., Giovanelli, R., & Kent, B. R. 2005, *ApJS*, 160, 149

Stilp, A. M., et al. 2012, in preparation

van der Hulst, J. M., van Albada, T. S., & Sancisi, R. 2001, *Gas and Galaxy Evolution*, 240, 451

van Driel, W., Kraan-Korteweg, R. C., Binggeli, B., & Huchtmeier, W. K. 1998, *A&AS*, 127, 397

Warren, S. R., Weisz, D. R., Skillman, E. D., et al. 2011, *ApJ*, 738, 10

Warren, S. R., Skillman, E. D., Stilp, A. M., Dalcanton, J. J., Ott, J., Walter, F., Petersen, E. A., koribalski, B., & West, A. A. 2012, *ApJ*, submitted

Walter, F., Brinks, E., de Blok, W. J. G., Bigiel, F., Kennicutt, R. C., Thornley, M. D., & Leroy, A. 2008, *AJ*, 136, 2563

Weisz, D. R., Skillman, E. D., Cannon, J. M., Dolphin, A. E., Kennicutt, R. C., Jr., Lee, J., & Walter, F. 2008, *ApJ*, 689, 160

Weisz, D. R., Dalcanton, J. J., Williams, B. F., et al. 2011, *ApJ*, 739, 5

Williams, B. F., Dalcanton, J. J., Stilp, A., et al. 2010, *ApJ*, 709, 135

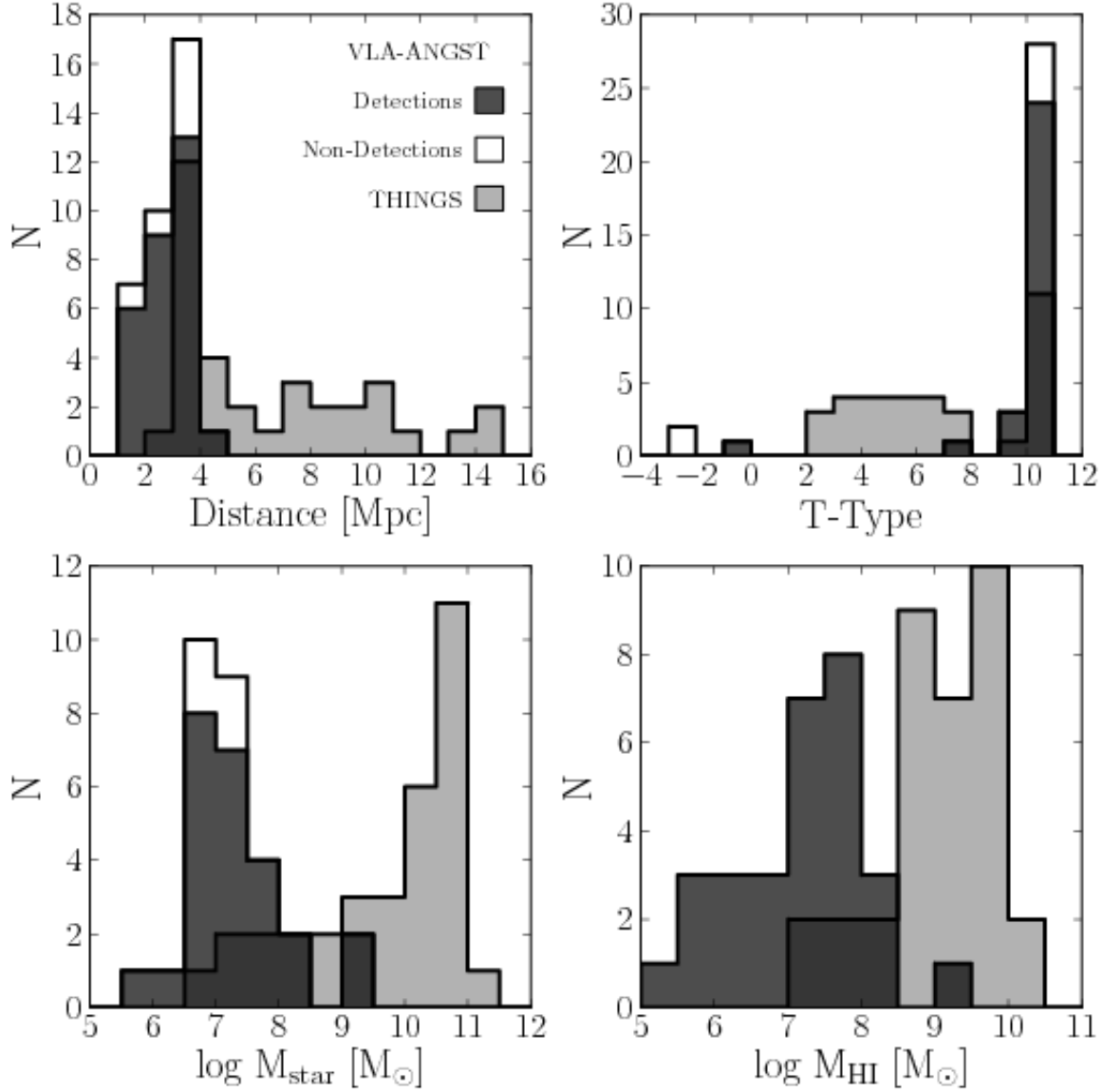


Fig. 1.— VLA-ANGST galaxy distribution across distance (upper left), T-Type (upper right), logarithmic stellar mass (lower left), and logarithmic H I mass (lower right). Galaxies that are detected in VLA-ANGST are shown in medium gray bins and non-detections, colored white, add to the distribution. THINGS galaxies are shown in light gray and the VLA-ANGST and THINGS overlap areas in dark gray color.

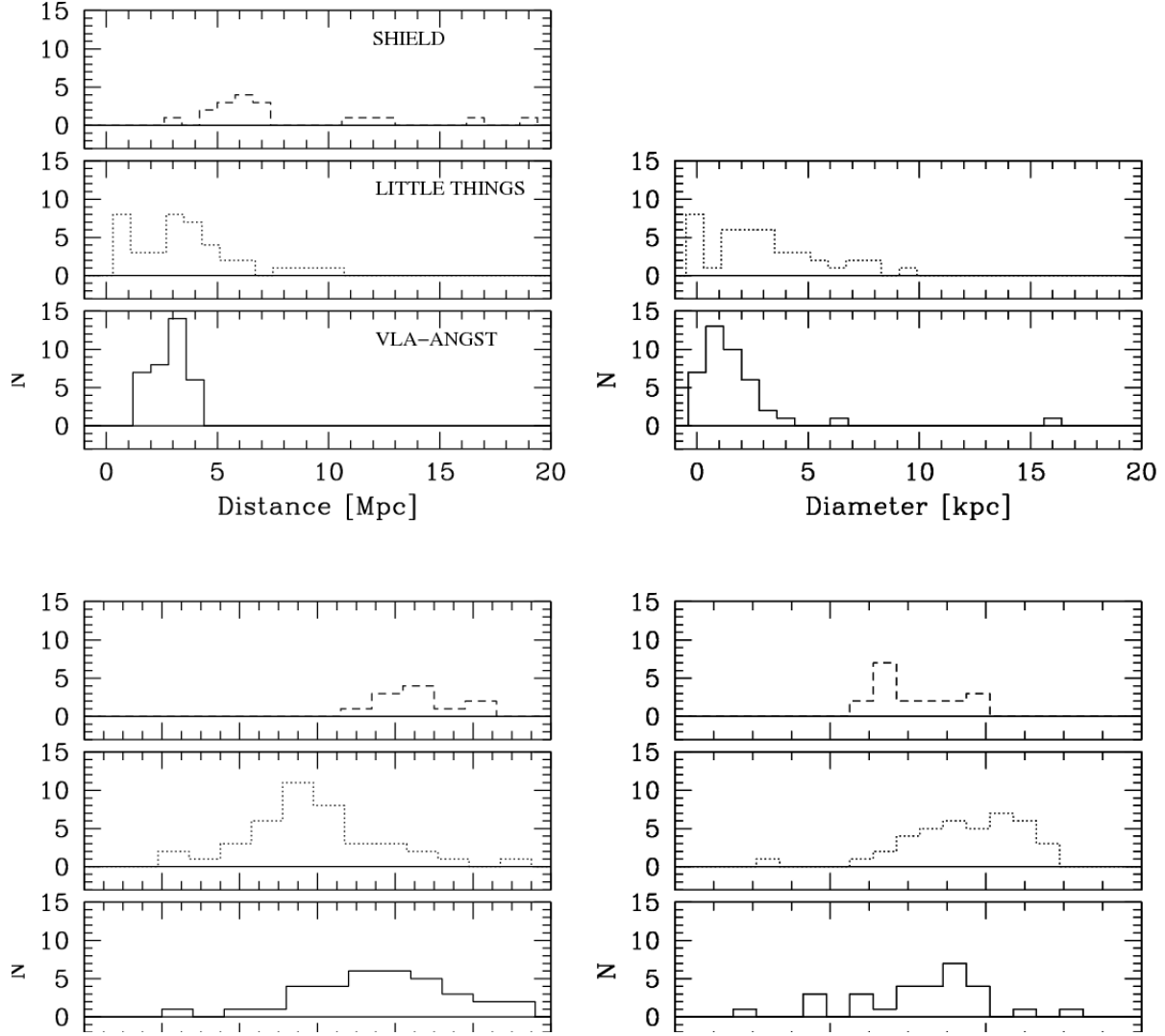


Fig. 2.— Comparison of VLA-ANGST galaxy properties (*solid*) with the LITTLE THINGS (*dotted*) and SHIELD (*dashed*) samples. Clockwise from the upper left: Distance, Diameter (D_{25} for VLA-ANGST, Holmberg diameter for LITTLE THINGS, no information on SHIELD targets), logarithmic H I masses, and optical absolute B magnitudes.

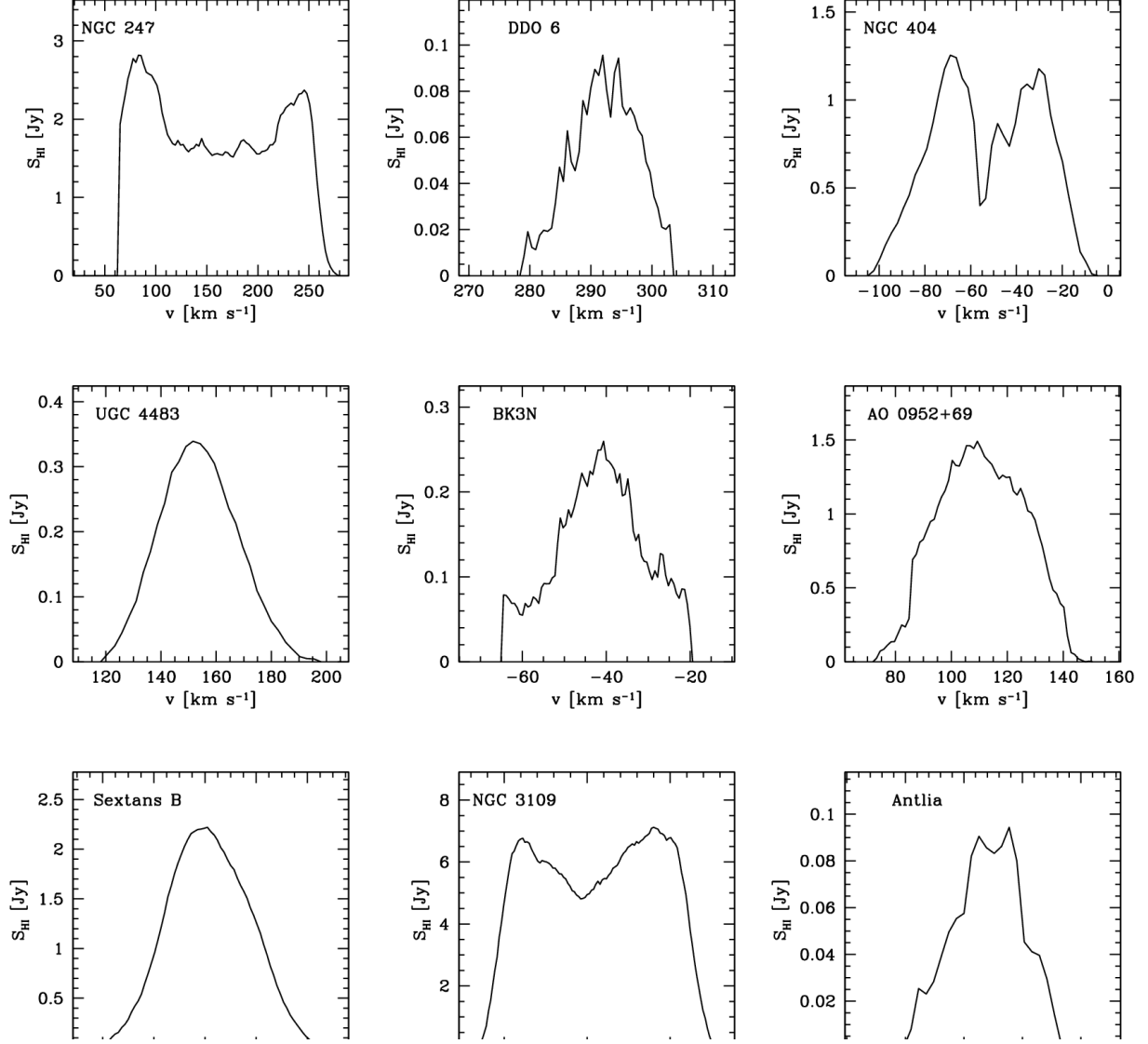


Fig. 3.— Spatially integrated H I spectra of the VLA-ANGST galaxies.

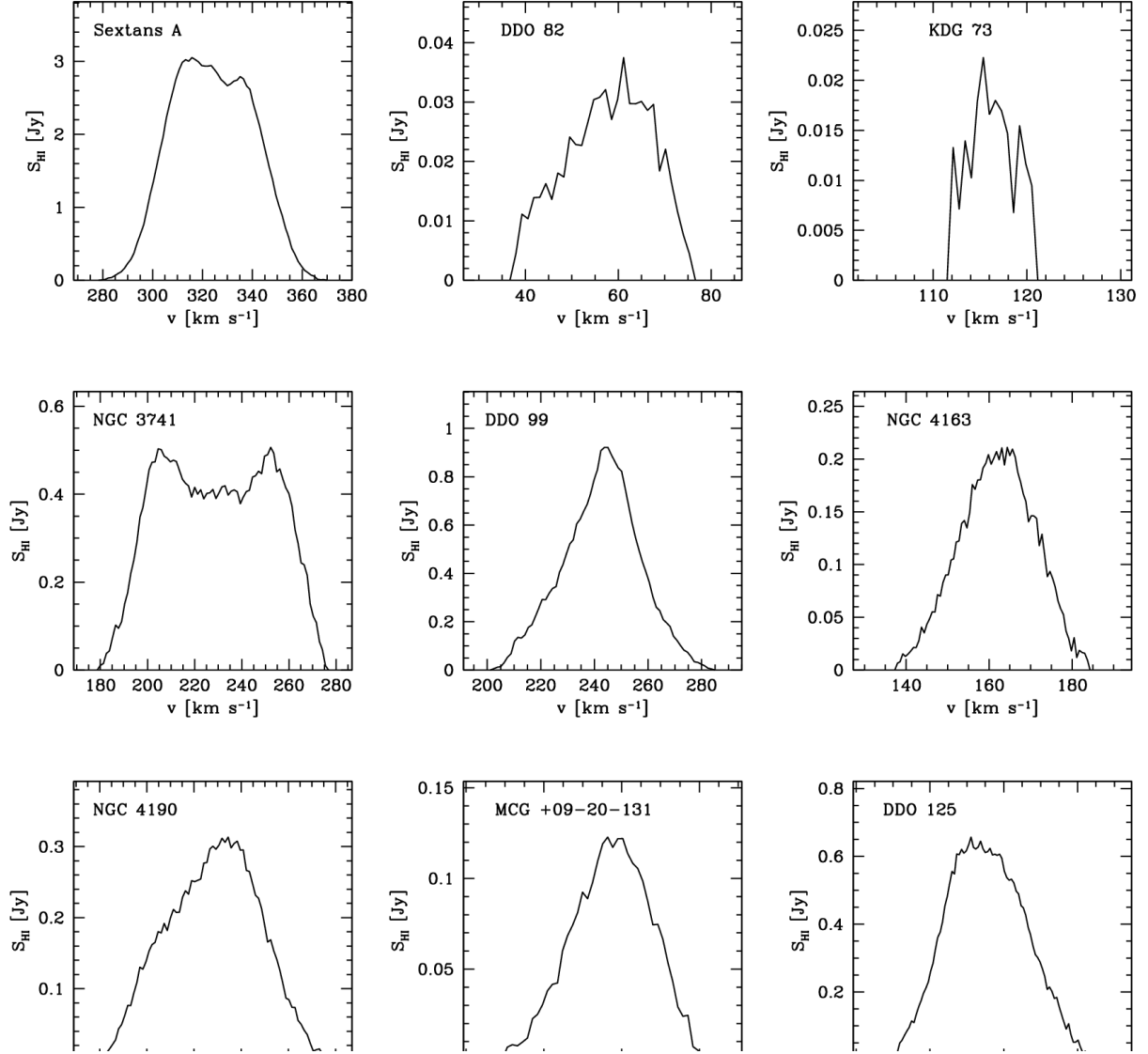


Fig. 3.— continued.

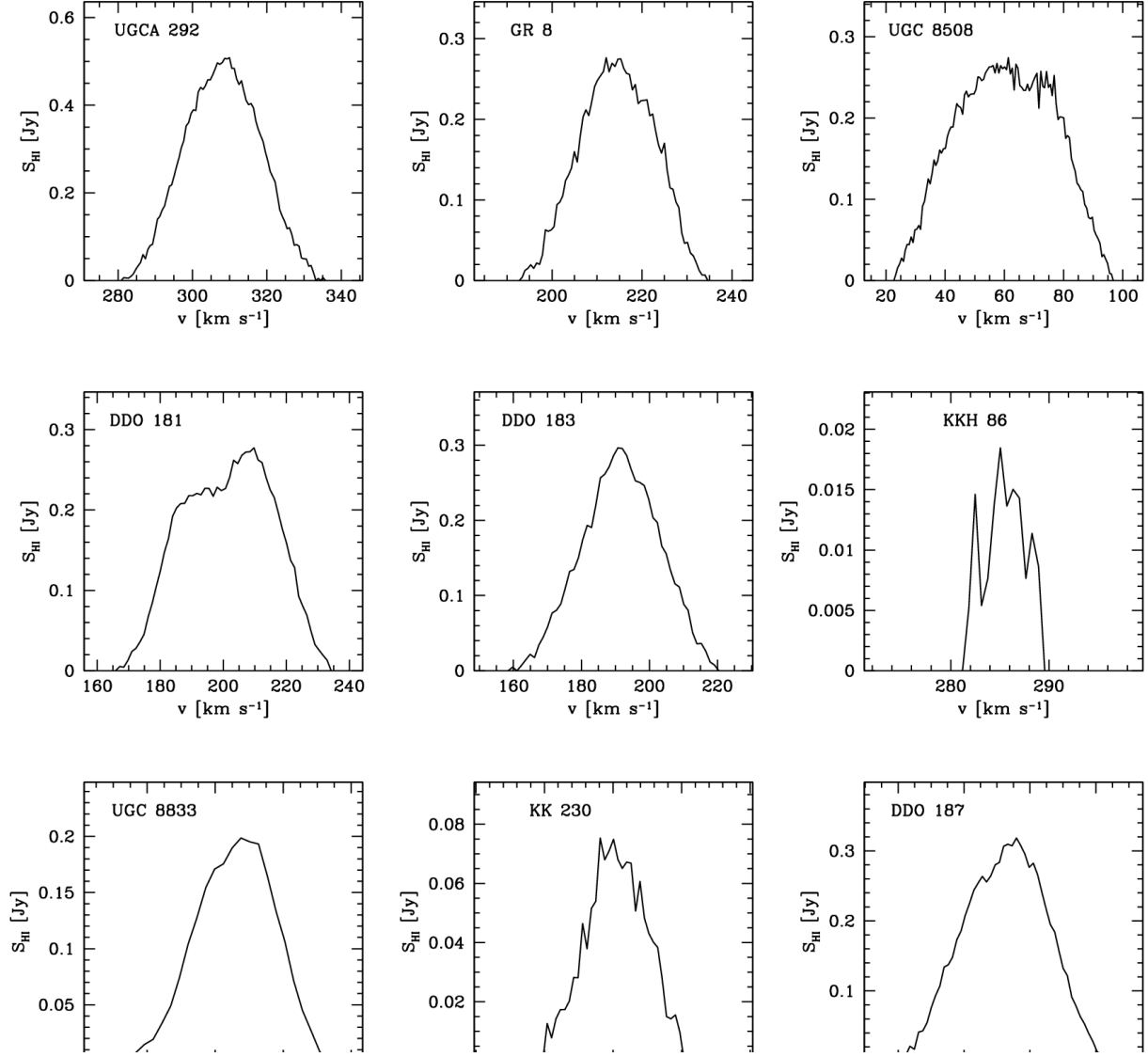


Fig. 3.— continued.

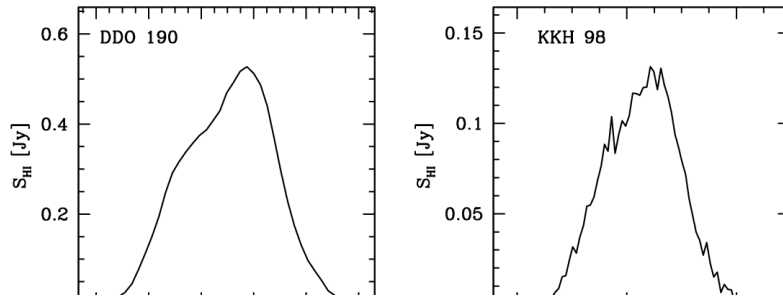


Fig. 3.— continued.

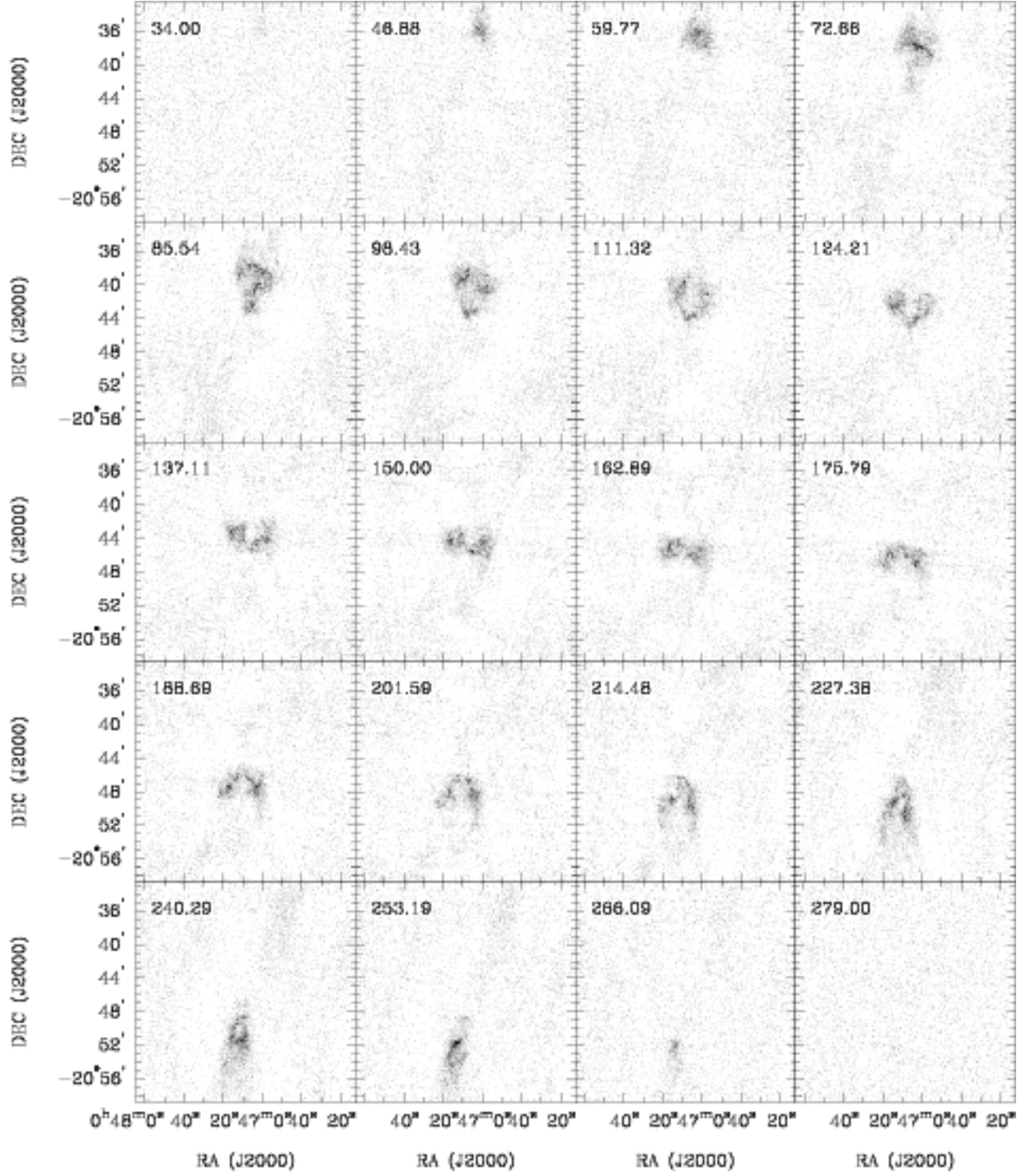


Fig. 4.— NGC 247: Channel maps based on the natural-weighted cube (grayscale range: -0.02 to $12.2 \text{ mJy beam}^{-1}$). Every fourth channel is shown (channel width 2.6 km s^{-1}) and each map has the same size as the moment maps in the following panels.

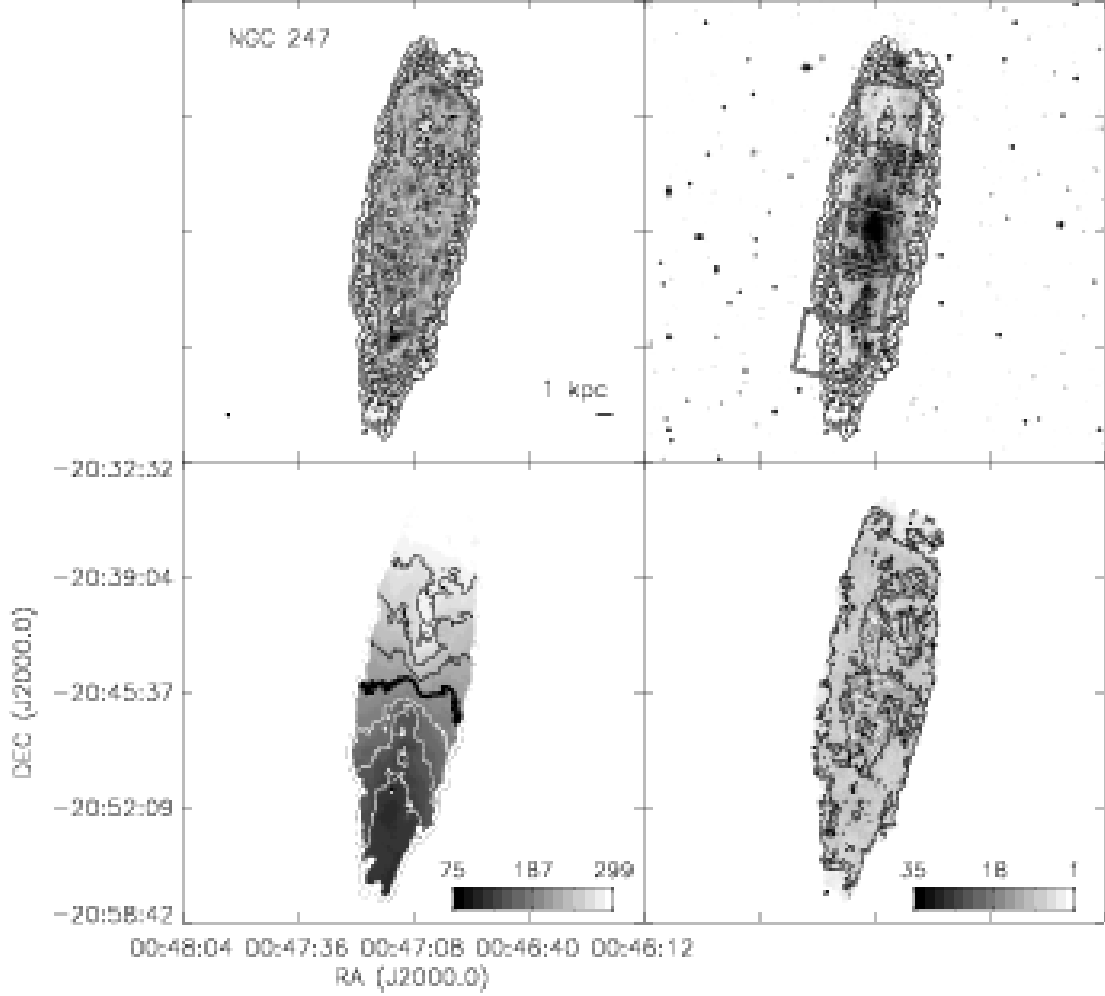


Fig. 4.— continued. *Top left:* The integrated H I intensity map for NGC 247. The grayscale covers a range from 1×10^{19} to $5.4 \times 10^{21} \text{ cm}^{-2}$ with contours of 1×10^{20} , 5×10^{20} , 1×10^{21} , and $5 \times 10^{21} \text{ cm}^{-2}$. *Top Right:* An optical 4680 Å image from the DSS with the same column density contours overlaid. The HST ACS footprints are the fields covered by the ANGST survey. *Bottom Left:* The H I velocity field. Black contours (lighter grayscale) indicate approaching emission, white contours (darker grayscale) receding emission. The thick black contour is the central velocity ($v_{cen} = 163.7 \text{ km s}^{-1}$) and the isovelocity contours are spaced by $\Delta v = 25 \text{ km s}^{-1}$. *Bottom Right:* The H I velocity dispersion. Contours are plotted at 5, 10, 15, and 20 km s^{-1} . Colorbars are in units of km s^{-1} .

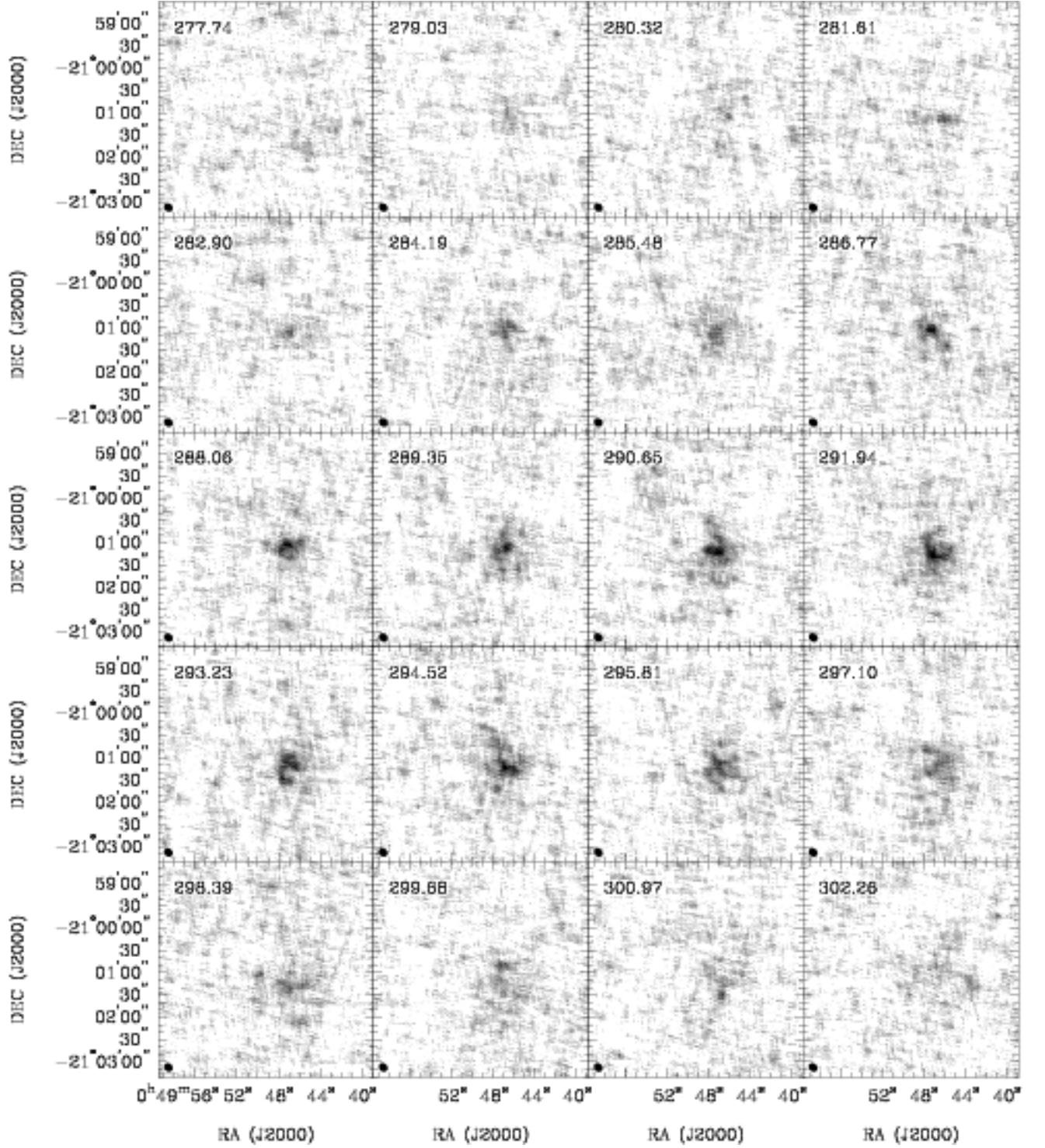


Fig. 5.— **DDO 6:** Channel maps based on the natural-weighted cube (grayscale range: -0.02 to $13.3 \text{ mJy beam}^{-1}$). Every channel is shown (channel width 0.6 km s^{-1}) and each map has the same size as the moment maps in the following panels.

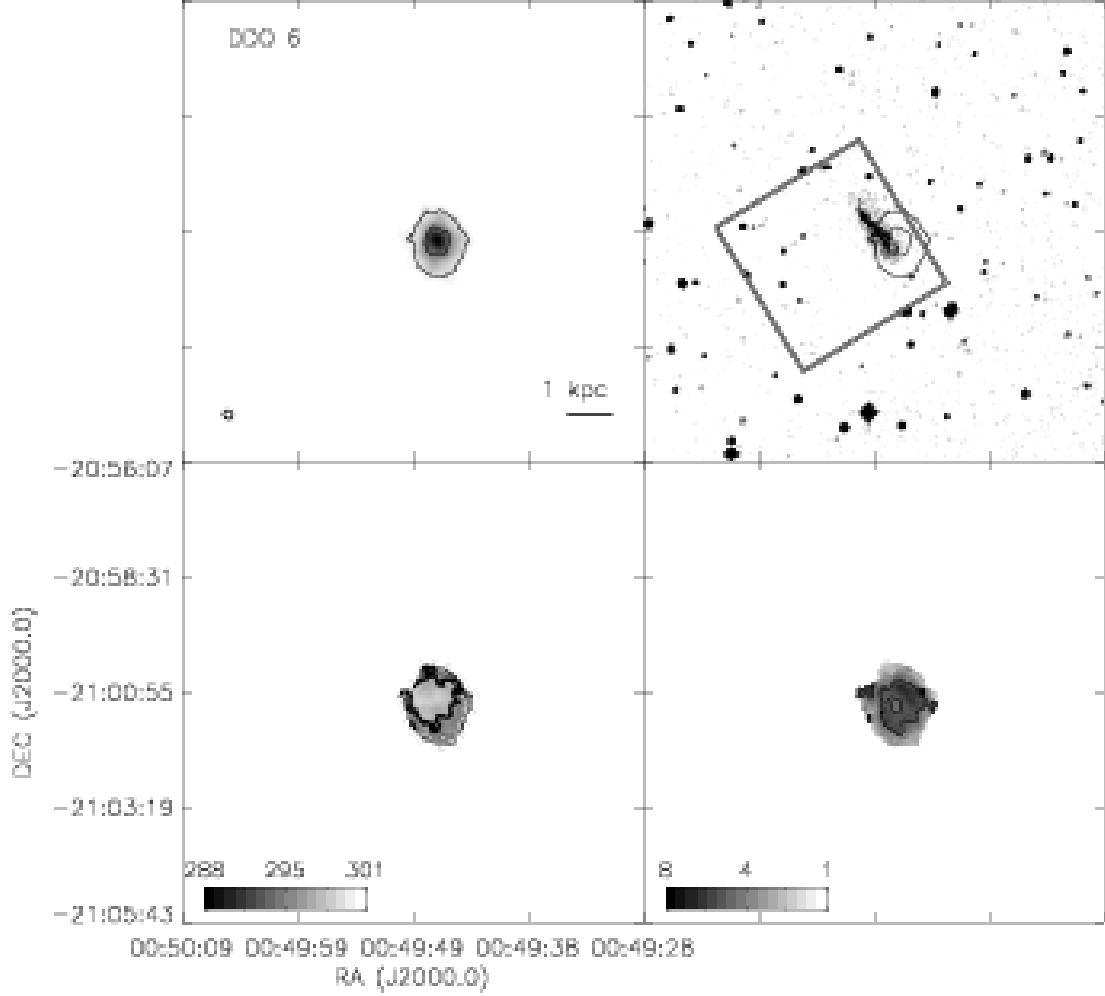


Fig. 5.— continued. *Top left:* The integrated H I intensity map for DDO 6. The grayscale covers a range from 1×10^{19} to $9.4 \times 10^{20} \text{ cm}^{-2}$ with contours of 1×10^{20} and $5 \times 10^{20} \text{ cm}^{-2}$. *Top Right:* An optical 4680 Å image from the DSS with the same column density contours overlaid. The HST ACS footprint is the field covered by the ANGST survey. *Bottom Left:* The H I velocity field. Black contours (lighter gray scale) indicate approaching emission, white contours (darker gray scale) receding emission. The thick black contour is the central velocity ($v_{\text{cen}} = 292.5 \text{ km s}^{-1}$) and the isovelocity contours are spaced by $\Delta v = 3 \text{ km s}^{-1}$. *Bottom Right:* The H I velocity dispersion. A contour is plotted at 5 km s^{-1} . Colorbars are in units of km s^{-1} .

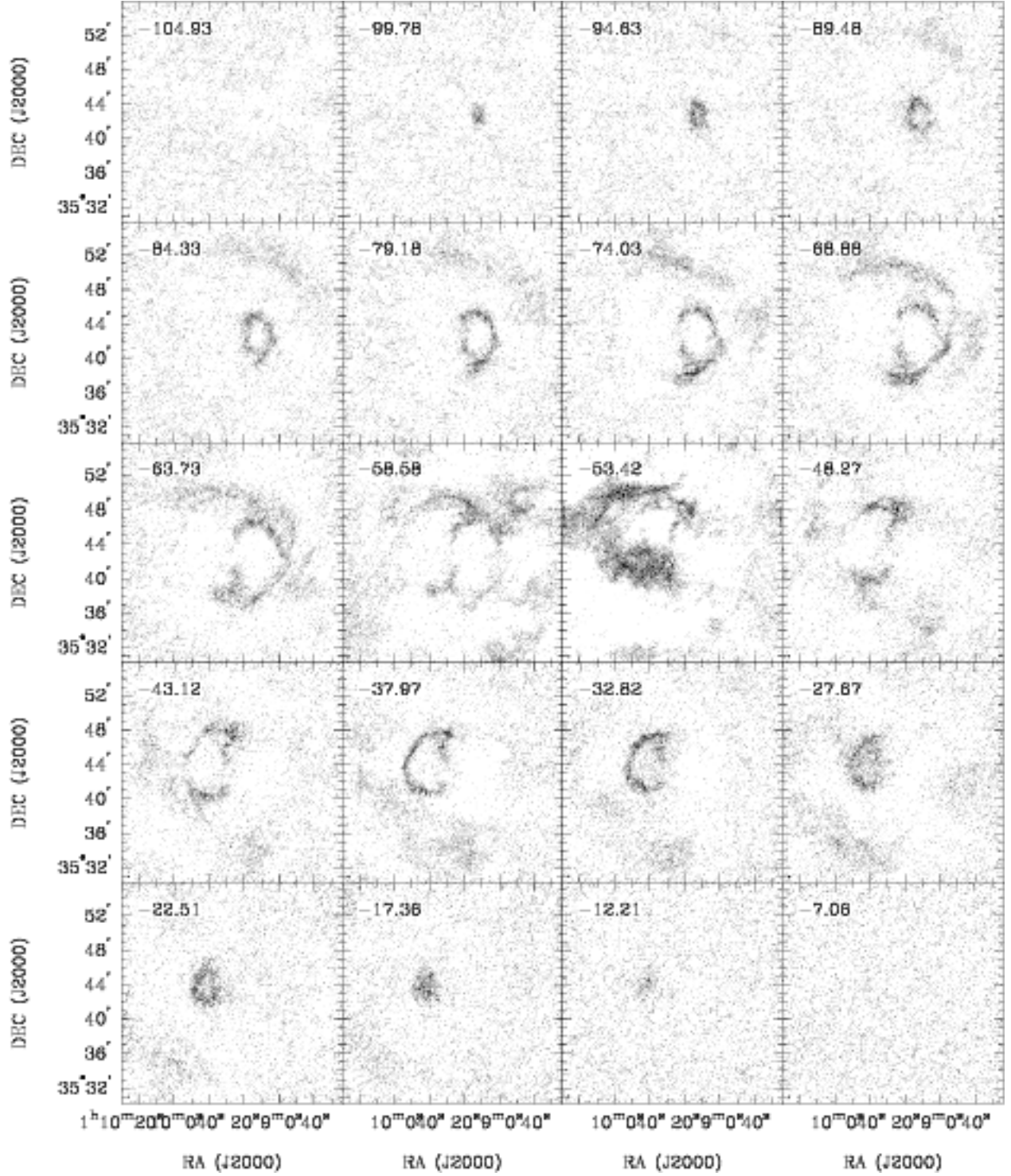


Fig. 6.— **NGC 404:** Channel maps based on the natural-weighted cube (grayscale range: -0.02 to $8.5 \text{ mJy beam}^{-1}$). Every channel is shown (channel width 2.6 km s^{-1}) and each map has the same size as the moment maps in the following panels. Confusion with H I emission from the Milky Way is present in this galaxy between velocities -58 to -50 km s^{-1} and can be seen in two of the above channels.

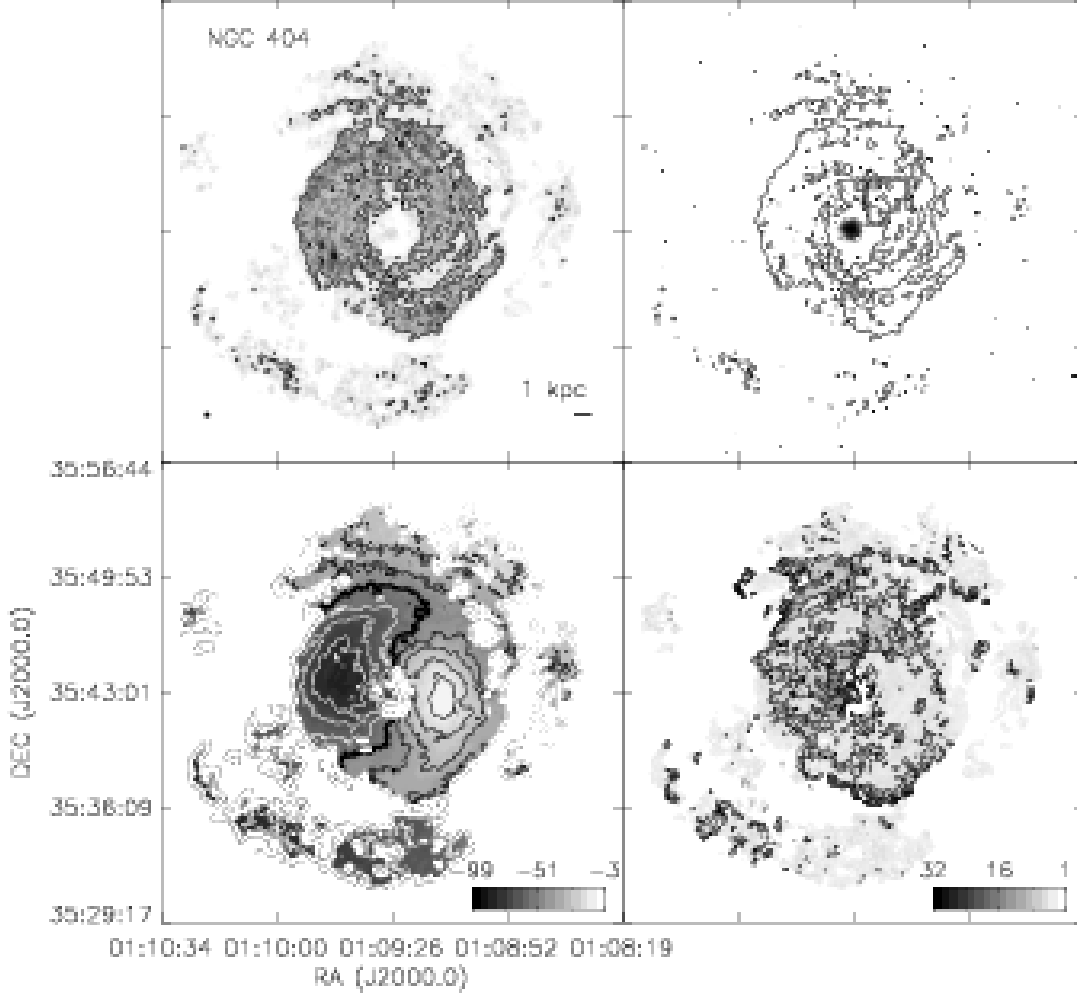


Fig. 6.— continued. *Top left:* The integrated H I intensity map for NGC 404. The grayscale covers a range from 1×10^{19} to $5.0 \times 10^{20} \text{ cm}^{-2}$ with contours of $1 \times 10^{20} \text{ cm}^{-2}$ and $5 \times 10^{20} \text{ cm}^{-2}$. *Top Right:* An optical 6450 Å image from the DSS with the same column density contours overlaid. The HST WFPC2 footprint is the field covered by the ANGST survey. The bright, large disk in the lower right is a foreground star. *Bottom Left:* The H I velocity field. Black contours (lighter gray scale) indicate approaching emission, white contours (darker gray scale) receding emission. The thick black contour is the central velocity ($v_{cen} = -54.0 \text{ km s}^{-1}$) and the isovelocity contours are spaced by $\Delta v = 10 \text{ km s}^{-1}$. *Bottom Right:* The H I velocity dispersion. Contours are plotted at 5, 10, 15, and 20 km s^{-1} . Colorbars are in units of km s^{-1} .

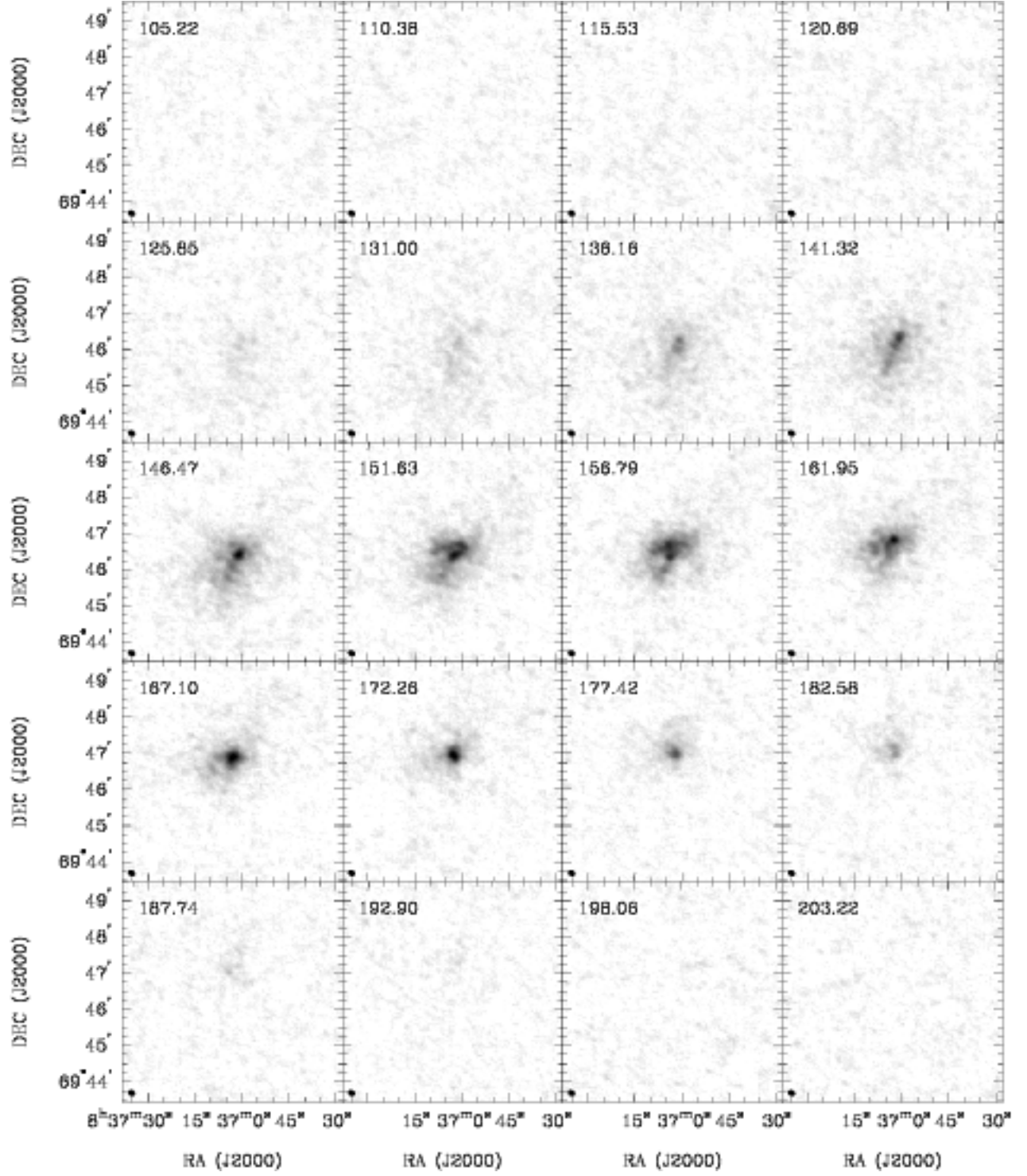


Fig. 7.— **UGC 4483**: Channel maps based on the natural-weighted cube (grayscale range: -0.02 to $14.8 \text{ mJy beam}^{-1}$). Every channel is shown (channel width 2.6 km s^{-1}) and each map has the same size as the moment maps in the following panels.

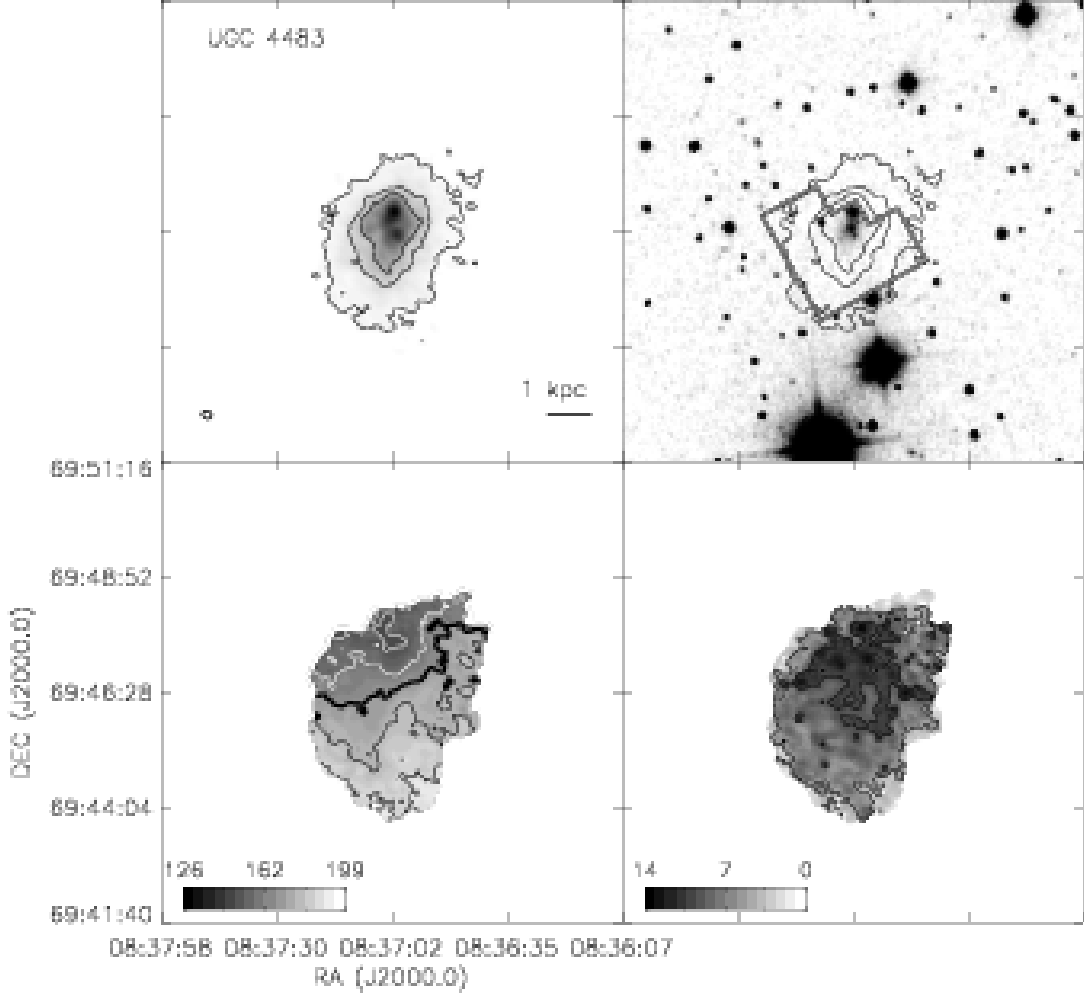


Fig. 7.— continued. *Top left:* The integrated H I intensity map for UGC 4483. The grayscale covers a range from 1×10^{19} to $3.2 \times 10^{21} \text{ cm}^{-2}$ with contours of 1×10^{20} , 5×10^{20} , and $1 \times 10^{21} \text{ cm}^{-2}$. *Top Right:* An optical 6450 Å image from the DSS with the same column density contours overlaid. The HST WFPC2 footprint is the field covered by the ANGST survey. *Bottom Left:* The H I velocity field. Black contours (lighter gray scale) indicate approaching emission, white contours (darker gray scale) receding emission. The thick black contour is the central velocity ($v_{cen} = 153.9 \text{ km s}^{-1}$) and the isovelocity contours are spaced by $\Delta v = 10 \text{ km s}^{-1}$. *Bottom Right:* The H I velocity dispersion. Contours are plotted at 5 and 10 km s^{-1} . Colorbars are in units of km s^{-1} .

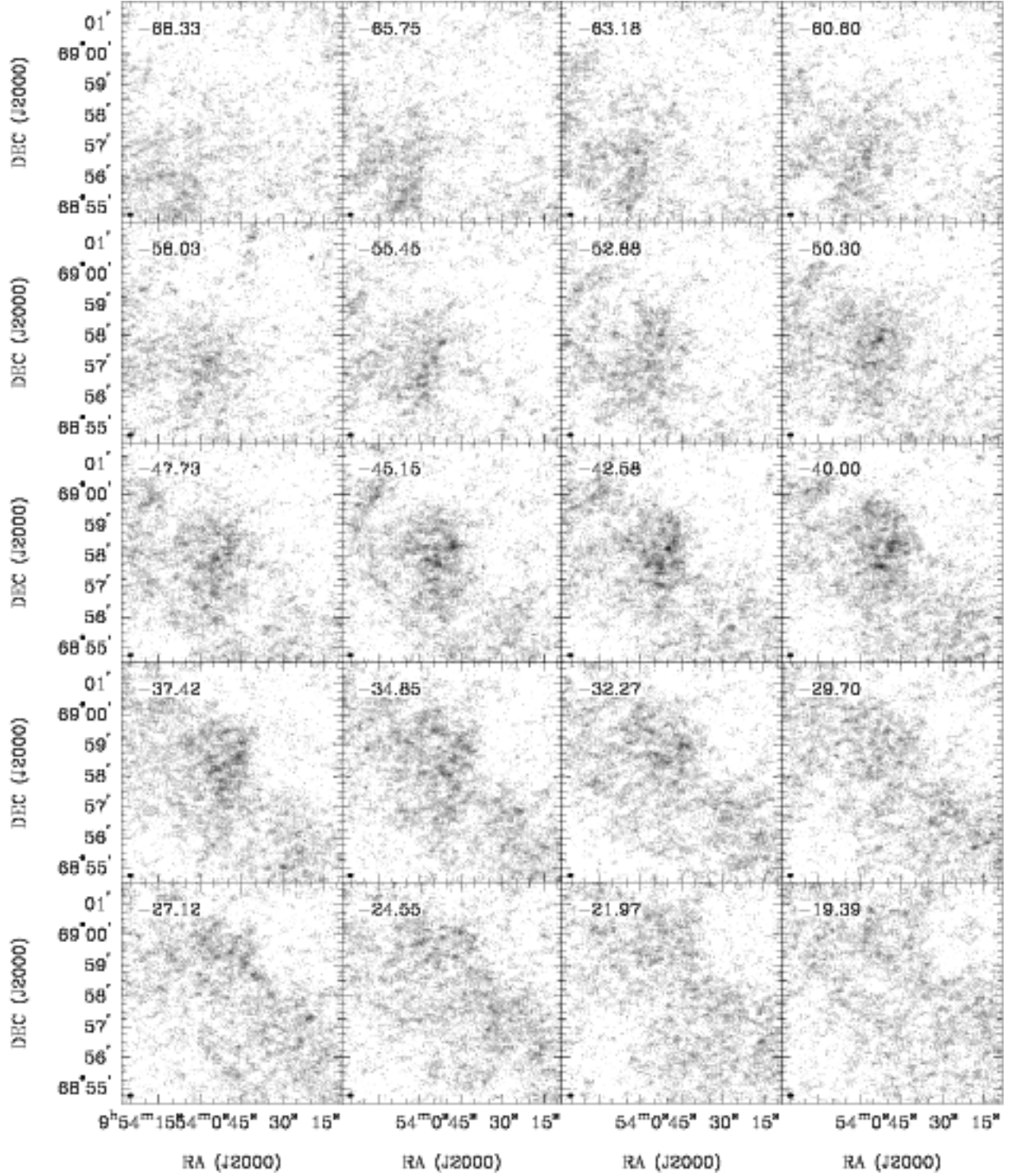


Fig. 8.— **BK3N**: Channel maps based on the natural-weighted cube (grayscale range: -0.02 to $12.9 \text{ mJy beam}^{-1}$). Every third channel is shown (channel width 0.6 km s^{-1}) and each map has the same size as the moment maps in the following panels. H I emission from M81 is present in every channel of the data cube.

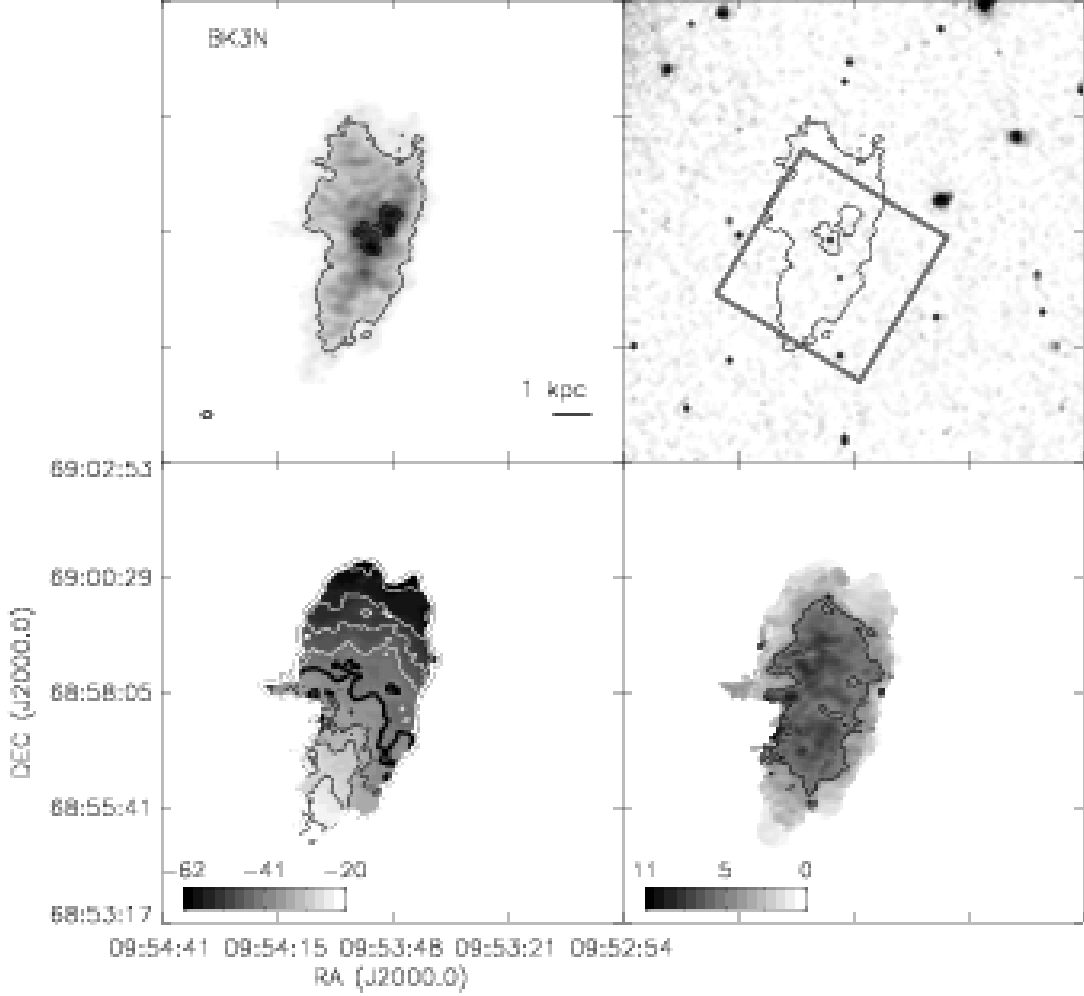


Fig. 8.— continued. *Top left:* The integrated H I intensity map for BK3N. The grayscale covers a range from 1×10^{19} to $7.1 \times 10^{20} \text{ cm}^{-2}$ with contours of 1×10^{20} and $5 \times 10^{20} \text{ cm}^{-2}$. *Top Right:* An optical g-band image from the SDSS with the same column density contours overlaid. The HST ACS footprint is the field covered by the ANGST survey. *Bottom Left:* The H I velocity field. Black contours (lighter gray scale) indicate approaching emission, white contours (darker gray scale) receding emission. The thick black contour is the central velocity ($v_{cen} = -42.5 \text{ km s}^{-1}$) and the isovelocity contours are spaced by $\Delta v = -5 \text{ km s}^{-1}$. *Bottom Right:* The H I velocity dispersion. Contours are plotted at 5 and 10 km s^{-1} . Colorbars are in units of km s^{-1} .

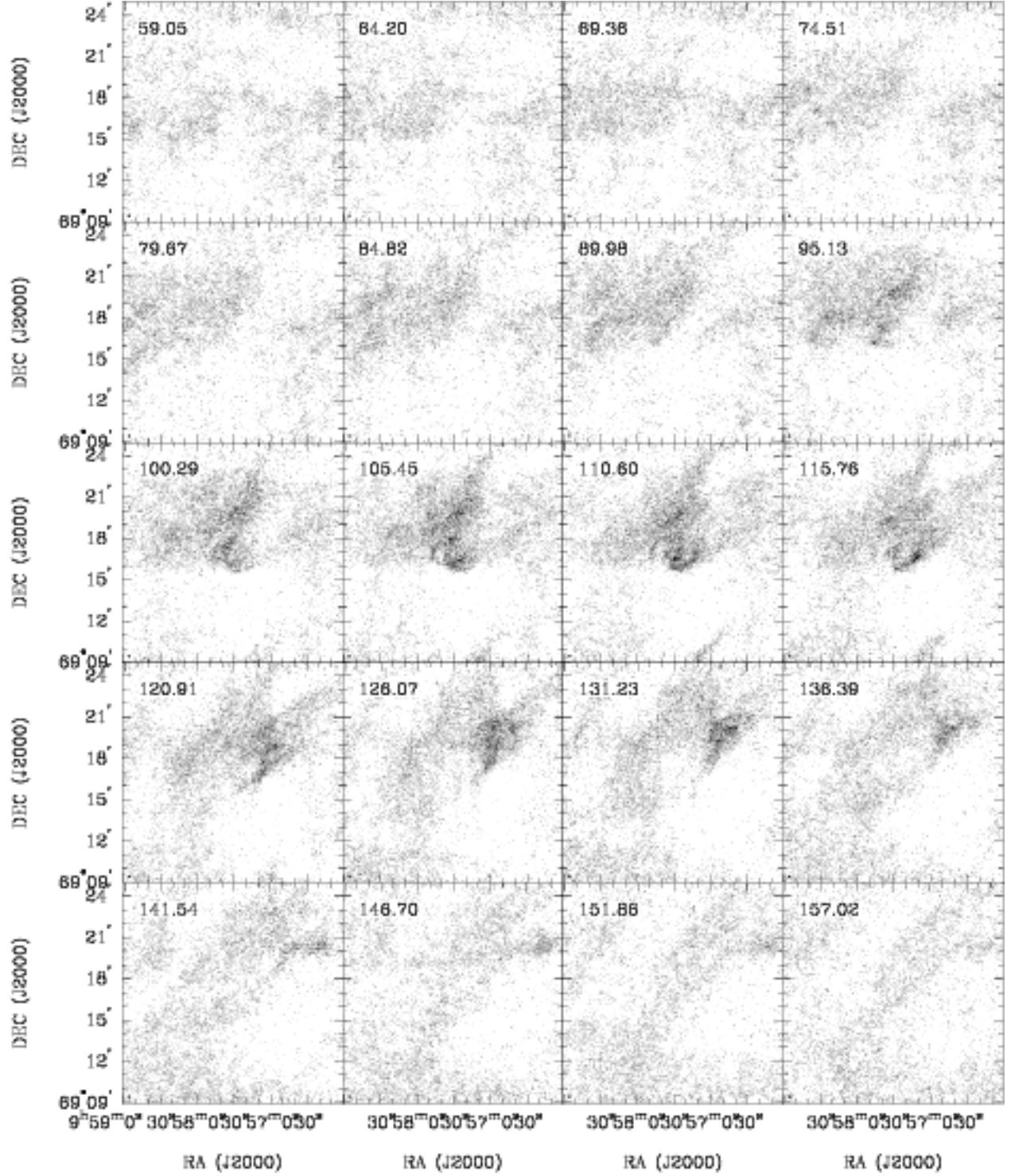


Fig. 9.— **AO 0952+69**: Channel maps based on the natural-weighted cube (grayscale range: -0.02 to $10.5 \text{ mJy beam}^{-1}$). Every third channel is shown (channel width 1.3 km s^{-1}) and each map has the same size as the moment maps in the following panels. This field is in the M81 group and therefore tidal H I from member interactions is also visible.

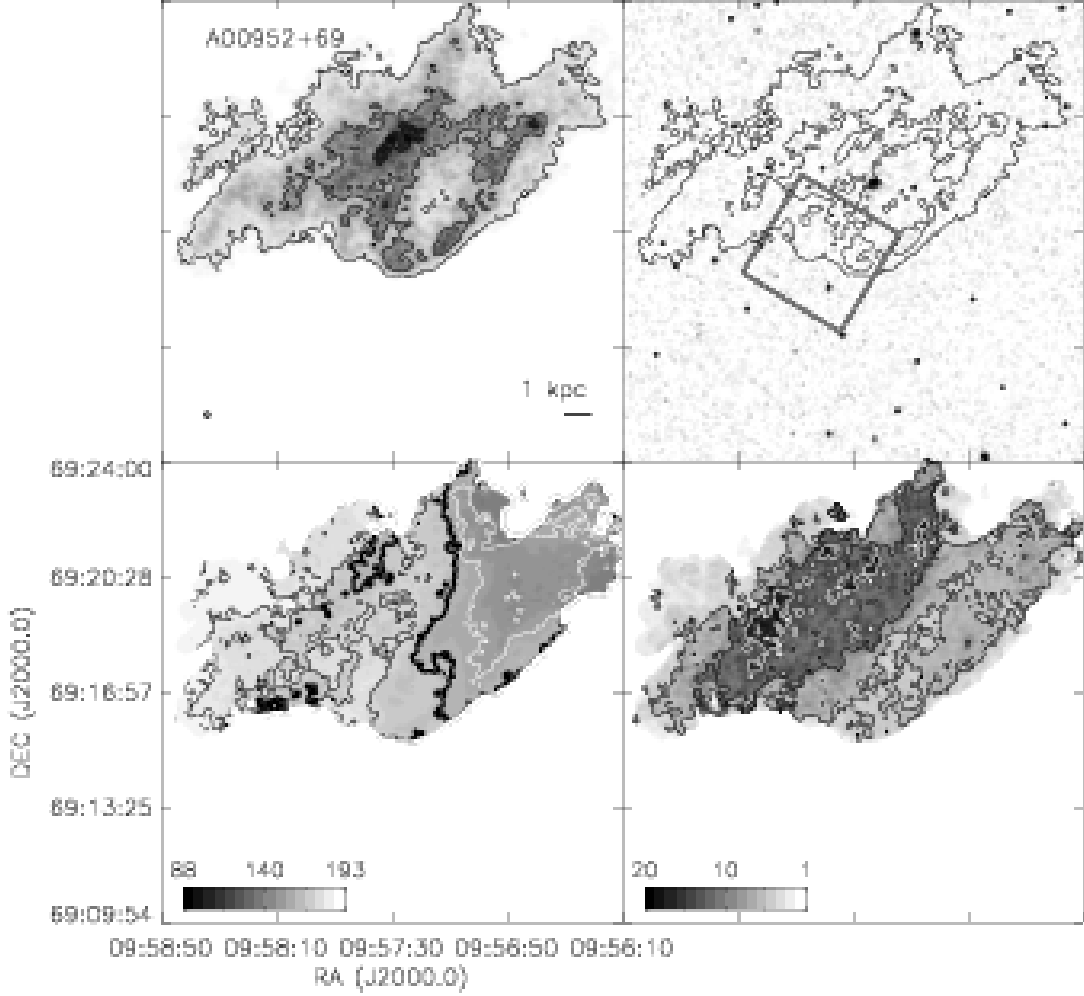


Fig. 9.— continued. *Top left:* The integrated H I intensity map for AO 0952+69. The grayscale covers a range from 1×10^{19} to $1.13 \times 10^{21} \text{ cm}^{-2}$ with contours of 1×10^{20} , 5×10^{20} , and $1 \times 10^{21} \text{ cm}^{-2}$. *Top Right:* An optical g-band image from the SDSS with the same column density contours overlaid. The HST ACS footprint is the field covered by the ANGST survey. *Bottom Left:* The H I velocity field. Black contours (lighter gray scale) indicate approaching emission, white contours (darker gray scale) receding emission. The thick black contour is the central velocity ($v_{\text{cen}} = 112.8 \text{ km s}^{-1}$) and the isovelocity contours are spaced by $\Delta v = 10 \text{ km s}^{-1}$. *Bottom Right:* The H I velocity dispersion. Contours are plotted at 5, 10, and 15 km s^{-1} . Colorbars are in units of km s^{-1} .

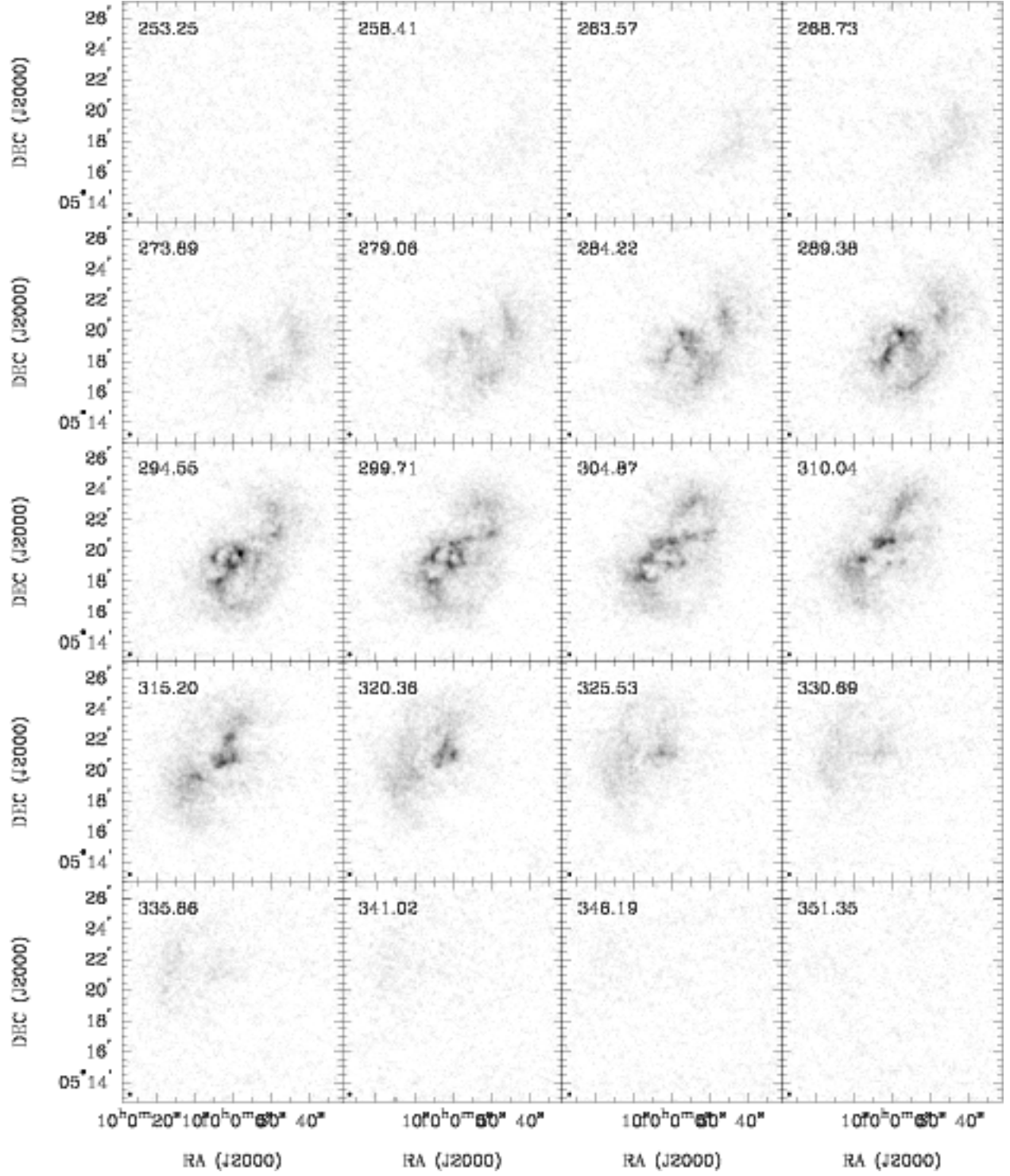


Fig. 10.— **Sextans B**: Channel maps based on the natural-weighted cube (grayscale range: -0.02 to $25.3 \text{ mJy beam}^{-1}$). Every third channel is shown (channel width 1.3 km s^{-1}) and each map has the same size as the moment maps in the following panels.

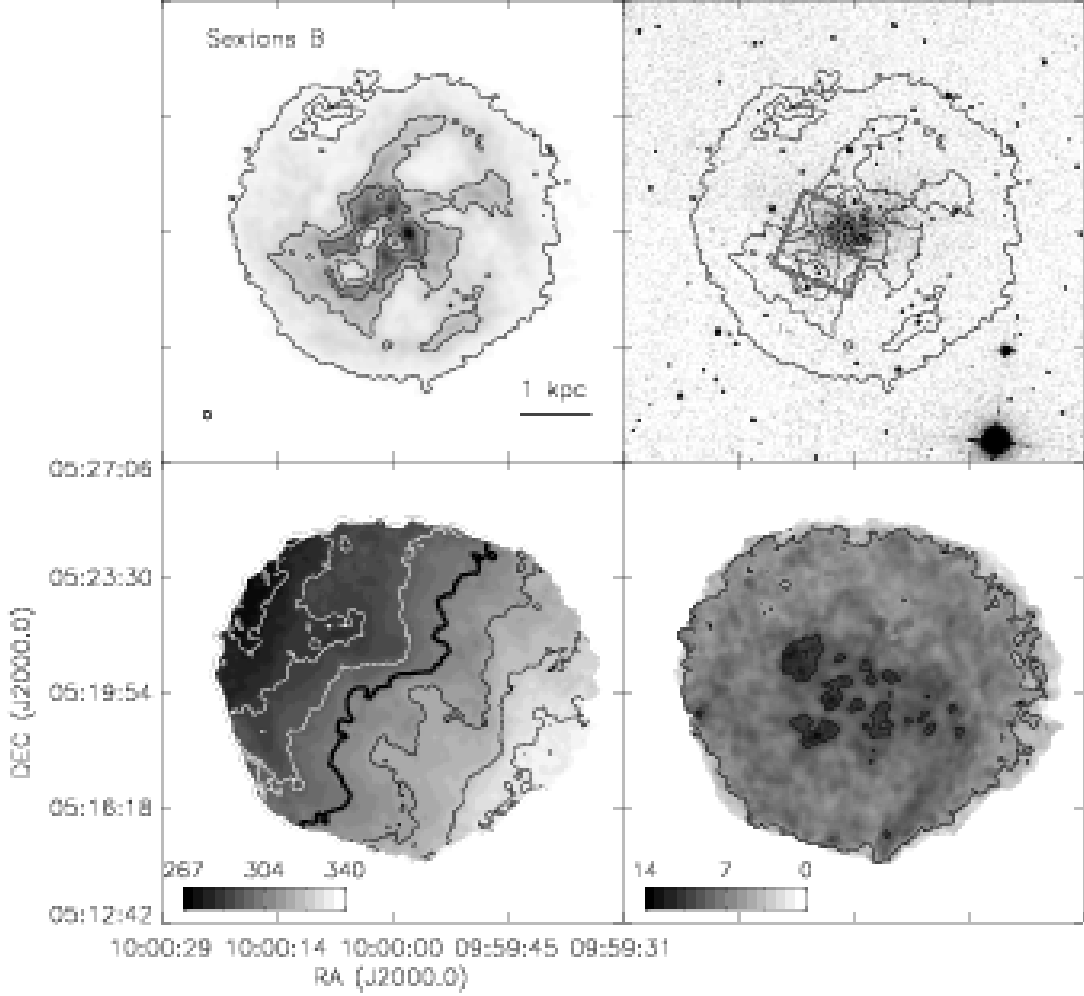


Fig. 10.— continued. *Top left:* The integrated H I intensity map for Sextans B. The grayscale covers a range from 1×10^{19} to $2.6 \times 10^{21} \text{ cm}^{-2}$ with contours of 1×10^{20} , 5×10^{20} , and $1 \times 10^{21} \text{ cm}^{-2}$. *Top Right:* An optical g-band image from the SDSS with the same column density contours overlaid. The HST WFPC2 footprint is the field covered by the ANGST survey. *Bottom Left:* The H I velocity field. Black contours (lighter gray scale) indicate approaching emission, white contours (darker gray scale) receding emission. The thick black contour is the central velocity ($v_{cen} = 302.2 \text{ km s}^{-1}$) and the isovelocity contours are spaced by $\Delta v = 10 \text{ km s}^{-1}$. *Bottom Right:* The H I velocity dispersion. Contours are plotted at 5 and 10 km s^{-1} . Colorbars are in units of km s^{-1} .

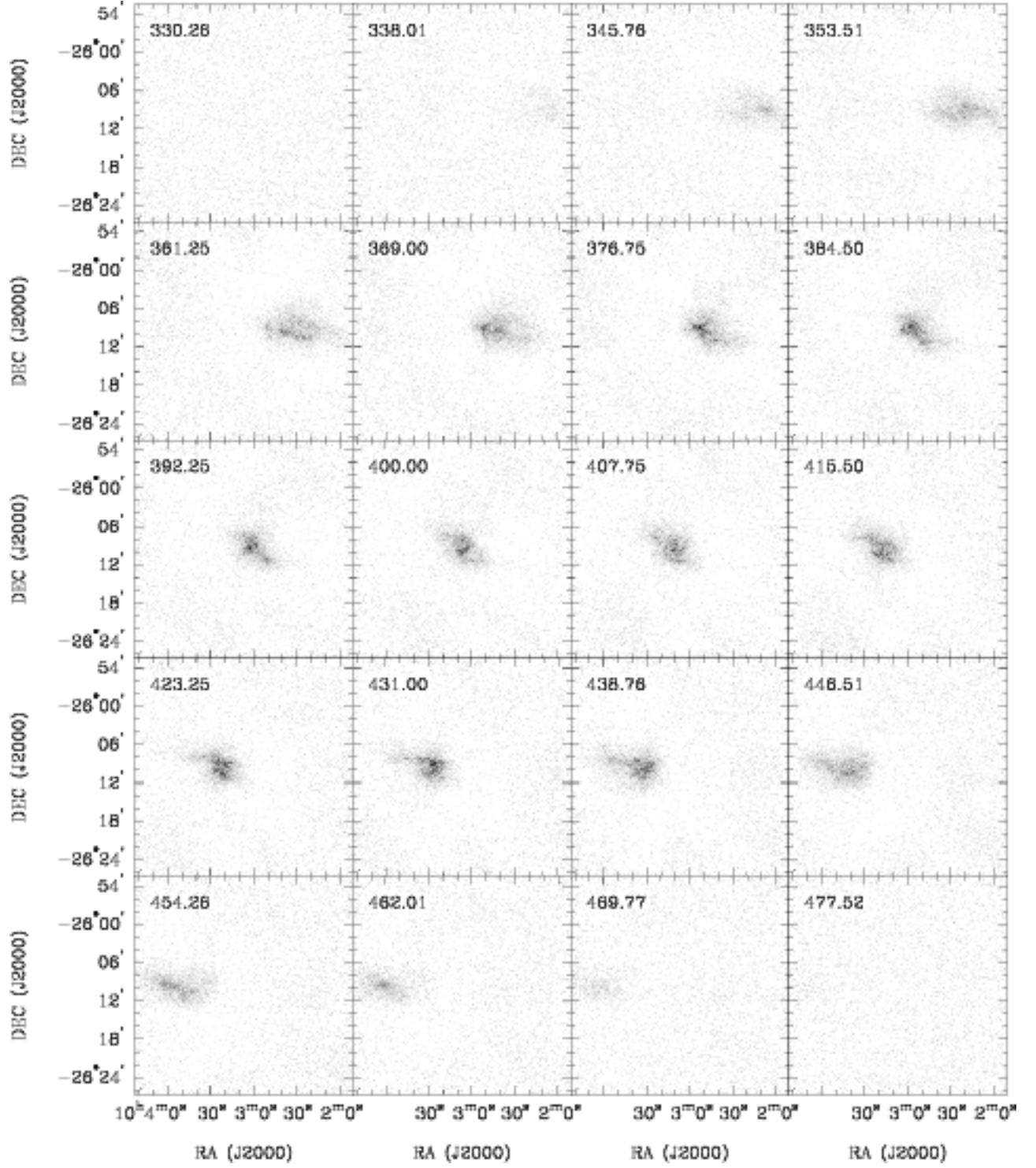


Fig. 11.— **NGC 3109**: Channel maps based on the natural-weighted cube (grayscale range: -0.02 to $31.7 \text{ mJy beam}^{-1}$). Every fifth channel is shown (channel width 1.3 km s^{-1}) and each map has the same size as the moment maps in the following panels.

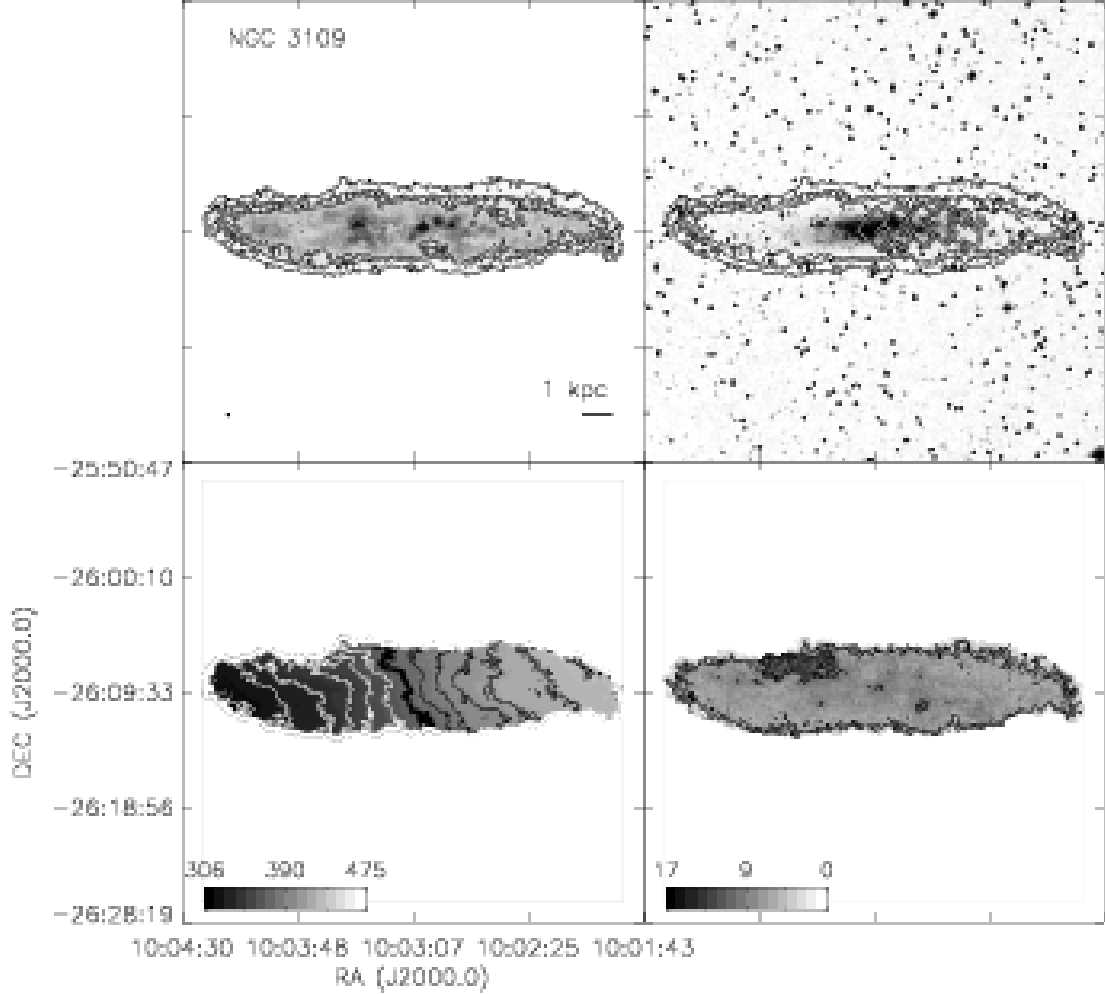


Fig. 11.— continued. *Top left:* The integrated H I intensity map for NGC 3109. The grayscale covers a range from 1×10^{19} to $6.6 \times 10^{21} \text{ cm}^{-2}$ with contours of 1×10^{20} , 5×10^{20} , 1×10^{21} , and $5 \times 10^{21} \text{ cm}^{-2}$. *Top Right:* An optical 4680 Å image from the DSS with the same column density contours overlaid. The HST WFPC2 footprints are the fields covered by the ANGST survey. *Bottom Left:* The H I velocity field. Black contours (lighter grayscale) indicate approaching emission, white contours (darker grayscale) receding emission. The thick black contour is the central velocity ($v_{\text{cen}} = 405.1 \text{ km s}^{-1}$) and the isovelocity contours are spaced by $\Delta v = 10 \text{ km s}^{-1}$. *Bottom Right:* The H I velocity dispersion. Contours are plotted at 5, 10, and 15 km s^{-1} . Colorbars are in units of km s^{-1} .

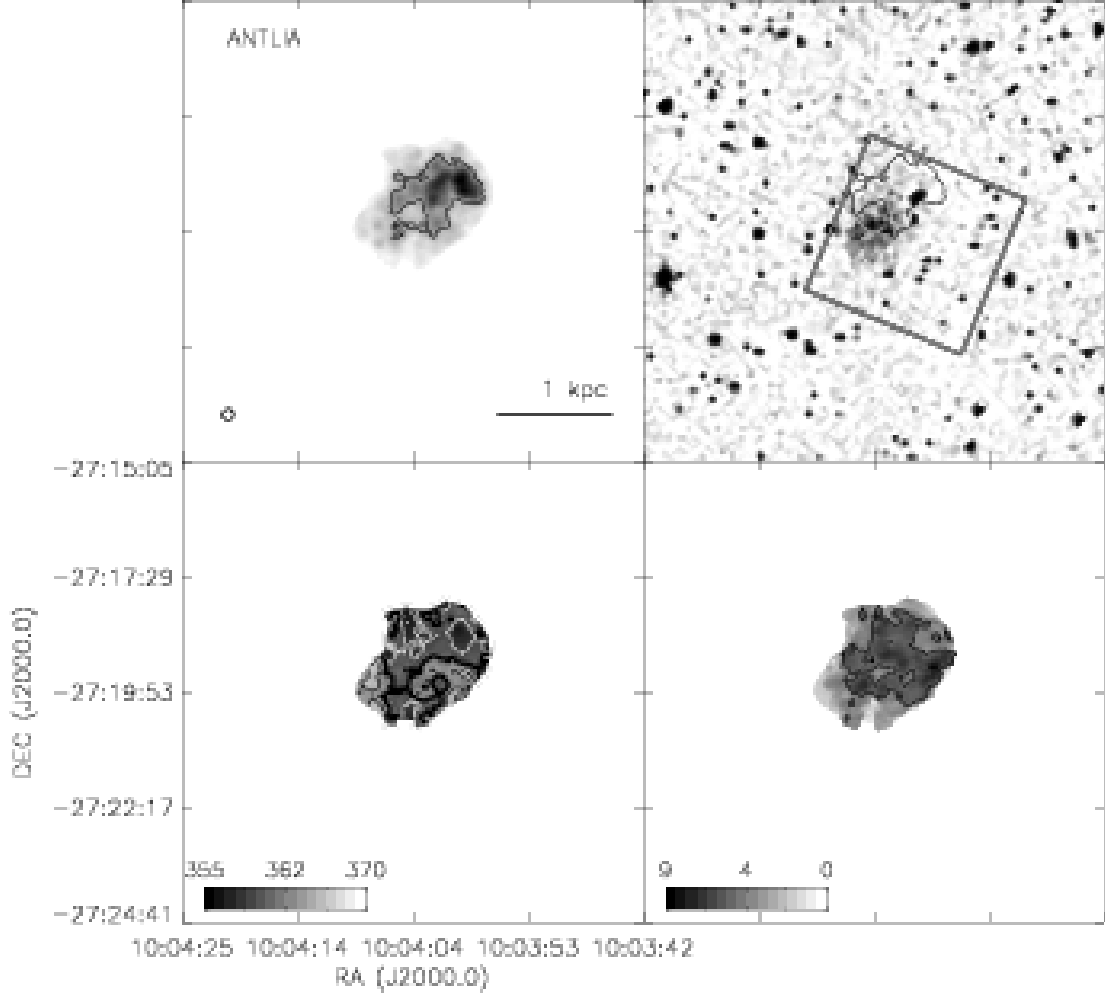


Fig. 12.— continued. *Top left:* The integrated H I intensity map for Antlia. The grayscale covers a range from 1×10^{19} to $2.9 \times 10^{20} \text{ cm}^{-2}$ with a contour of $1 \times 10^{20} \text{ cm}^{-2}$. *Top Right:* An optical 4680 Å image from the DSS with the same column density contours overlaid. The HST ACS footprint is the field covered by the ANGST survey. *Bottom Left:* The H I velocity field. Black contours (lighter grayscale) indicate approaching emission, white contours (darker grayscale) receding emission. The thick black contour is the central velocity ($v_{cen} = 363.0 \text{ km s}^{-1}$) and the isovelocity contours are spaced by $\Delta v = 3 \text{ km s}^{-1}$. *Bottom Right:* The H I velocity dispersion. A contour is plotted at 5 km s^{-1} . Colorbars are in units of km s^{-1} .

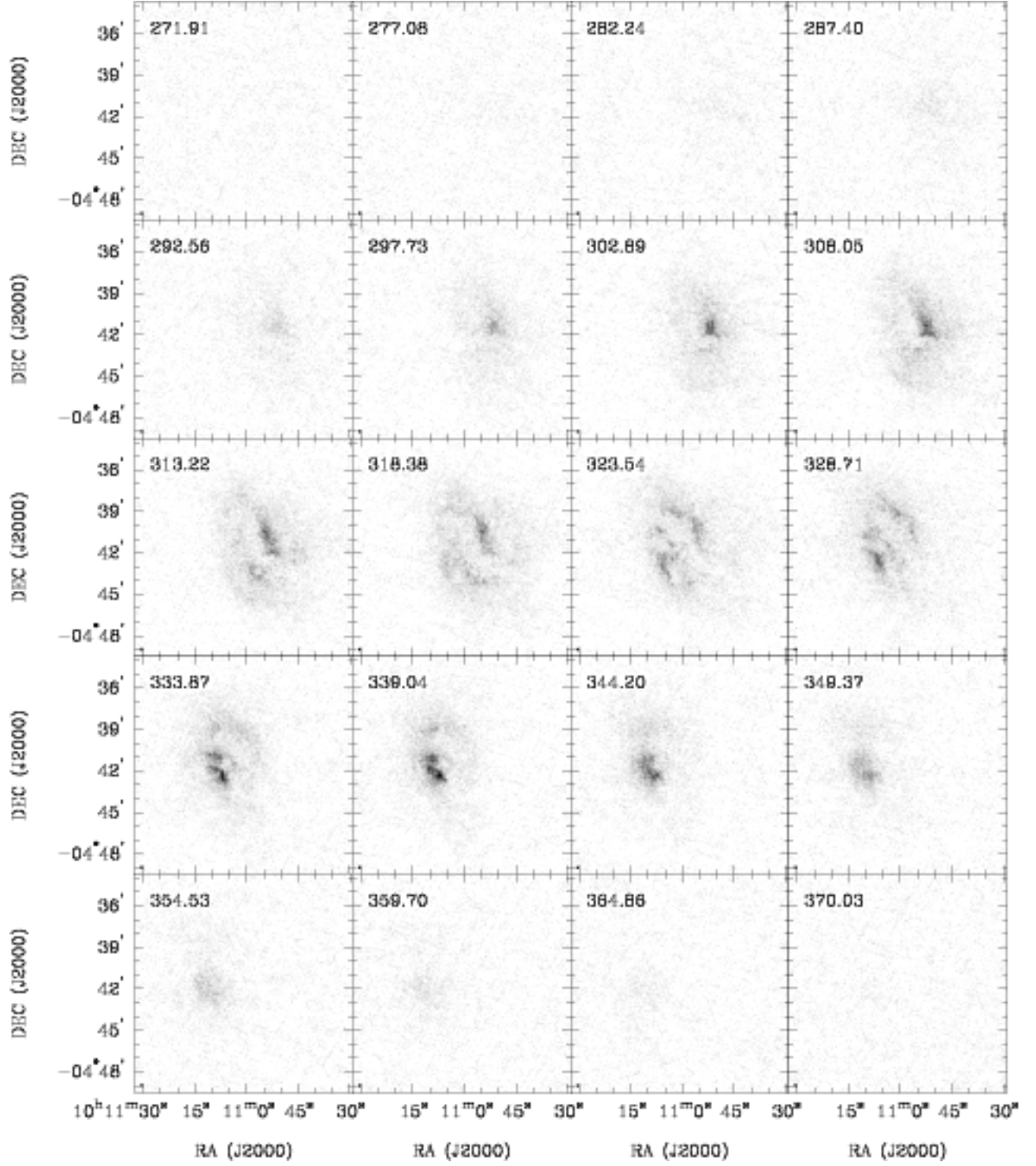


Fig. 13.— **Sextans A:** Channel maps based on the natural-weighted cube (grayscale range: -0.02 to $35.4 \text{ mJy beam}^{-1}$). Every third channel is shown (channel width 1.3 km s^{-1}) and each map has the same size as the moment maps in the following panels.

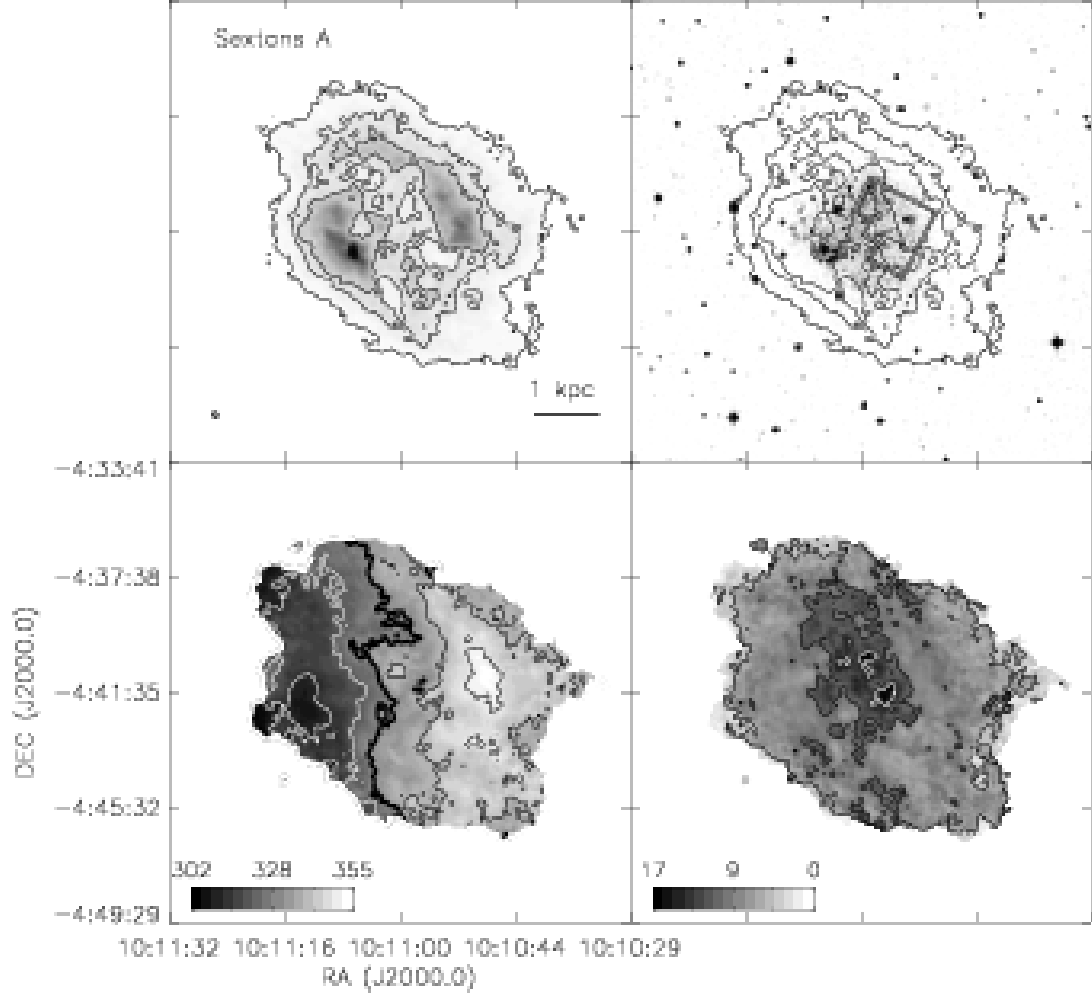


Fig. 13.— continued. *Top left:* The integrated H I intensity map for Sextans A. The grayscale covers a range from 1×10^{19} to $6.1 \times 10^{21} \text{ cm}^{-2}$ with contours of 1×10^{20} , 5×10^{20} , 1×10^{21} , and $5 \times 10^{21} \text{ cm}^{-2}$. *Top Right:* An optical 4680 Å image from the DSS with the same column density contours overlaid. The HST WFPC2 footprint is the field covered by the ANGST survey. *Bottom Left:* The H I velocity field. Black contours (lighter gray scale) indicate approaching emission, white contours (darker gray scale) receding emission. The thick black contour is the central velocity ($v_{cen} = 324.8 \text{ km s}^{-1}$) and the isovelocity contours are spaced by $\Delta v = 10 \text{ km s}^{-1}$. *Bottom Right:* The H I velocity dispersion. Contours are plotted at 5, 10, and 15 km s^{-1} . Colorbars are in units of km s^{-1} .

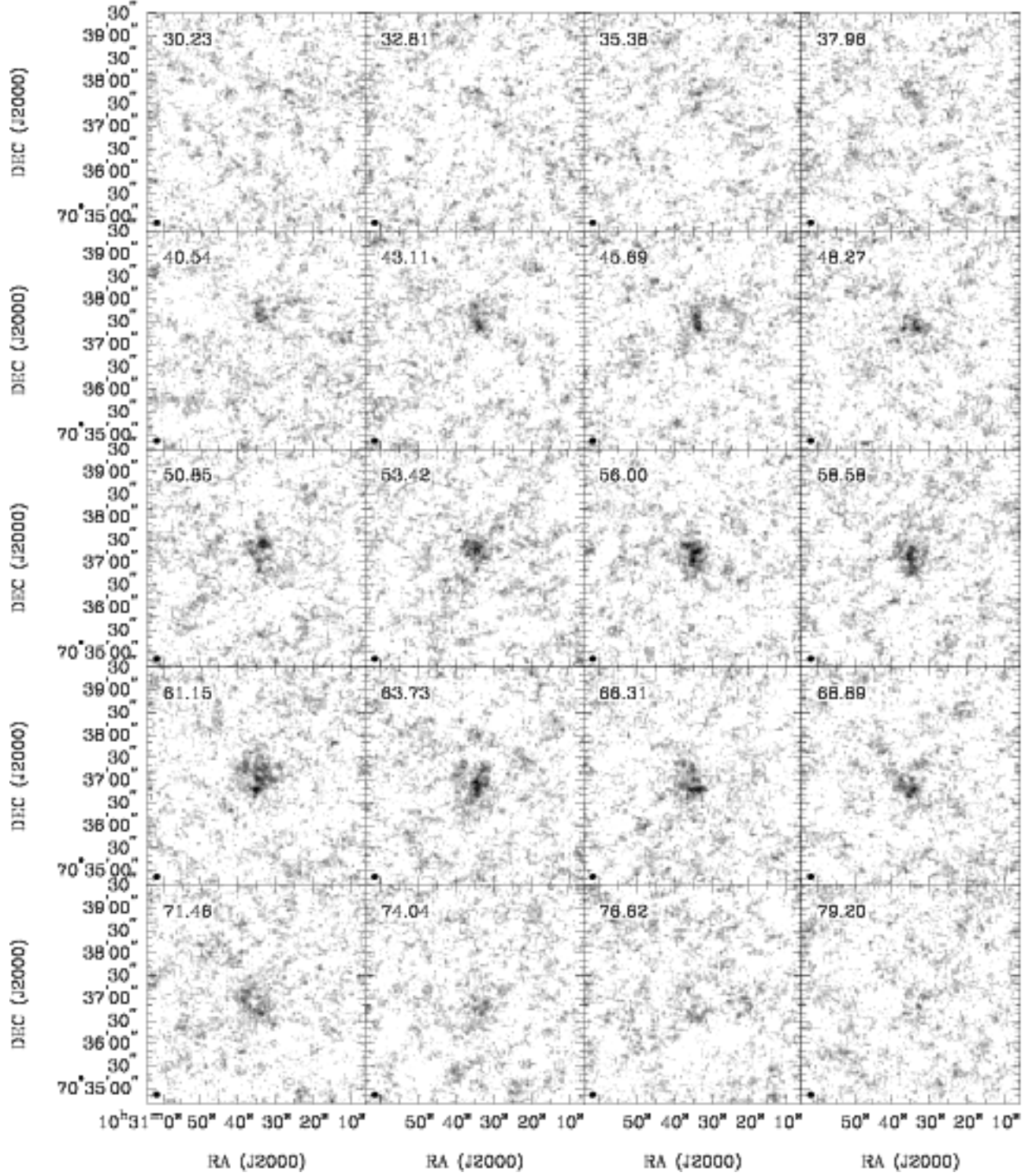


Fig. 14.— **DDO 82**: Channel maps based on the natural-weighted cube (grayscale range: -0.02 to $6.7 \text{ mJy beam}^{-1}$). Every channel is shown (channel width 1.3 km s^{-1}) and each map has the same size as the moment maps in the following panels.

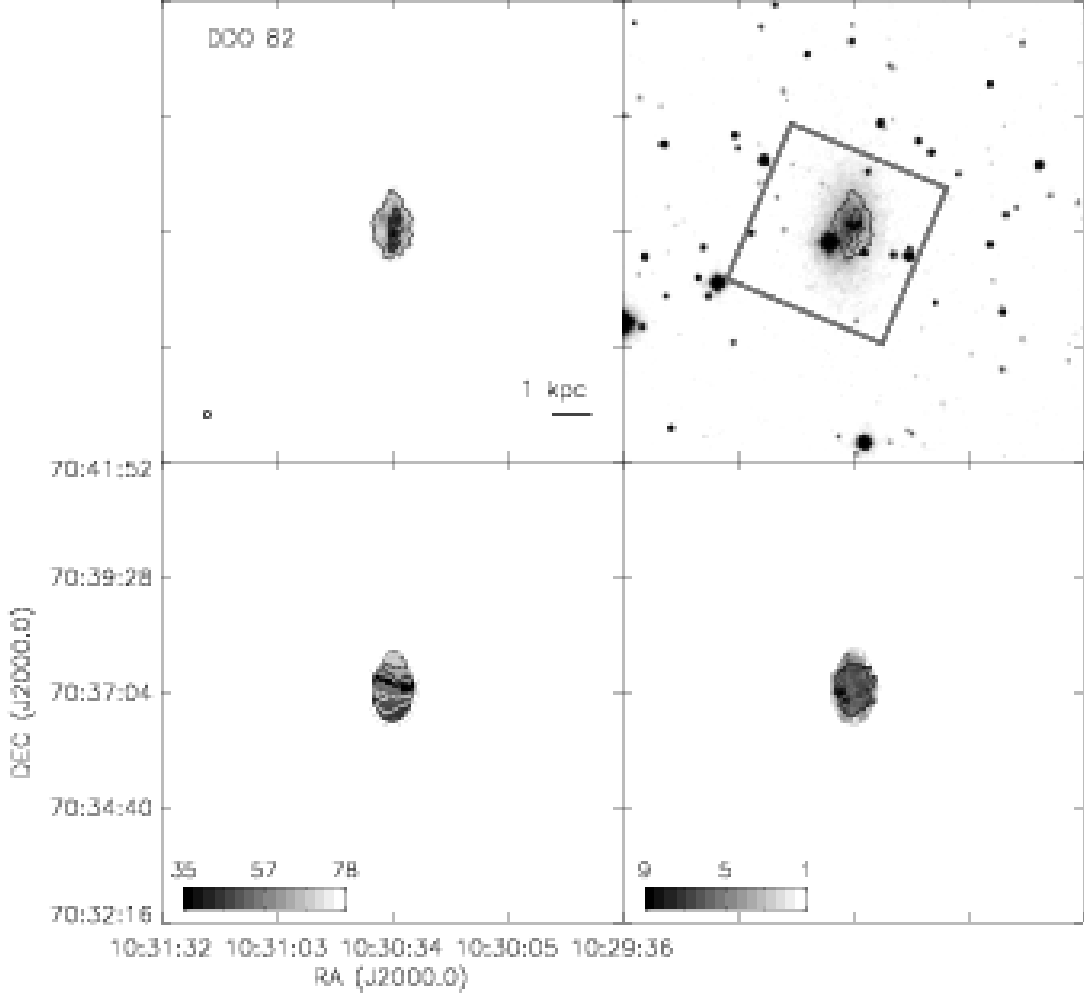


Fig. 14.— continued. *Top left:* The integrated H I intensity map for DDO 82. The grayscale covers a range from 1×10^{19} to $9.3 \times 10^{20} \text{ cm}^{-2}$ with contours of 1×10^{20} and $5 \times 10^{20} \text{ cm}^{-2}$. *Top Right:* An optical 6450 Å image from the DSS with the same column density contours overlaid. The HST ACS footprint is the field covered by the ANGST survey. *Bottom Left:* The H I velocity field. Black contours (lighter gray scale) indicate approaching emission, white contours (darker gray scale) receding emission. The thick black contour is the central velocity ($v_{\text{cen}} = 56.2 \text{ km s}^{-1}$) and the isovelocity contours are spaced by $\Delta v = 5 \text{ km s}^{-1}$. *Bottom Right:* The H I velocity dispersion. A contour is plotted at 5 km s^{-1} . Colorbars are in units of km s^{-1} .

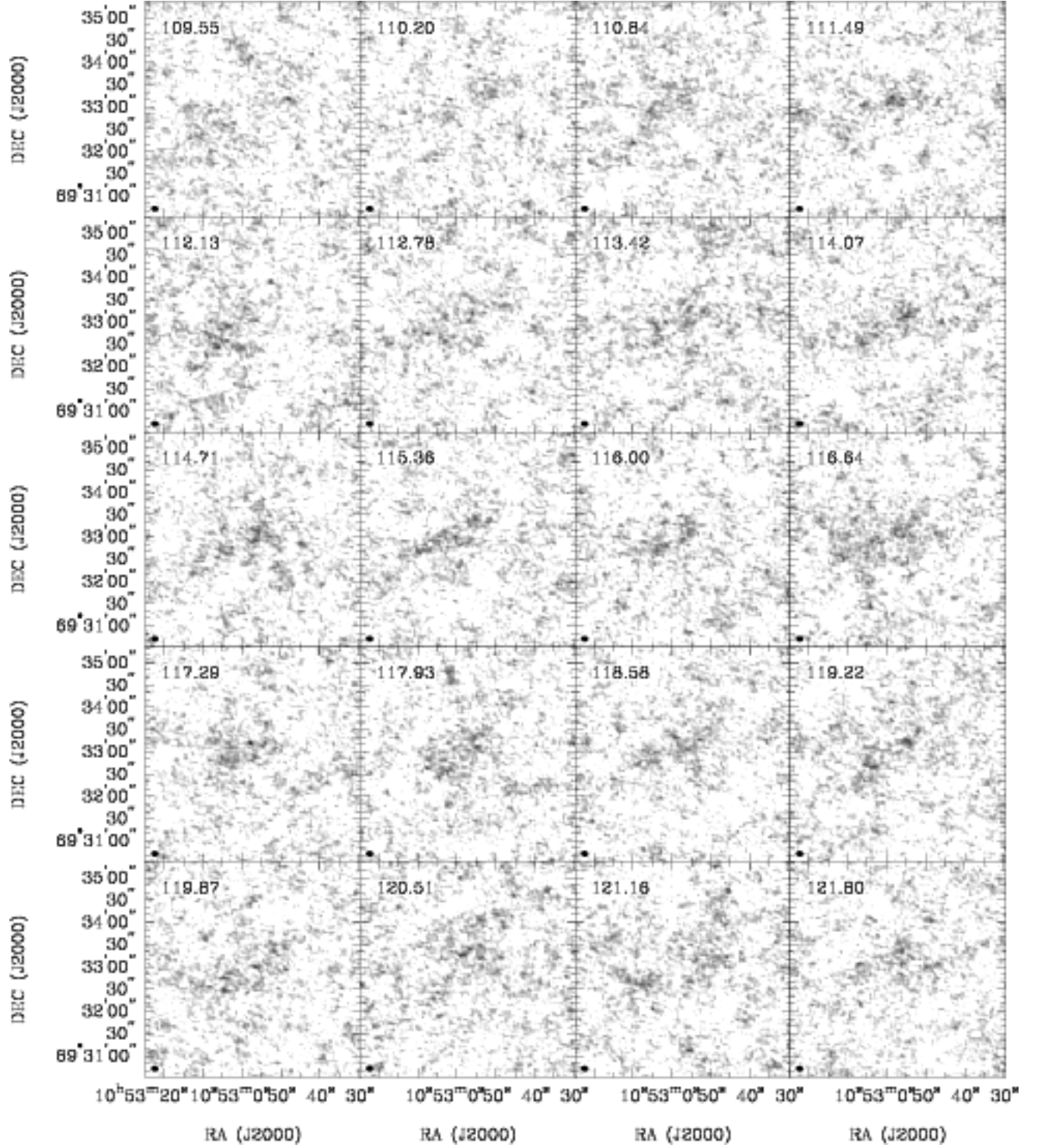


Fig. 15.— **KDG 73**: Channel maps based on the natural-weighted cube (grayscale range: -0.02 to $8.6 \text{ mJy beam}^{-1}$). Every third channel is shown (channel width 0.6 km s^{-1}) and each map has the same size as the moment maps in the following panels.

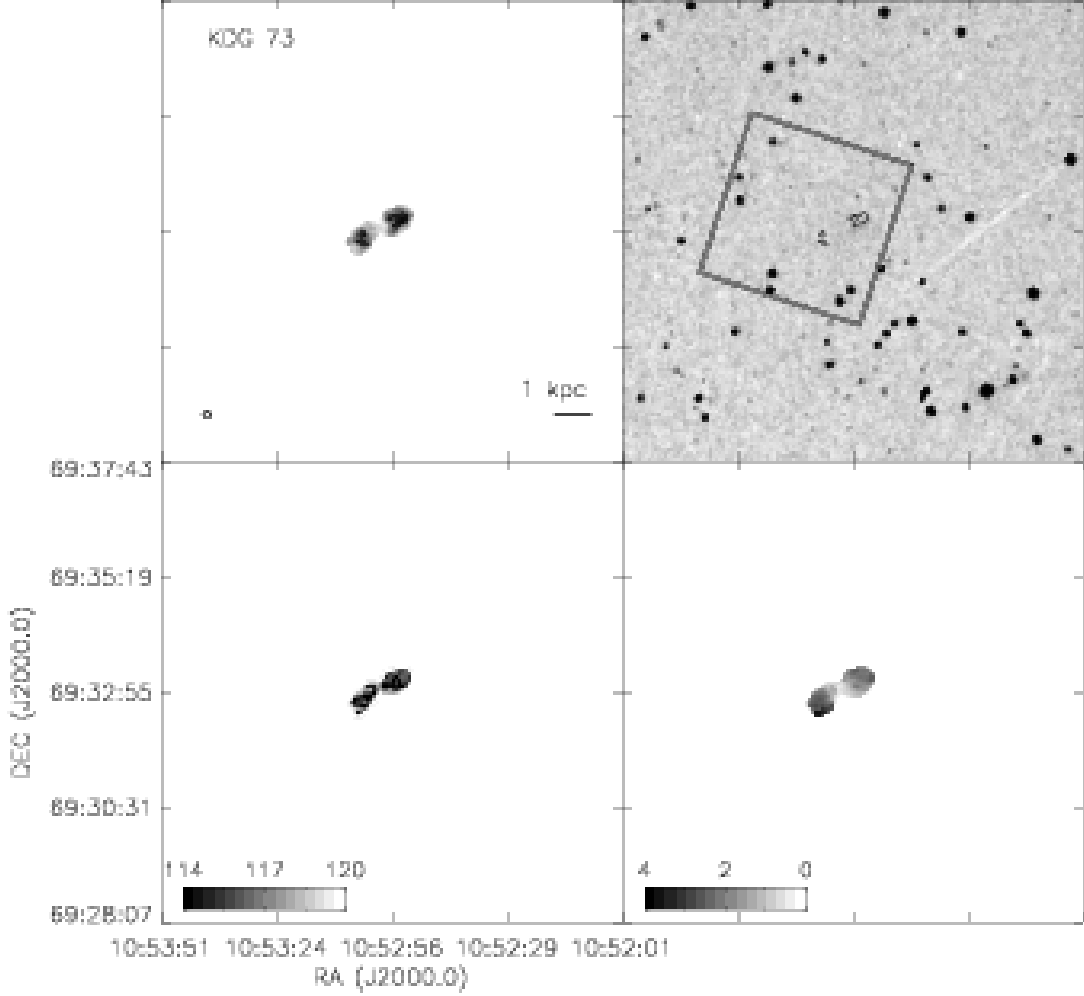


Fig. 15.— continued. *Top left:* The integrated H I intensity map for KDG 73. The grayscale covers a range from 1×10^{19} to $1.4 \times 10^{20} \text{ cm}^{-2}$ with a contour of $1 \times 10^{20} \text{ cm}^{-2}$. *Top Right:* An optical 6450 Å image from the DSS with the same column density contours overlaid. The HST ACS footprint is the field covered by the ANGST survey. *Bottom Left:* The H I velocity field. Black contours (lighter gray scale) indicate approaching emission, white contours (darker gray scale) receding emission. The thick black contour is the central velocity ($v_{\text{cen}} = 116.3 \text{ km s}^{-1}$) and the isovelocity contours are spaced by $\Delta v = 10 \text{ km s}^{-1}$. *Bottom Right:* The H I velocity dispersion. Colorbars are in units of km s^{-1} .

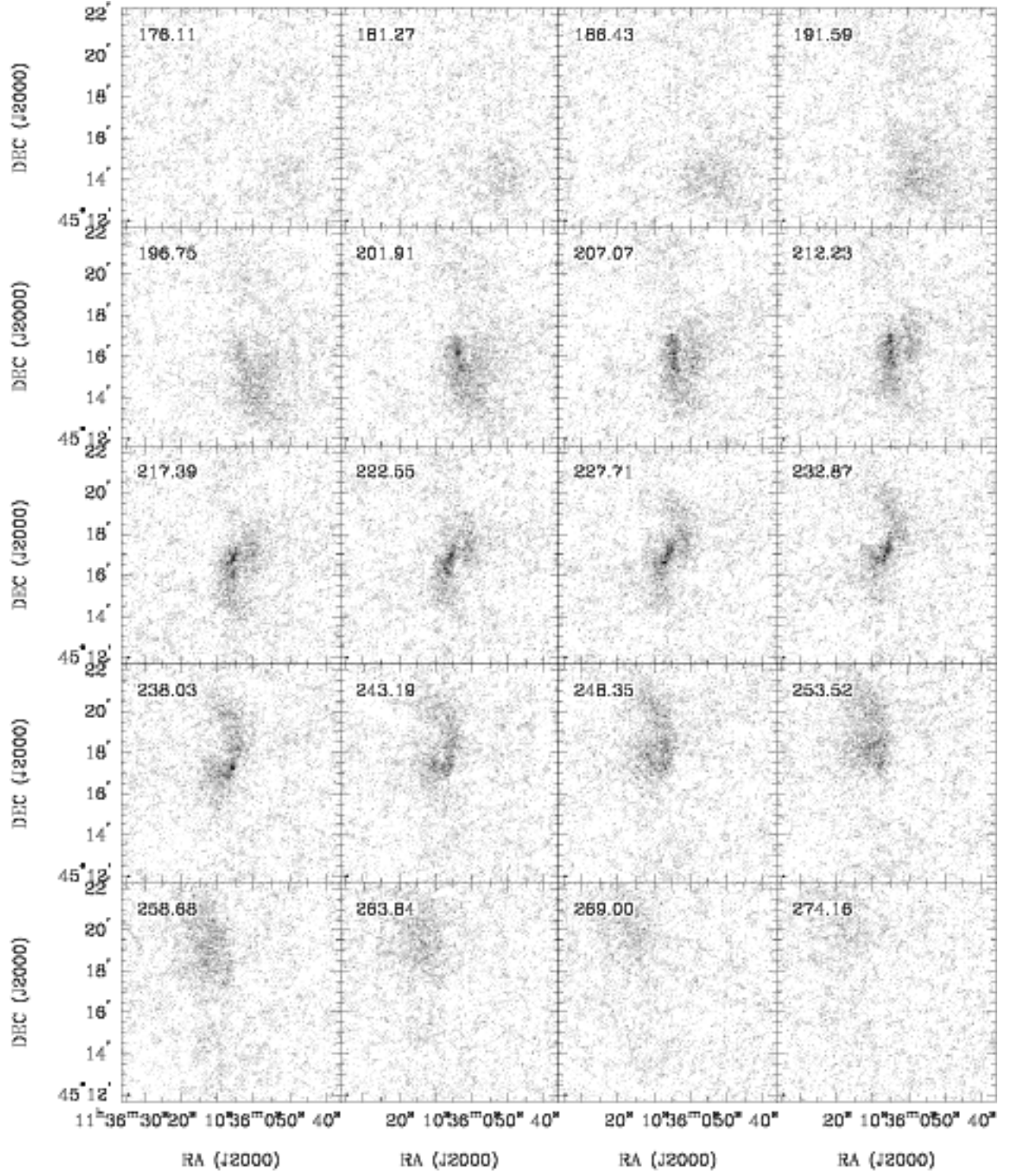


Fig. 16.— **NGC 3741**: Channel maps based on the natural-weighted cube (grayscale range: -0.02 to $9.6 \text{ mJy beam}^{-1}$). Every third channel is shown (channel width 1.3 km s^{-1}) and each map has the same size as the moment maps in the following panels.

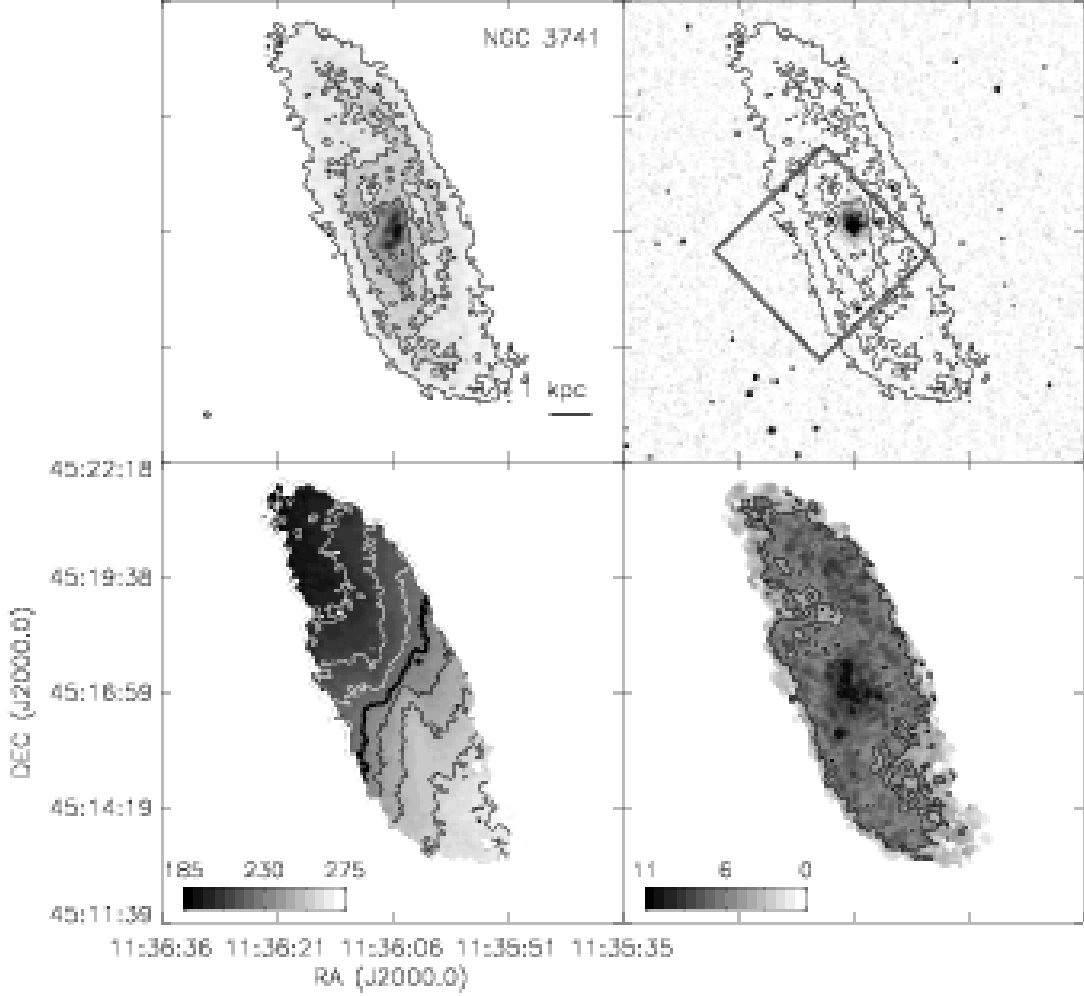


Fig. 16.— continued. *Top left:* The integrated H I intensity map for NGC 3741. The grayscale covers a range from 1×10^{19} to $3.4 \times 10^{21} \text{ cm}^{-2}$ with contours of 1×10^{20} , 5×10^{20} , and $1 \times 10^{21} \text{ cm}^{-2}$. *Top Right:* An optical g-band image from the SDSS with the same column density contours overlaid. The HST ACS footprint is the field covered by the ANGST survey. *Bottom Left:* The H I velocity field. Black contours (lighter gray scale) indicate approaching emission, white contours (darker gray scale) receding emission. The thick black contour is the central velocity ($v_{cen} = 229.1 \text{ km s}^{-1}$) and the isovelocity contours are spaced by $\Delta v = 10 \text{ km s}^{-1}$. *Bottom Right:* The H I velocity dispersion. Contours are plotted at 5 and 10 km s^{-1} . Colorbars are in units of km s^{-1} .

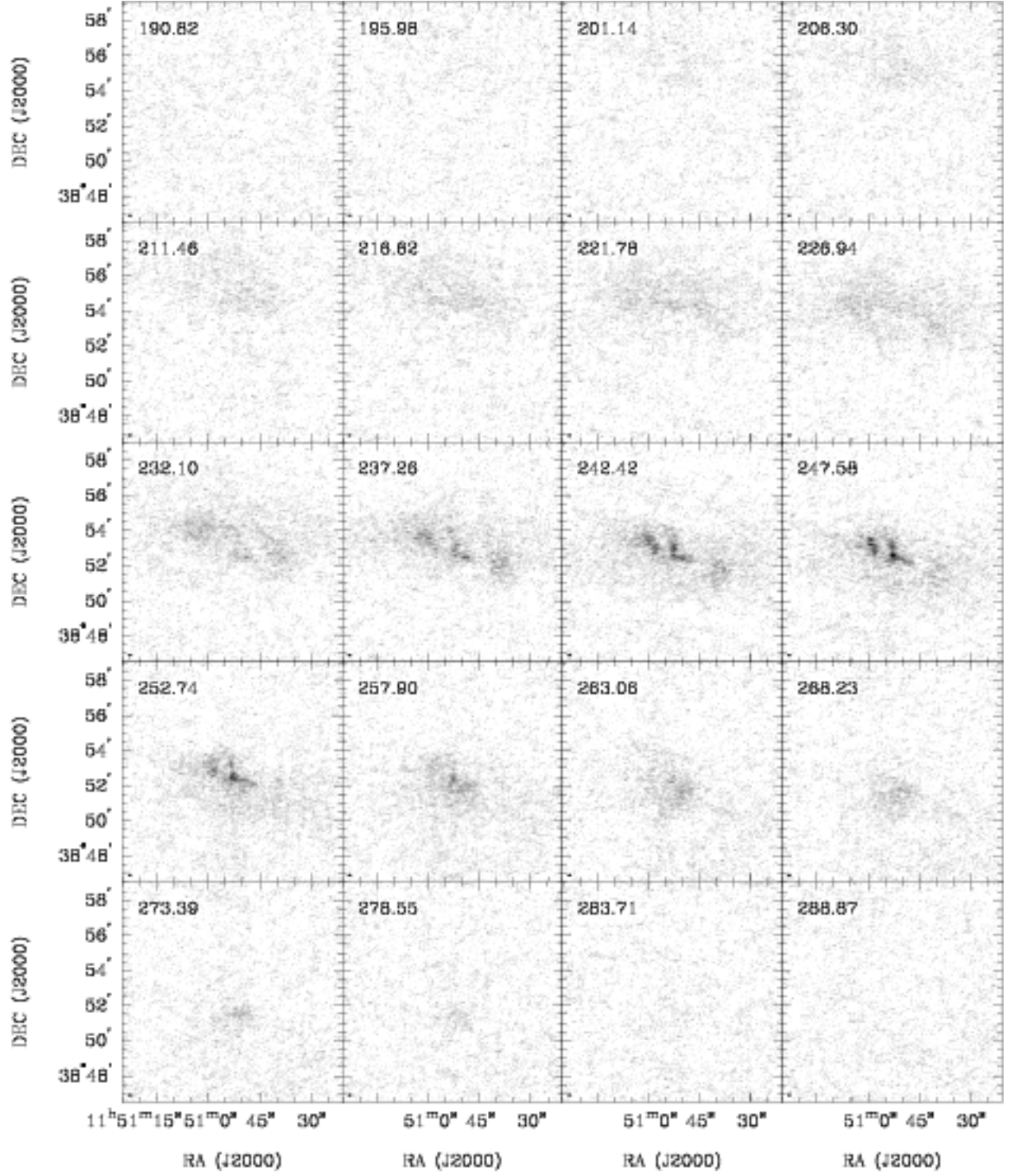


Fig. 17.— **DDO 99**: Channel maps based on the natural-weighted cube (grayscale range: -0.02 to $14.7 \text{ mJy beam}^{-1}$). Every third channel is shown (channel width 1.3 km s^{-1}) and each map has the same size as the moment maps in the following panels.

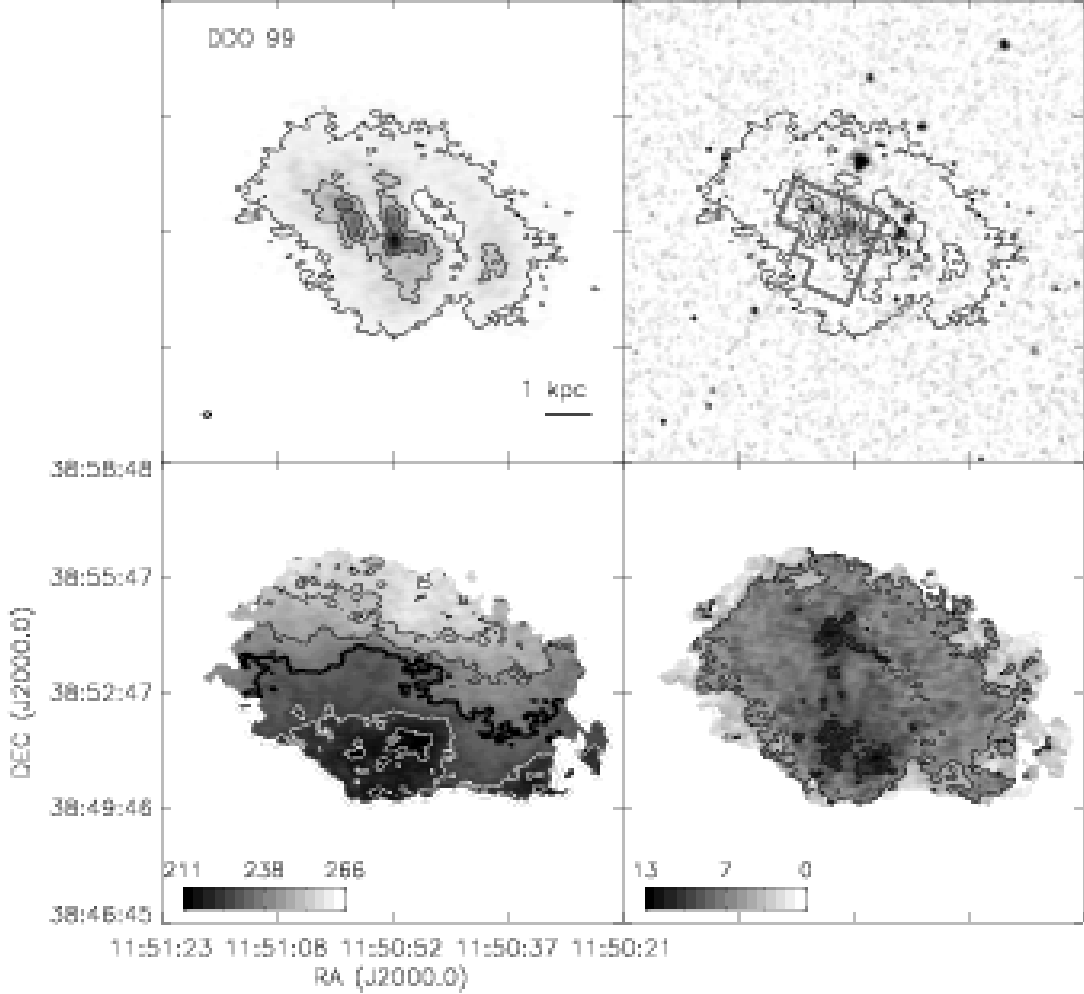


Fig. 17.— continued. *Top left:* The integrated H I intensity map for DDO 99. The grayscale covers a range from 1×10^{19} to $2.6 \times 10^{21} \text{ cm}^{-2}$ with contours of 1×10^{20} , 5×10^{20} , and $1 \times 10^{21} \text{ cm}^{-2}$. *Top Right:* An optical g-band image from the SDSS with the same column density contours overlaid. The HST WFPC2 footprint is the field covered by the ANGST survey. *Bottom Left:* The H I velocity field. Black contours (lighter gray scale) indicate approaching emission, white contours (darker gray scale) receding emission. The thick black contour is the central velocity ($v_{cen} = 242.1 \text{ km s}^{-1}$) and the isovelocity contours are spaced by $\Delta v = 10 \text{ km s}^{-1}$. *Bottom Right:* The H I velocity dispersion. Contours are plotted at 5 and 10 km s^{-1} . Colorbars are in units of km s^{-1} .

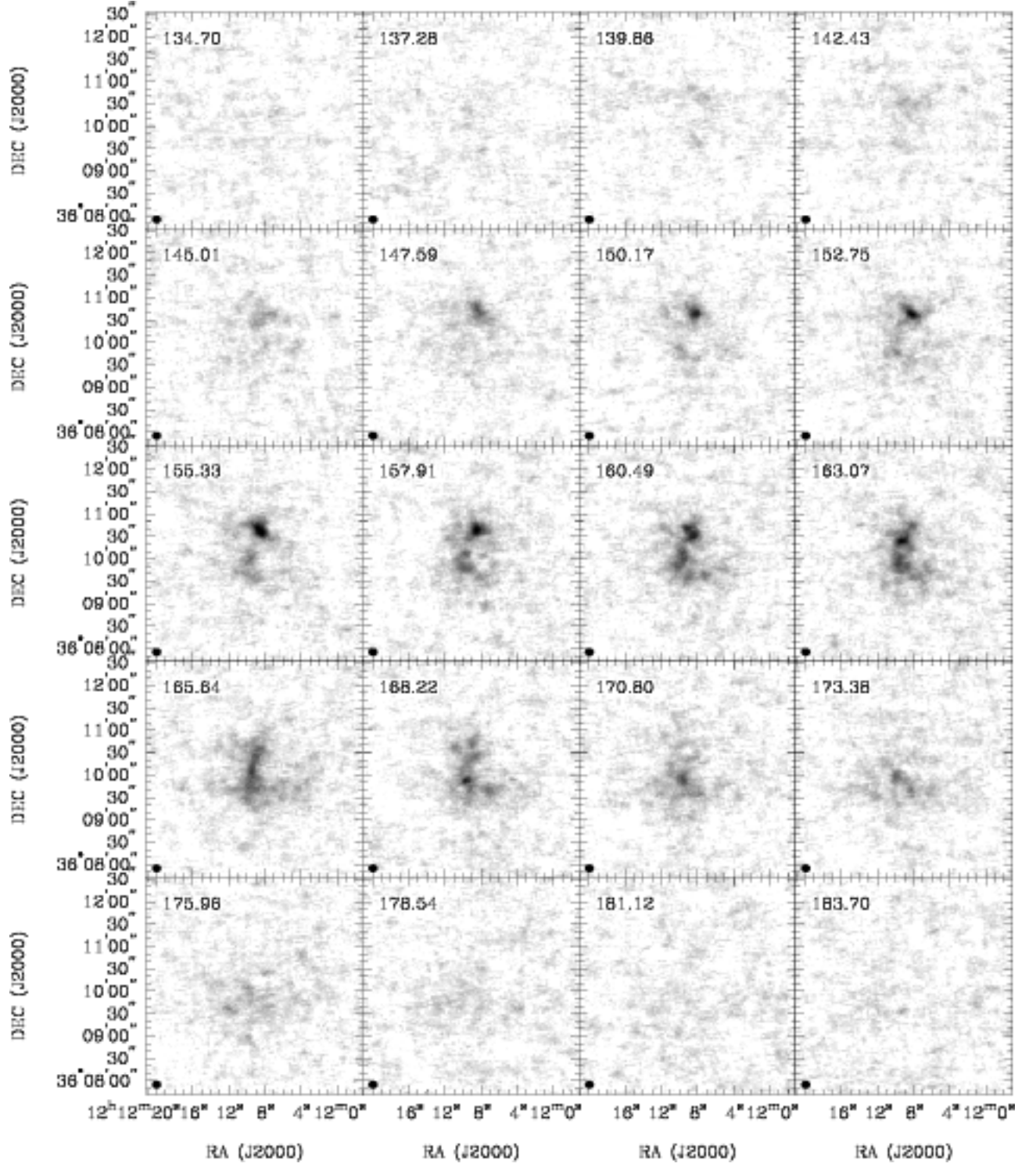


Fig. 18.— **NGC 4163**: Channel maps based on the natural-weighted cube (grayscale range: -0.02 to $16.1 \text{ mJy beam}^{-1}$). Every third channel is shown (channel width 0.6 km s^{-1}) and each map has the same size as the moment maps in the following panels.

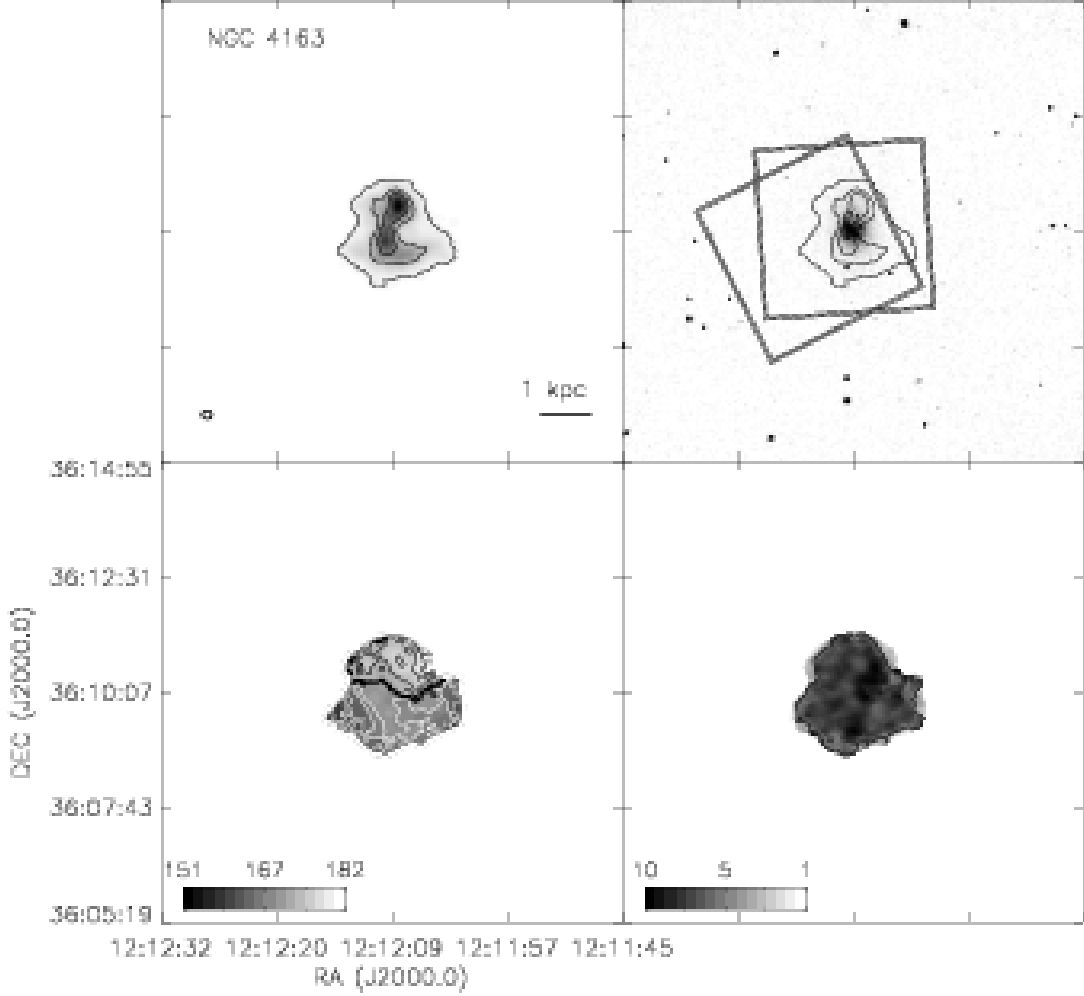


Fig. 18.— continued. *Top left:* The integrated H I intensity map for NGC 4163. The grayscale covers a range from 1×10^{19} to $2.1 \times 10^{21} \text{ cm}^{-2}$ with contours of 1×10^{20} , 5×10^{20} , and $1 \times 10^{21} \text{ cm}^{-2}$. *Top Right:* An optical g-band image from the SDSS with the same column density contours overlaid. The HST ACS footprints are the fields covered by the ANGST survey. *Bottom Left:* The H I velocity field. Black contours (lighter gray scale) indicate approaching emission, white contours (darker gray scale) receding emission. The thick black contour is the central velocity ($v_{cen} = 161.6 \text{ km s}^{-1}$) and the isovelocity contours are spaced by $\Delta v = 3 \text{ km s}^{-1}$. *Bottom Right:* The H I velocity dispersion. Contours are plotted at 5 and 10 km s^{-1} . Colorbars are in units of km s^{-1} .

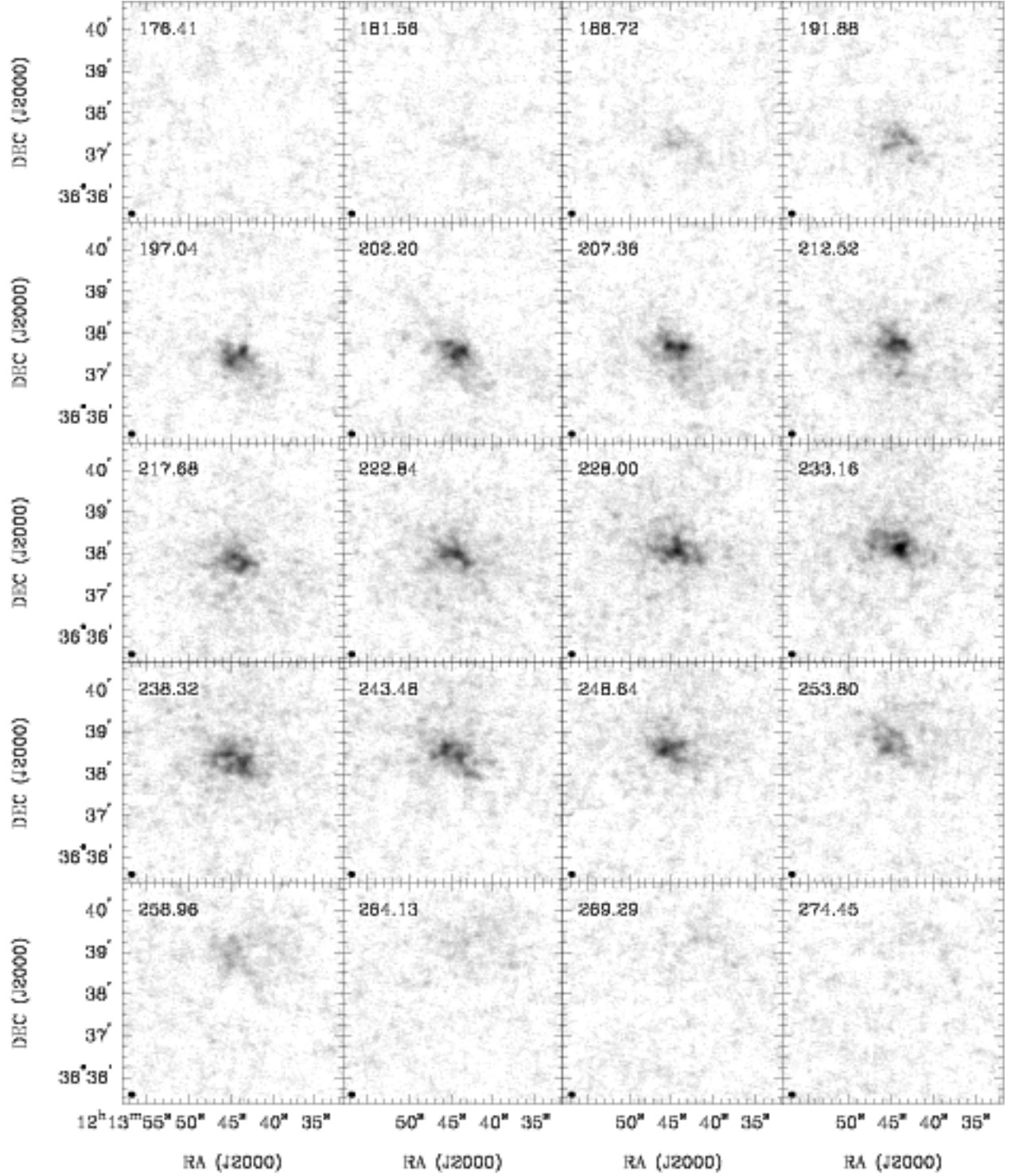


Fig. 19.— **NGC 4190**: Channel maps based on the natural-weighted cube (grayscale range: -0.02 to $14.7 \text{ mJy beam}^{-1}$). Every third channel is shown (channel width 1.3 km s^{-1}) and each map has the same size as the moment maps in the following panels.

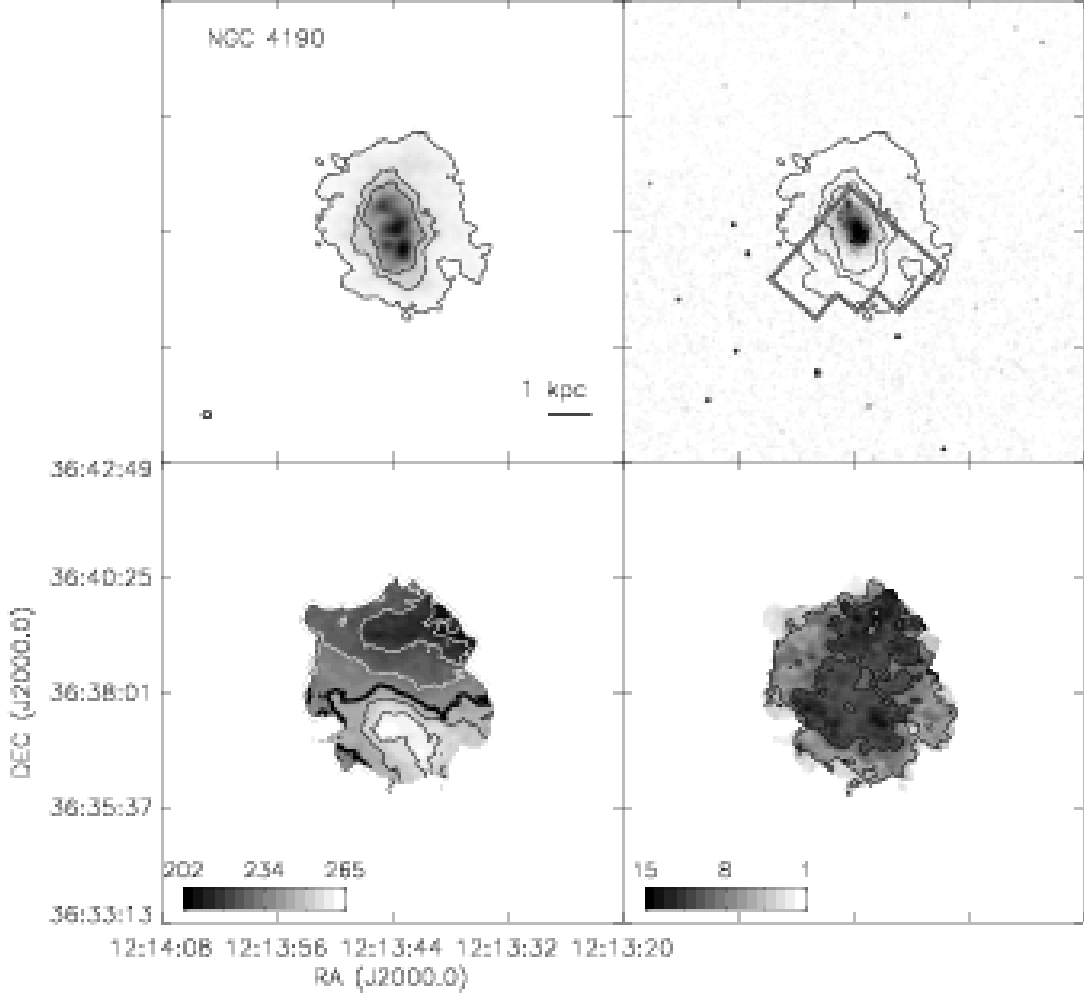


Fig. 19.— continued. *Top left:* The integrated H I intensity map for NGC 4190. The grayscale covers a range from 1×10^{19} to $3.5 \times 10^{21} \text{ cm}^{-2}$ with contours of 1×10^{20} , 5×10^{20} , and $1 \times 10^{21} \text{ cm}^{-2}$. *Top Right:* An optical g-band image from the SDSS with the same column density contours overlaid. The HST WFPC2 footprint is the field covered by the ANGST survey. *Bottom Left:* The H I velocity field. Black contours (lighter gray scale) indicate approaching emission, white contours (darker gray scale) receding emission. The thick black contour is the central velocity ($v_{cen} = 227.0 \text{ km s}^{-1}$) and the isovelocity contours are spaced by $\Delta v = 10 \text{ km s}^{-1}$. *Bottom Right:* The H I velocity dispersion. Contours are plotted at 5, 10, and 15 km s^{-1} . Colorbars are in units of km s^{-1} .

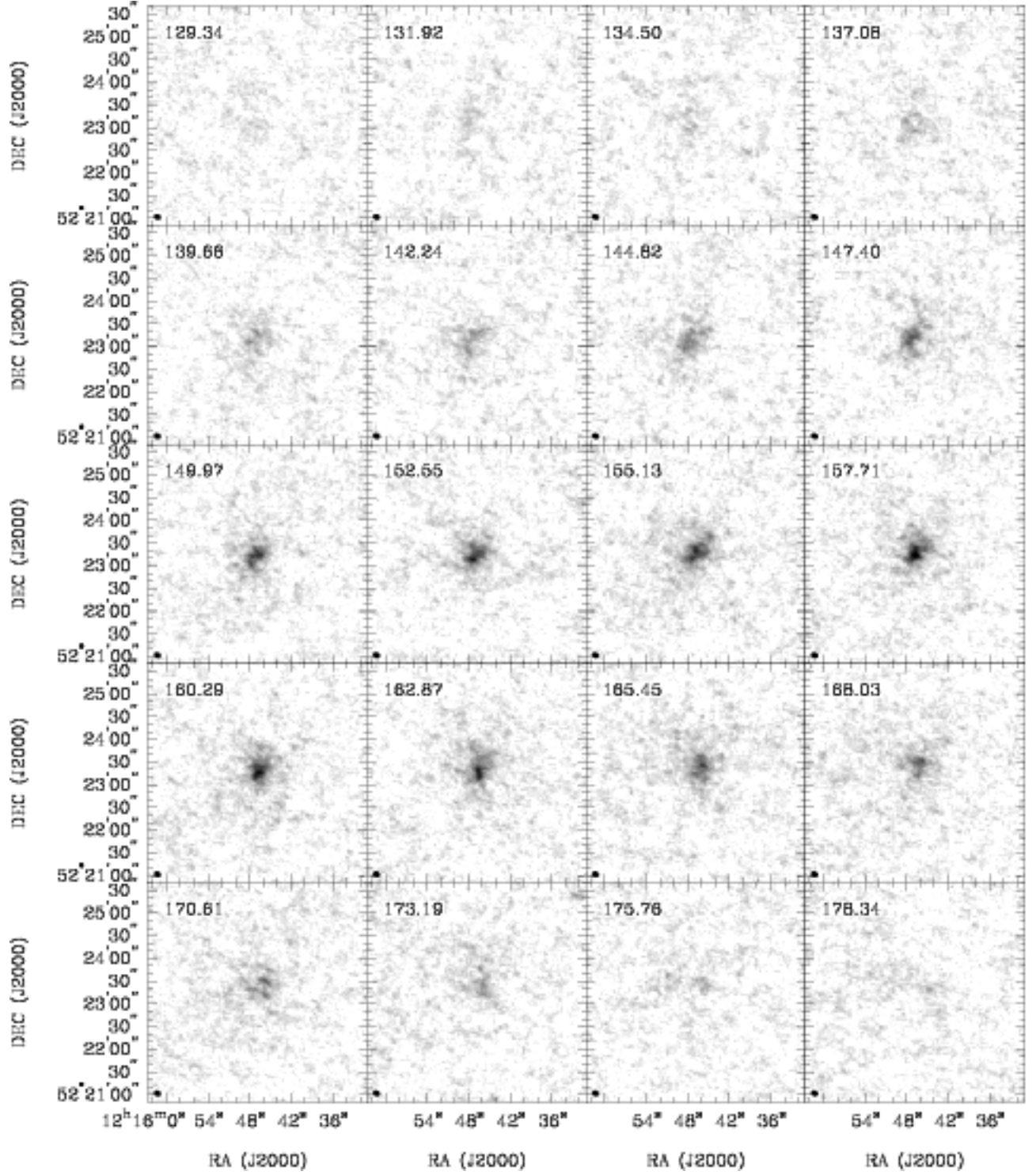


Fig. 20.— **MCG +09-20-131**: Channel maps based on the natural-weighted cube (grayscale range: -0.02 to $12.3 \text{ mJy beam}^{-1}$). Every channel is shown (channel width 1.3 km s^{-1}) and each map has the same size as the moment maps in the following panels.

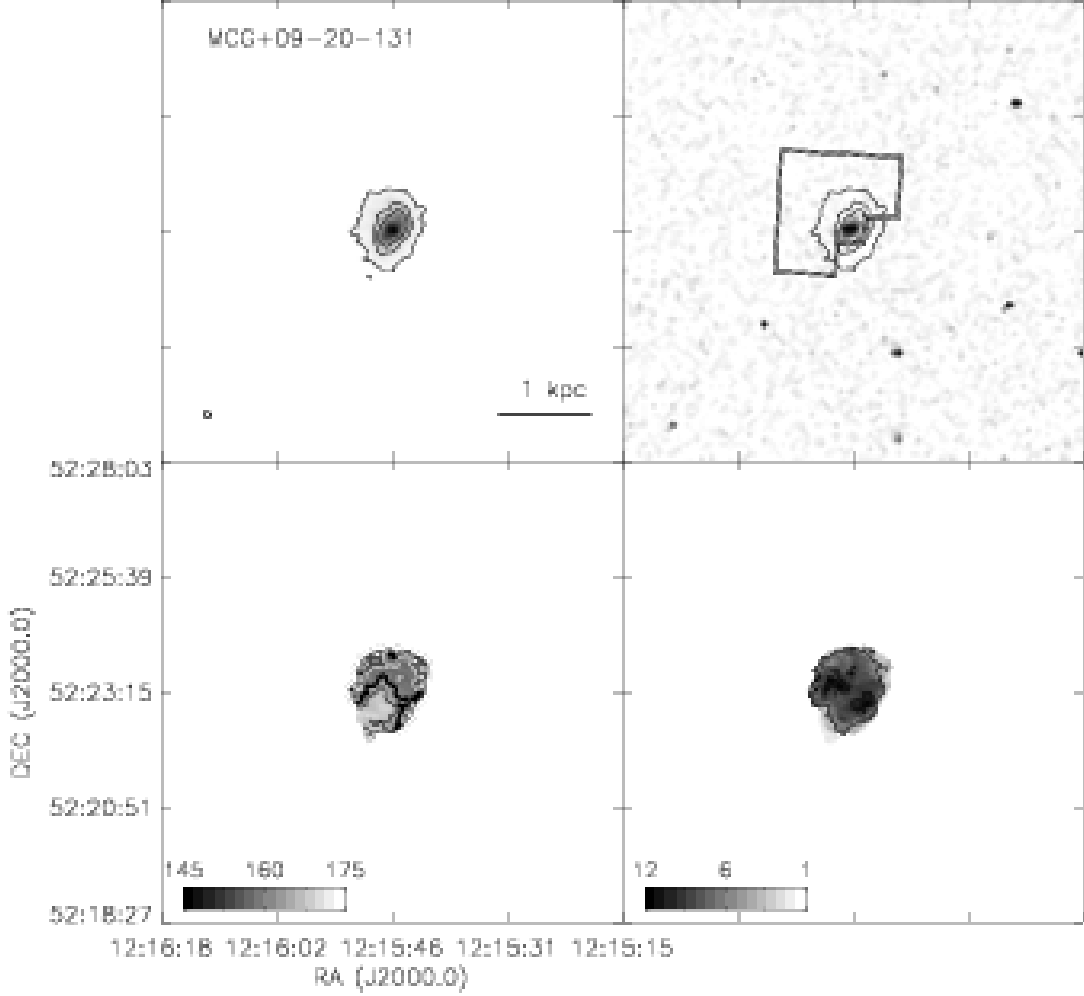


Fig. 20.— continued. *Top left:* The integrated H I intensity map for MCG +09-20-131. The grayscale covers a range from 1×10^{19} to $3.3 \times 10^{21} \text{ cm}^{-2}$ with contours of 1×10^{20} , 5×10^{20} , and $1 \times 10^{21} \text{ cm}^{-2}$. *Top Right:* An optical g-band image from the SDSS with the same column density contours overlaid. The HST WFPC2 footprint is the field covered by the ANGST survey. *Bottom Left:* The H I velocity field. Black contours (lighter gray scale) indicate approaching emission, white contours (darker gray scale) receding emission. The thick black contour is the central velocity ($v_{\text{cen}} = 157.6 \text{ km s}^{-1}$) and the isovelocity contours are spaced by $\Delta v = 5 \text{ km s}^{-1}$. *Bottom Right:* The H I velocity dispersion. Contours are plotted at 5 and 10 km s^{-1} . Colorbars are in units of km s^{-1} .

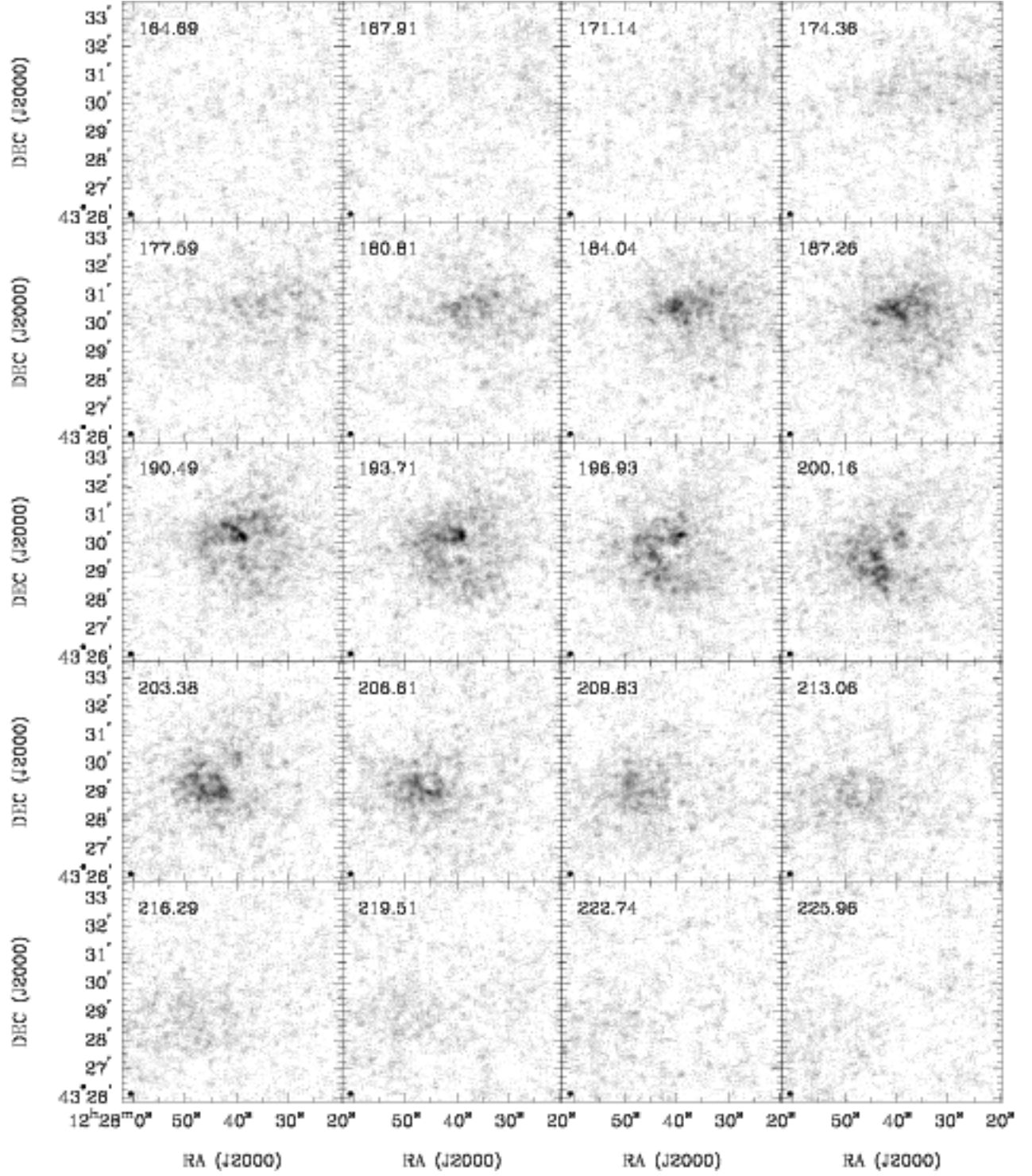


Fig. 21.— **DDO 125**: Channel maps based on the natural-weighted cube (grayscale range: -0.02 to $16.0 \text{ mJy beam}^{-1}$). Every fourth channel is shown (channel width 0.6 km s^{-1}) and each map has the same size as the moment maps in the following panels.

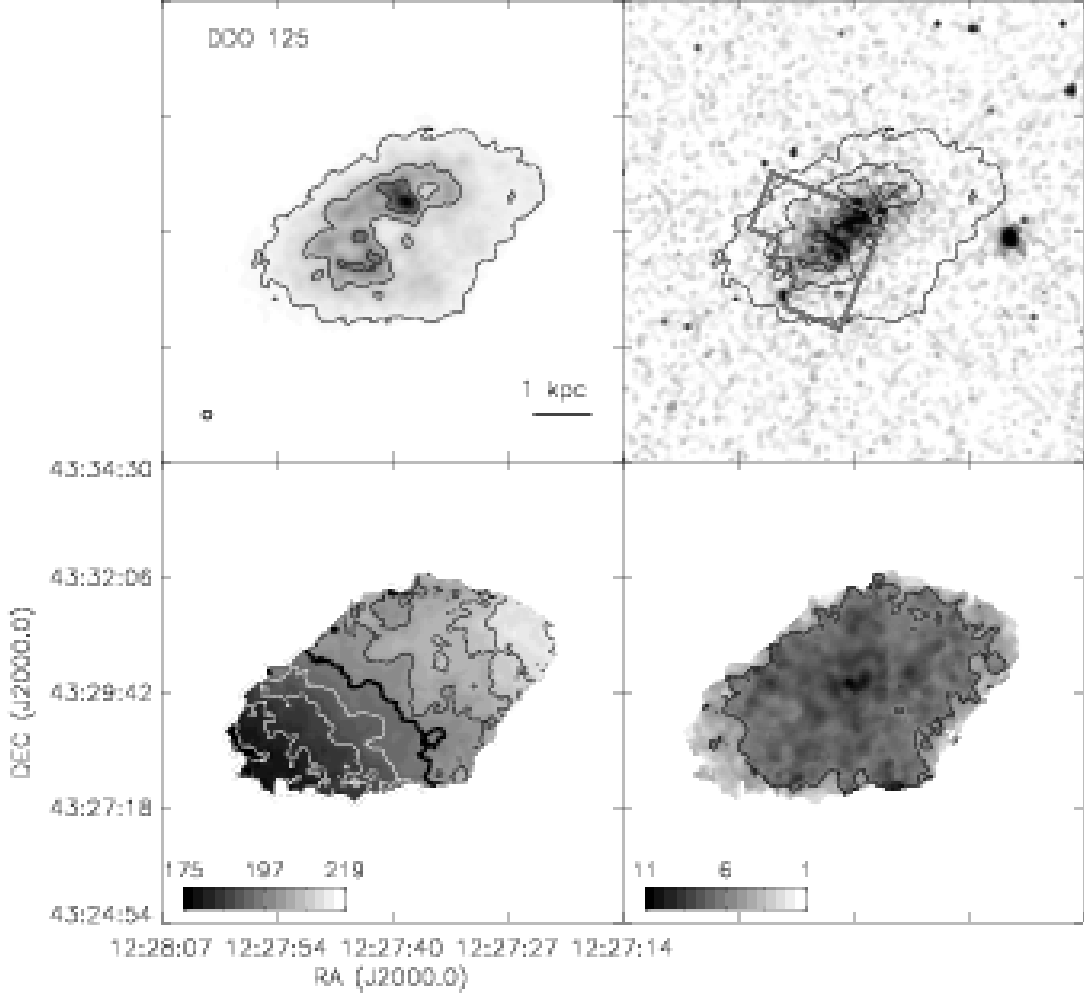


Fig. 21.— continued. *Top left:* The integrated H I intensity map for DDO 125. The grayscale covers a range from 1×10^{19} to $2.1 \times 10^{21} \text{ cm}^{-2}$ with contours of 1×10^{20} , 5×10^{20} , and $1 \times 10^{21} \text{ cm}^{-2}$. *Top Right:* An optical g-band image from the SDSS with the same column density contours overlaid. The HST WFPC2 footprint is the field covered by the ANGST survey. *Bottom Left:* The H I velocity field. Black contours (lighter gray scale) indicate approaching emission, white contours (darker gray scale) receding emission. The thick black contour is the central velocity ($v_{cen} = 196.1 \text{ km s}^{-1}$) and the isovelocity contours are spaced by $\Delta v = 5 \text{ km s}^{-1}$. *Bottom Right:* The H I velocity dispersion. Contours are plotted at 5 and 10 km s^{-1} . Colorbars are in units of km s^{-1} .

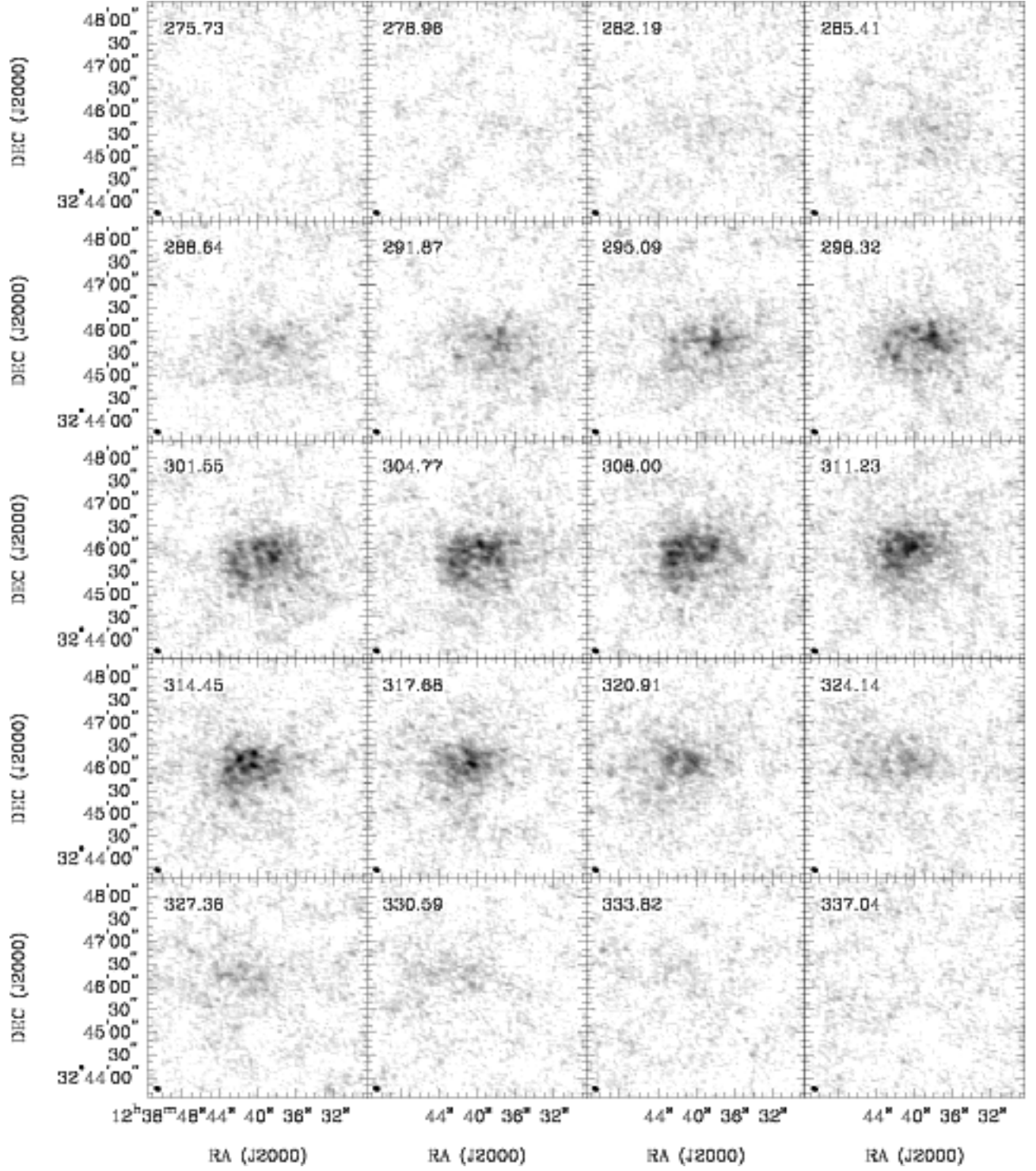


Fig. 22.— **UGCA 292**: Channel maps based on the natural-weighted cube (grayscale range: -0.02 to $15.8 \text{ mJy beam}^{-1}$). Every fourth channel is shown (channel width 0.6 km s^{-1}) and each map has the same size as the moment maps in the following panels.

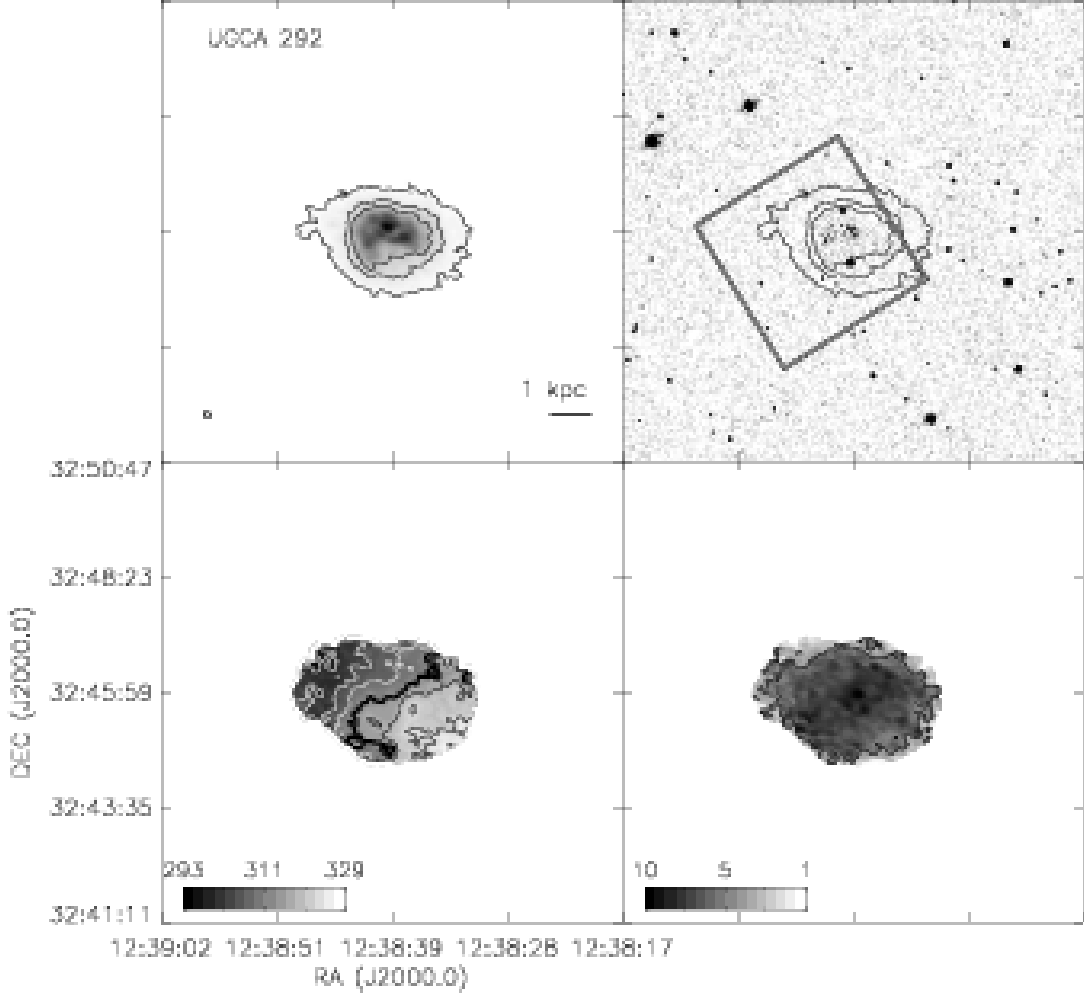


Fig. 22.— continued. *Top left:* The integrated H I intensity map for UGCA 292. The grayscale covers a range from 1×10^{19} to $4.2 \times 10^{21} \text{ cm}^{-2}$ with contours of 1×10^{20} , 5×10^{20} , and $1 \times 10^{21} \text{ cm}^{-2}$. *Top Right:* An optical g-band image from the SDSS with the same column density contours overlaid. The HST ACS footprint is the field covered by the ANGST survey. *Bottom Left:* The H I velocity field. Black contours (lighter gray scale) indicate approaching emission, white contours (darker gray scale) receding emission. The thick black contour is the central velocity ($v_{cen} = 308.3 \text{ km s}^{-1}$) and the isovelocity contours are spaced by $\Delta v = 5 \text{ km s}^{-1}$. *Bottom Right:* The H I velocity dispersion. Contours are plotted at 5 and 10 km s^{-1} . Colorbars are in units of km s^{-1} .

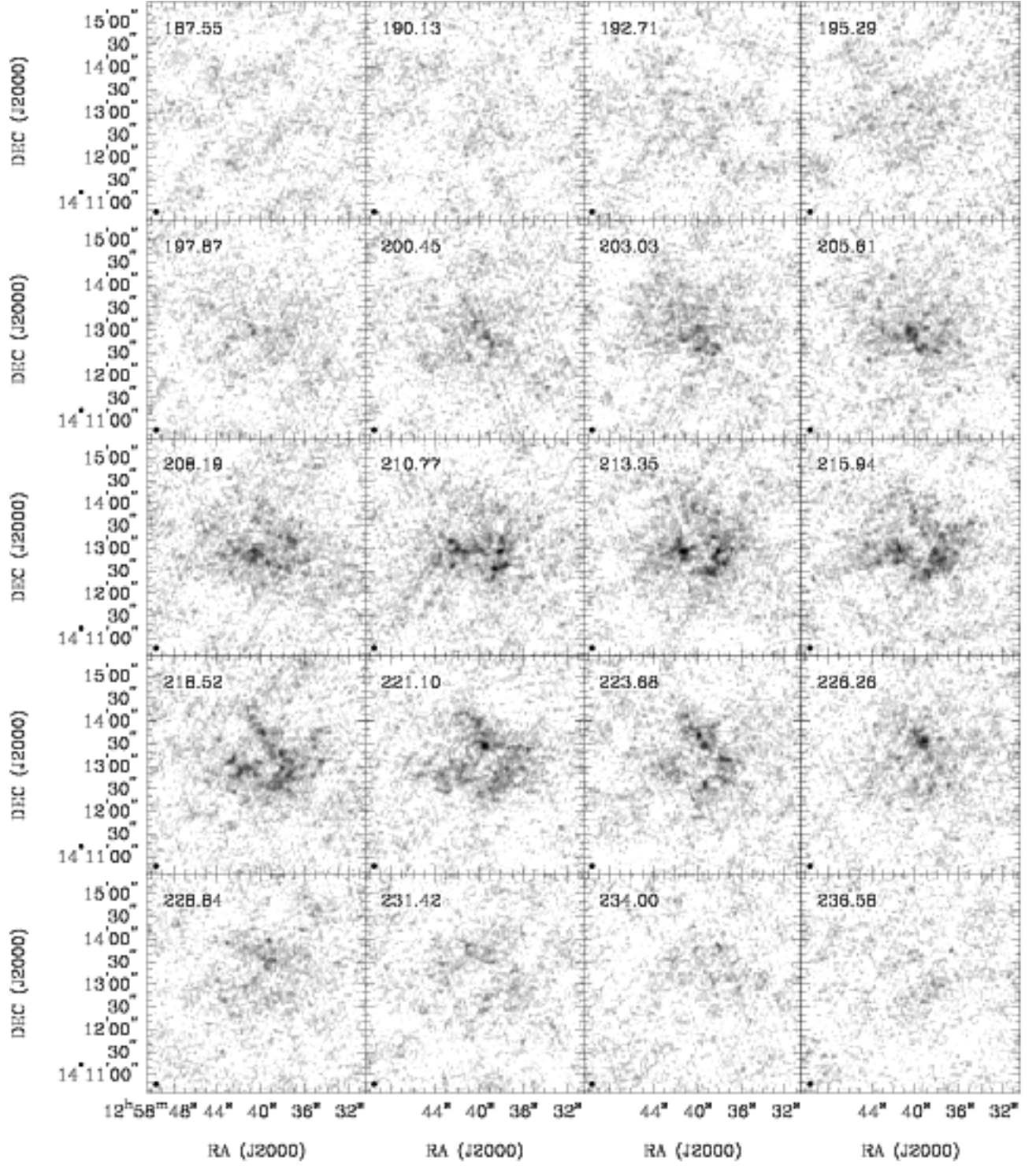


Fig. 23.— **GR 8:** Channel maps based on the natural-weighted cube (grayscale range: -0.02 to $10.6 \text{ mJy beam}^{-1}$). Every third channel is shown (channel width 0.6 km s^{-1}) and each map has the same size as the moment maps in the following panels.

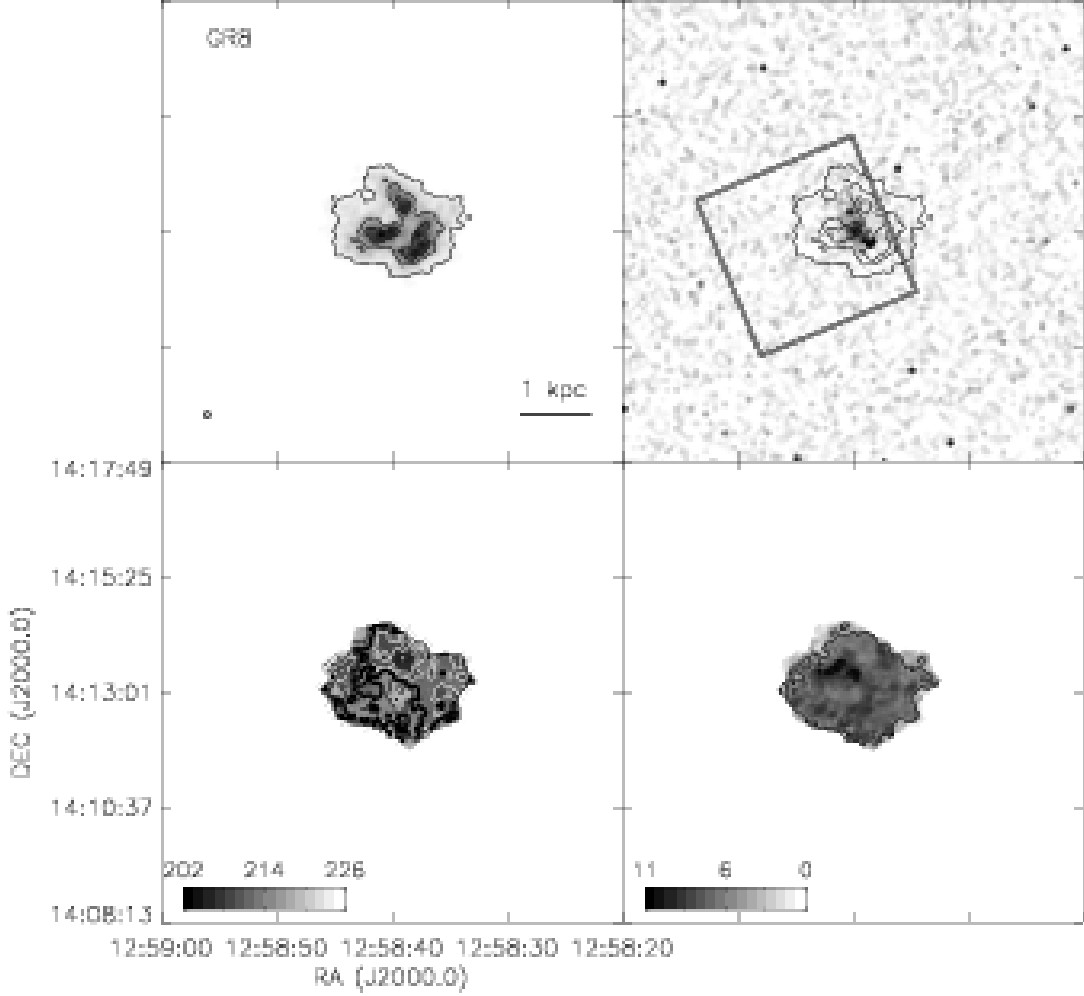


Fig. 23.— continued. *Top left:* The integrated H I intensity map for GR 8. The grayscale covers a range from 1×10^{19} to $1.7 \times 10^{21} \text{ cm}^{-2}$ with contours of 1×10^{20} , 5×10^{20} , and $1 \times 10^{21} \text{ cm}^{-2}$. *Top Right:* An optical g-band image from the SDSS with the same column density contours overlaid. The HST ACS footprint is the field covered by the ANGST survey. *Bottom Left:* The H I velocity field. Black contours (lighter gray scale) indicate approaching emission, white contours (darker gray scale) receding emission. The thick black contour is the central velocity ($v_{\text{cen}} = 213.7 \text{ km s}^{-1}$) and the isovelocity contours are spaced by $\Delta v = 3 \text{ km s}^{-1}$. *Bottom Right:* The H I velocity dispersion. Contours are plotted at 5 and 10 km s^{-1} . Colorbars are in units of km s^{-1} .

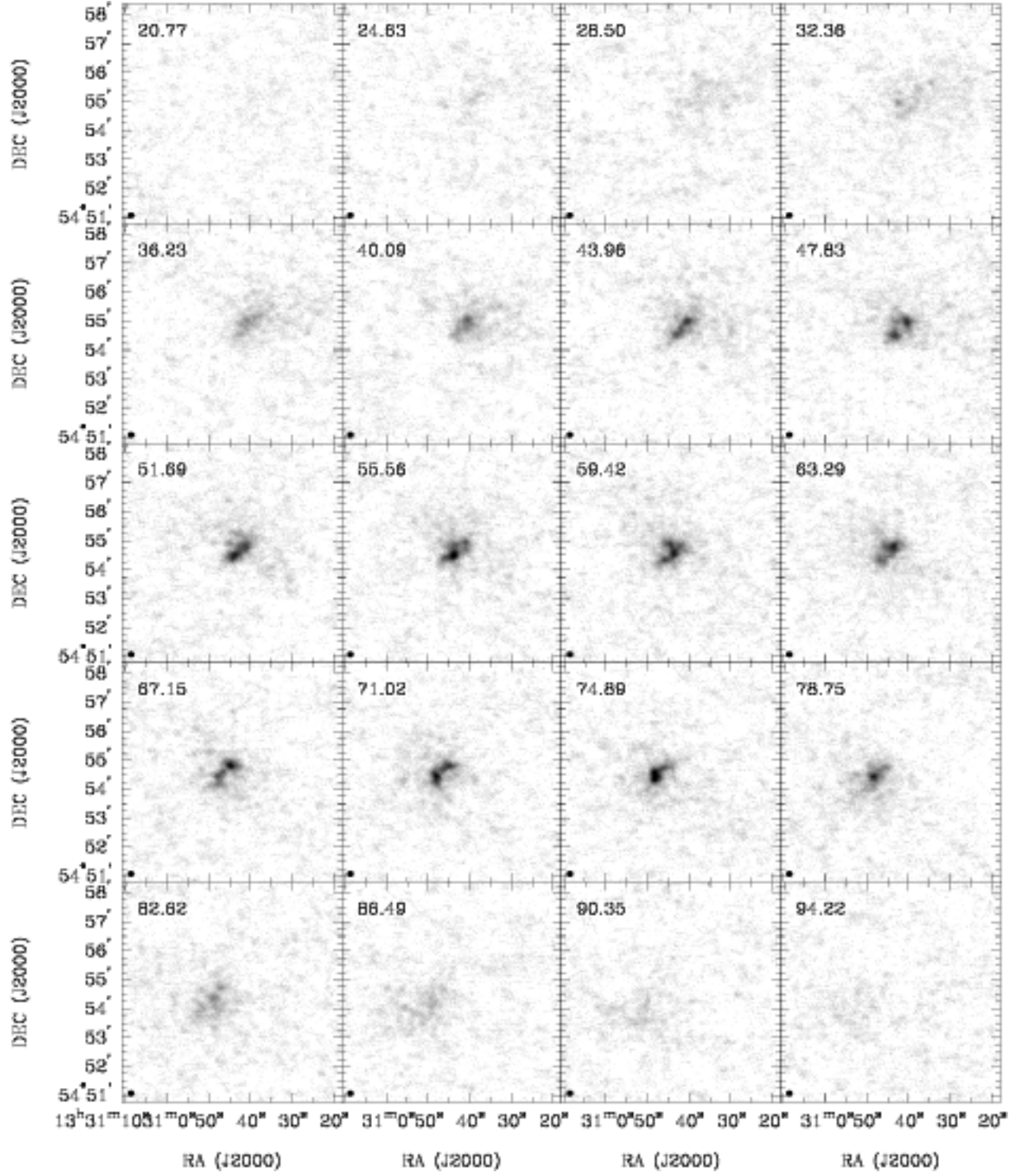


Fig. 24.— **UGC 8508**: Channel maps based on the natural-weighted cube (grayscale range: -0.02 to $23.0 \text{ mJy beam}^{-1}$). Every fifth channel is shown (channel width 0.6 km s^{-1}) and each map has the same size as the moment maps in the following panels.

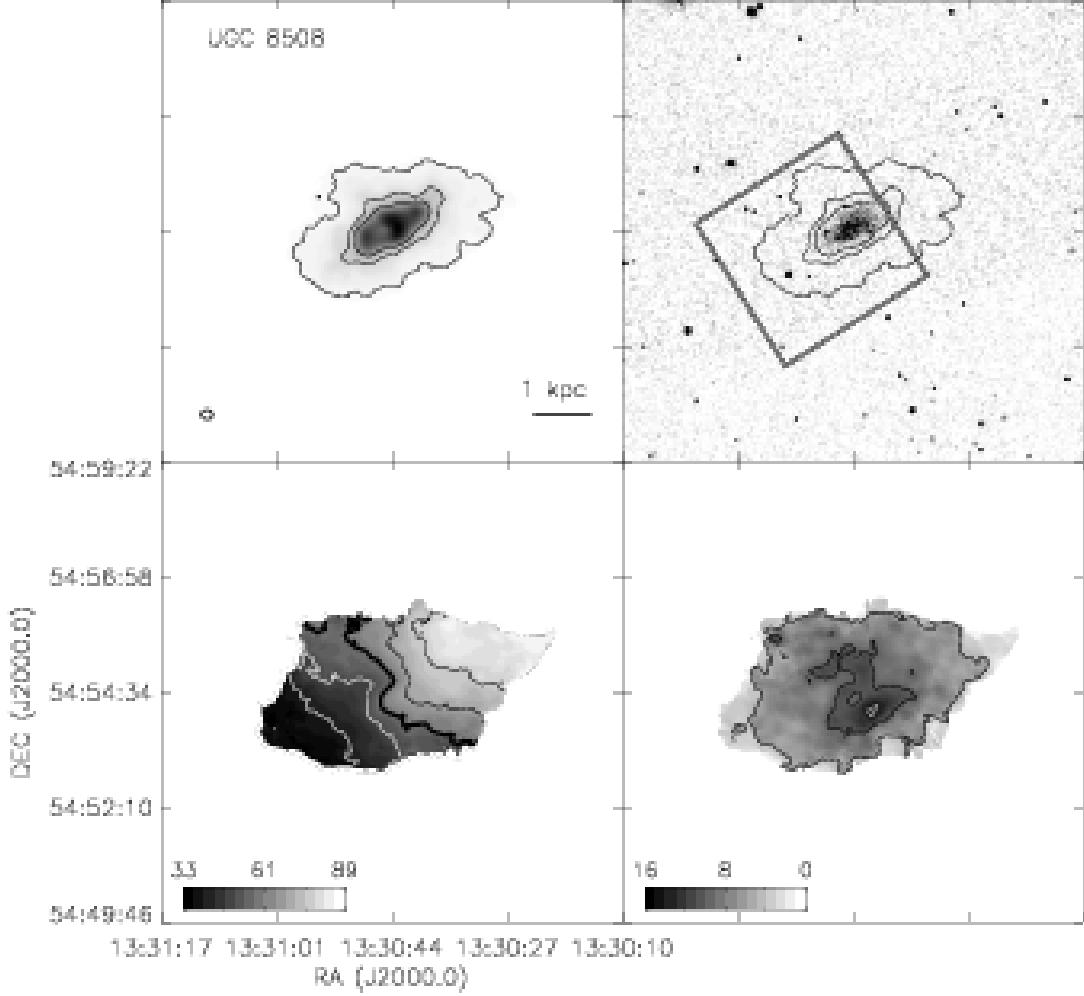


Fig. 24.— continued. *Top left:* The integrated H I intensity map for UGC 8508. The grayscale covers a range from 1×10^{19} to $2.9 \times 10^{21} \text{ cm}^{-2}$ with contours of 1×10^{20} , 5×10^{20} , and $1 \times 10^{21} \text{ cm}^{-2}$. *Top Right:* An optical g-band image from the SDSS with the same column density contours overlaid. The HST ACS footprint is the field covered by the ANGST survey. *Bottom Left:* The H I velocity field. Black contours (lighter gray scale) indicate approaching emission, white contours (darker gray scale) receding emission. The thick black contour is the central velocity ($v_{\text{cen}} = 62.0 \text{ km s}^{-1}$) and the isovelocity contours are spaced by $\Delta v = 10 \text{ km s}^{-1}$. *Bottom Right:* The H I velocity dispersion. Contours are plotted at 5, 10, and 15 km s^{-1} . Colorbars are in units of km s^{-1} .

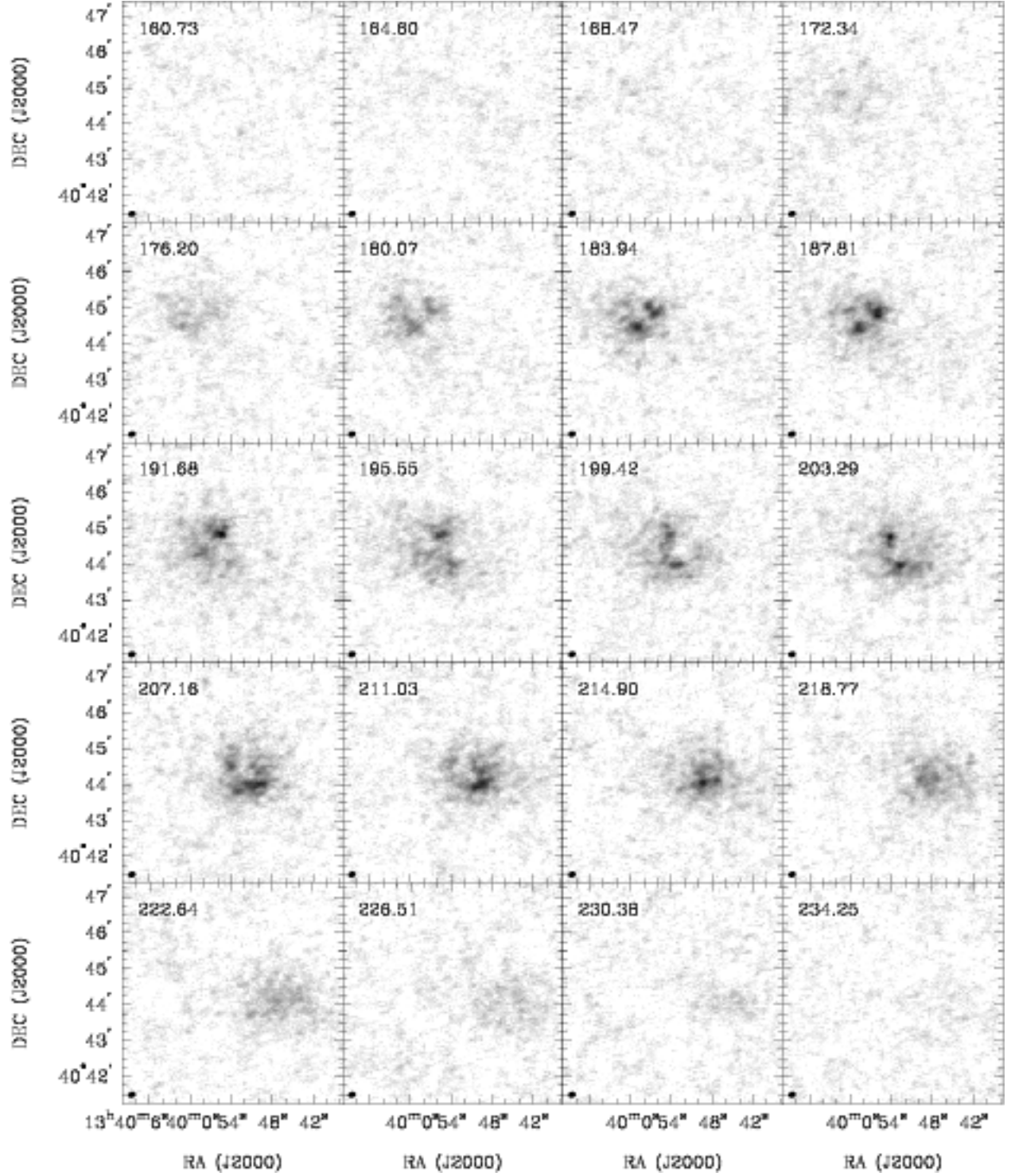


Fig. 25.— **DDO 181**: Channel maps based on the natural-weighted cube (grayscale range: -0.02 to $13.9 \text{ mJy beam}^{-1}$). Every second channel is shown (channel width 1.3 km s^{-1}) and each map has the same size as the moment maps in the following panels.

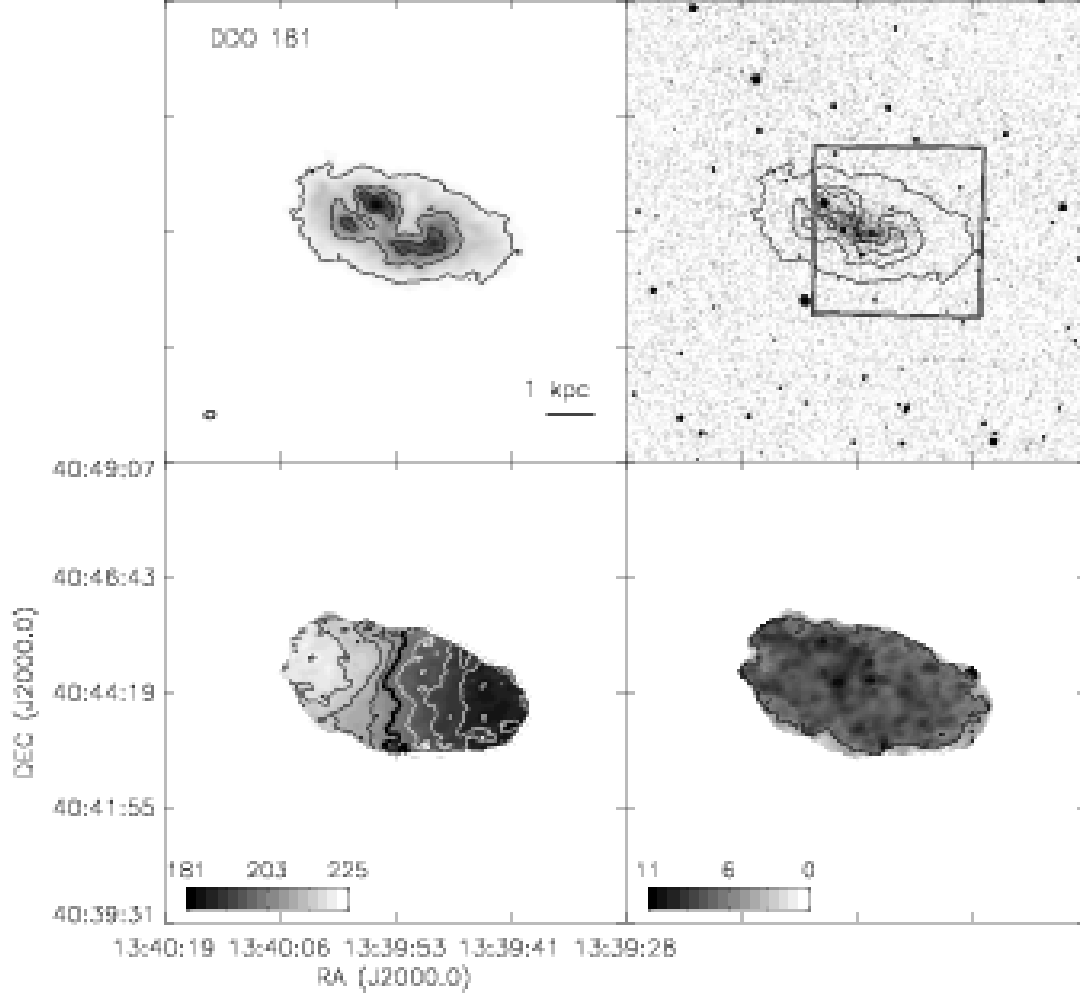


Fig. 25.— continued. *Top left:* The integrated H I intensity map for DDO 181. The grayscale covers a range from 1×10^{19} to $1.7 \times 10^{21} \text{ cm}^{-2}$ with contours of 1×10^{20} , 5×10^{20} , and $1 \times 10^{21} \text{ cm}^{-2}$. *Top Right:* An optical g-band image from the SDSS with the same column density contours overlaid. The HST ACS footprint is the field covered by the ANGST survey. *Bottom Left:* The H I velocity field. Black contours (lighter gray scale) indicate approaching emission, white contours (darker gray scale) receding emission. The thick black contour is the central velocity ($v_{cen} = 201.4 \text{ km s}^{-1}$) and the isovelocity contours are spaced by $\Delta v = 5 \text{ km s}^{-1}$. *Bottom Right:* The H I velocity dispersion. Contours are plotted at 5 and 10 km s^{-1} . Colorbars are in units of km s^{-1} .

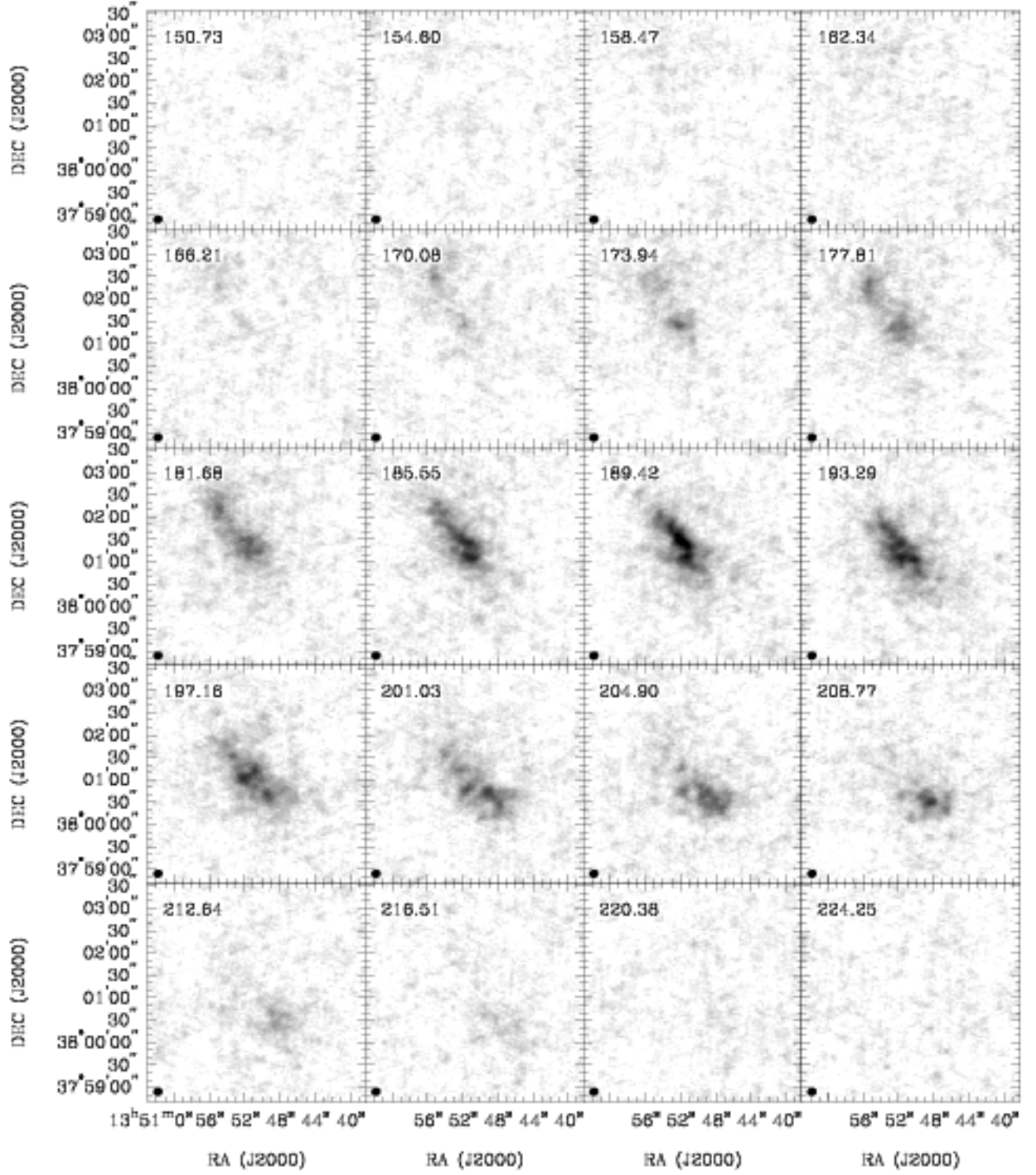


Fig. 26.— **DDO 183**: Channel maps based on the natural-weighted cube (grayscale range: -0.02 to $15.7 \text{ mJy beam}^{-1}$). Every second channel is shown (channel width 1.3 km s^{-1}) and each map has the same size as the moment maps in the following panels.

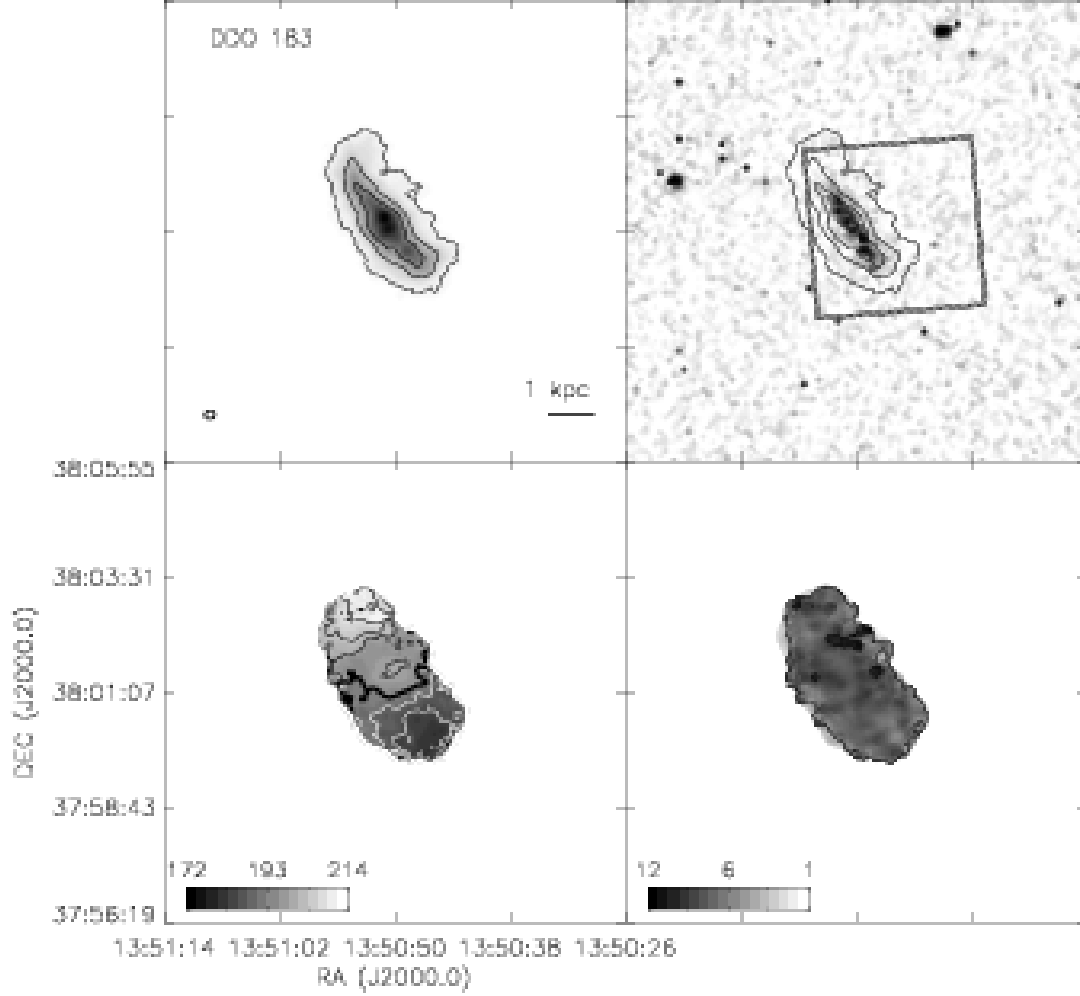


Fig. 26.— continued. *Top left:* The integrated H I intensity map for DDO 183. The grayscale covers a range from 1×10^{19} to $2.2 \times 10^{21} \text{ cm}^{-2}$ with contours of 1×10^{20} , 5×10^{20} , and $1 \times 10^{21} \text{ cm}^{-2}$. *Top Right:* An optical g-band image from the SDSS with the same column density contours overlaid. The HST ACS footprint is the field covered by the ANGST survey. *Bottom Left:* The H I velocity field. Black contours (lighter gray scale) indicate approaching emission, white contours (darker gray scale) receding emission. The thick black contour is the central velocity ($v_{cen} = 191.2 \text{ km s}^{-1}$) and the isovelocity contours are spaced by $\Delta v = 5 \text{ km s}^{-1}$. *Bottom Right:* The H I velocity dispersion. Contours are plotted at 5 and 10 km s^{-1} . Colorbars are in units of km s^{-1} .

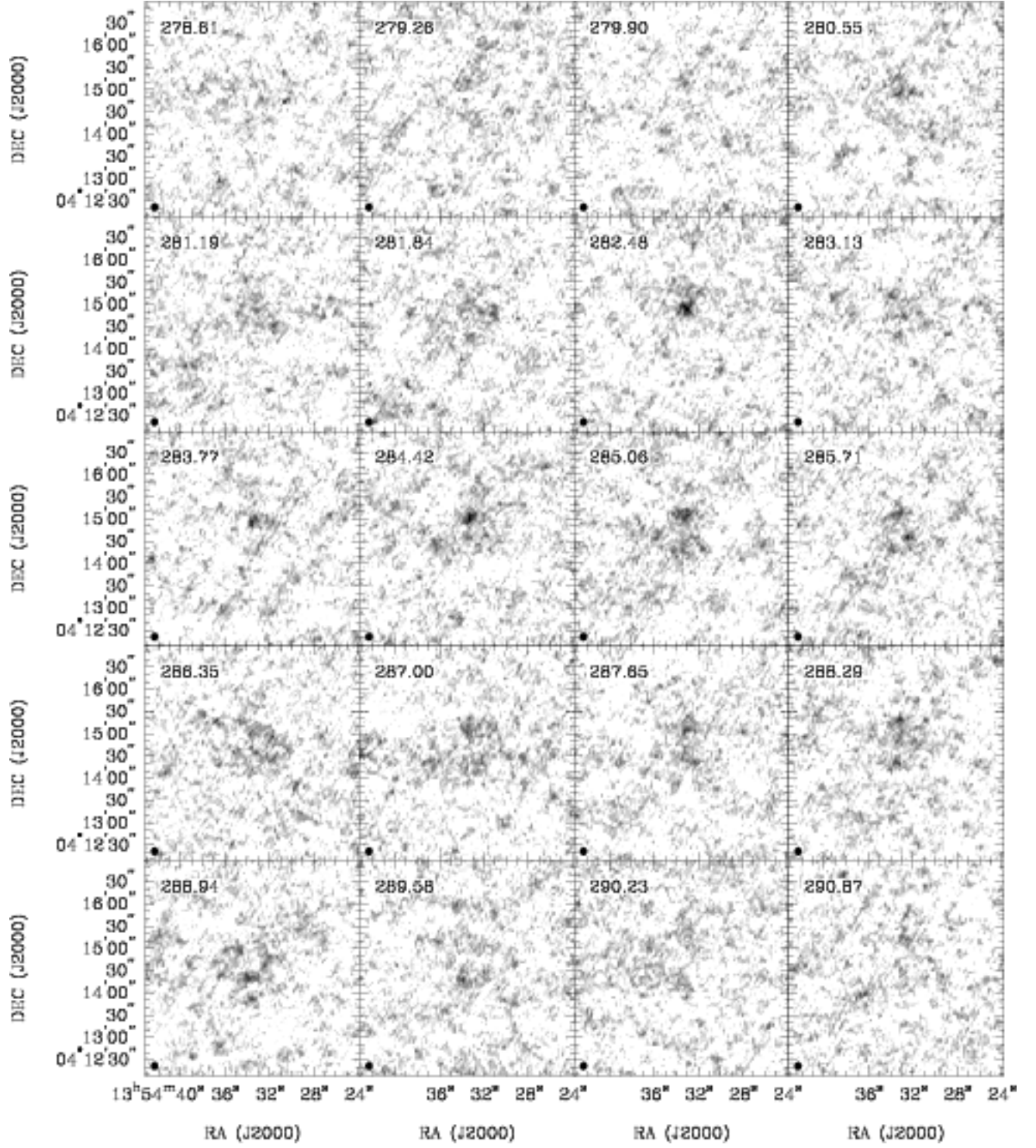


Fig. 27.— **KKH 86**: Channel maps based on the natural-weightedcube (grayscale range: -0.02 to $7.7 \text{ mJy beam}^{-1}$). Every channel is shown (channel width 0.6 km s^{-1}) and each map has the same size as the moment maps in the following panels.

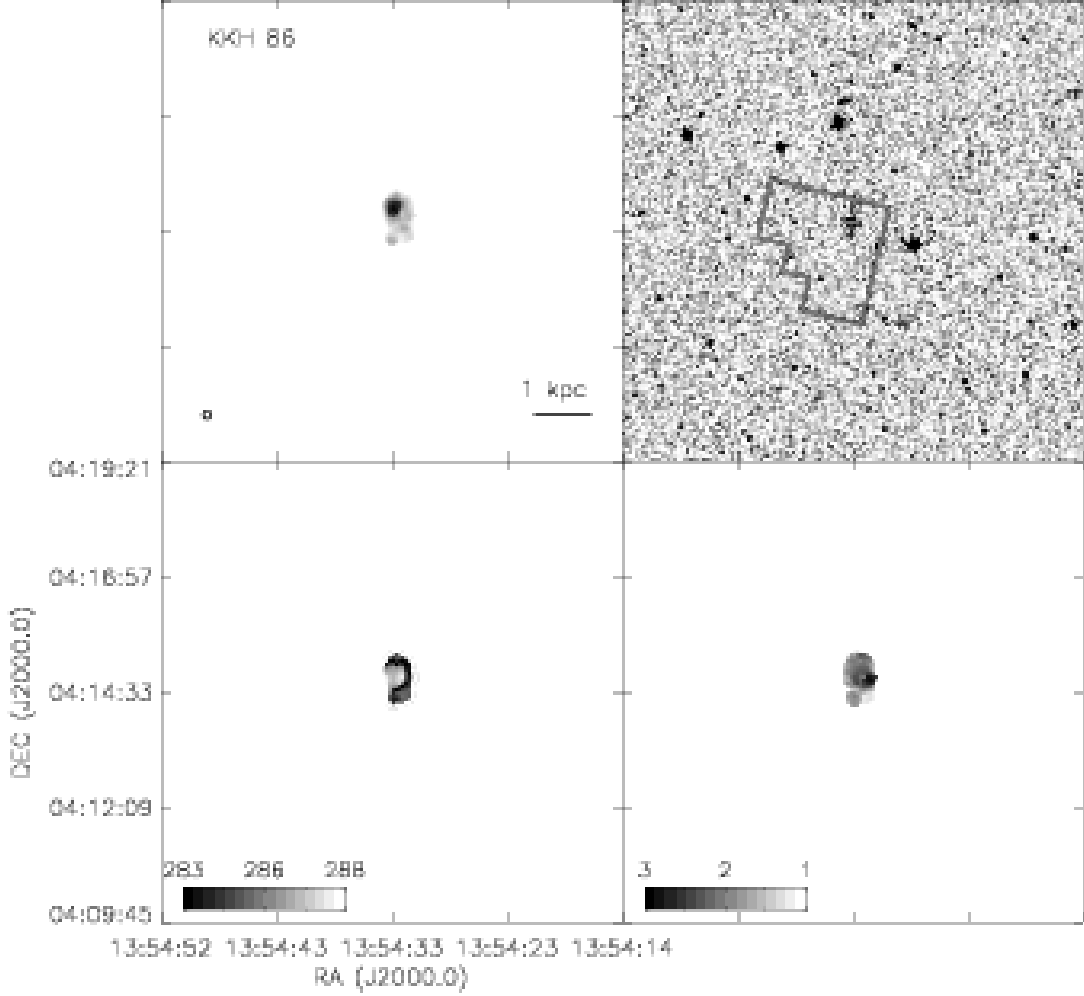


Fig. 27.— continued. *Top left:* The integrated H I intensity map for KKH 86. The grayscale covers a range from 1×10^{19} to $1.5 \times 10^{20} \text{ cm}^{-2}$ with a contour of $1 \times 10^{20} \text{ cm}^{-2}$. *Top Right:* An optical g-band image from the SDSS with the same column density contours overlaid. The HST WFPC2 footprint is the field covered by the ANGST survey. *Bottom Left:* The H I velocity field. Black contours (lighter gray scale) indicate approaching emission, white contours (darker gray scale) receding emission. The thick black contour is the central velocity ($v_{\text{cen}} = 285.5 \text{ km s}^{-1}$) and the isovelocity contours are spaced by $\Delta v = 10 \text{ km s}^{-1}$. *Bottom Right:* The H I velocity dispersion. Colorbars are in units of km s^{-1} .

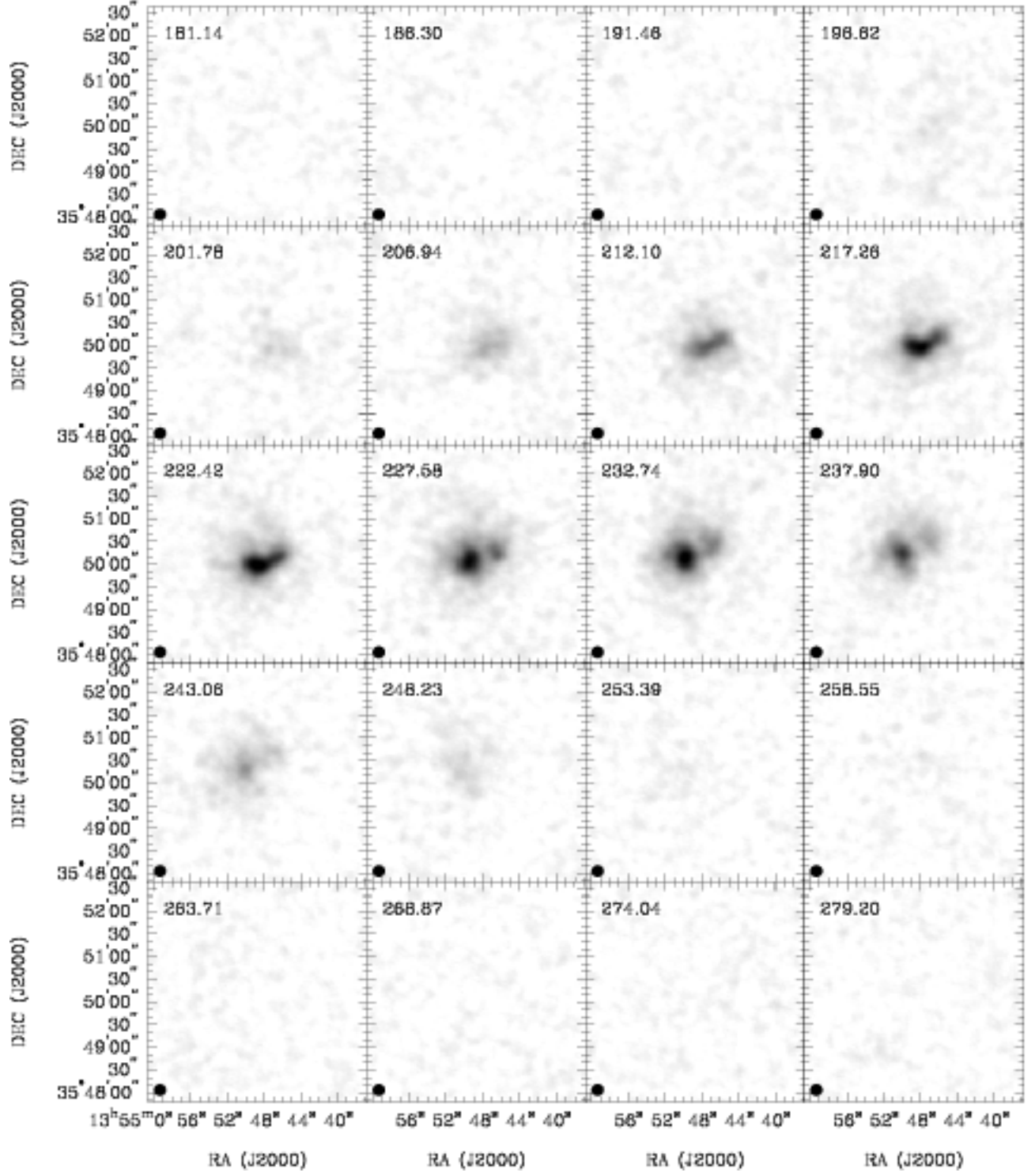


Fig. 28.— **UGC 8833**: Channel maps based on the natural-weighted cube (grayscale range: -0.02 to $20.8 \text{ mJy beam}^{-1}$). Every channel is shown (channel width 2.6 km s^{-1}) and each map has the same size as the moment maps in the following panels.

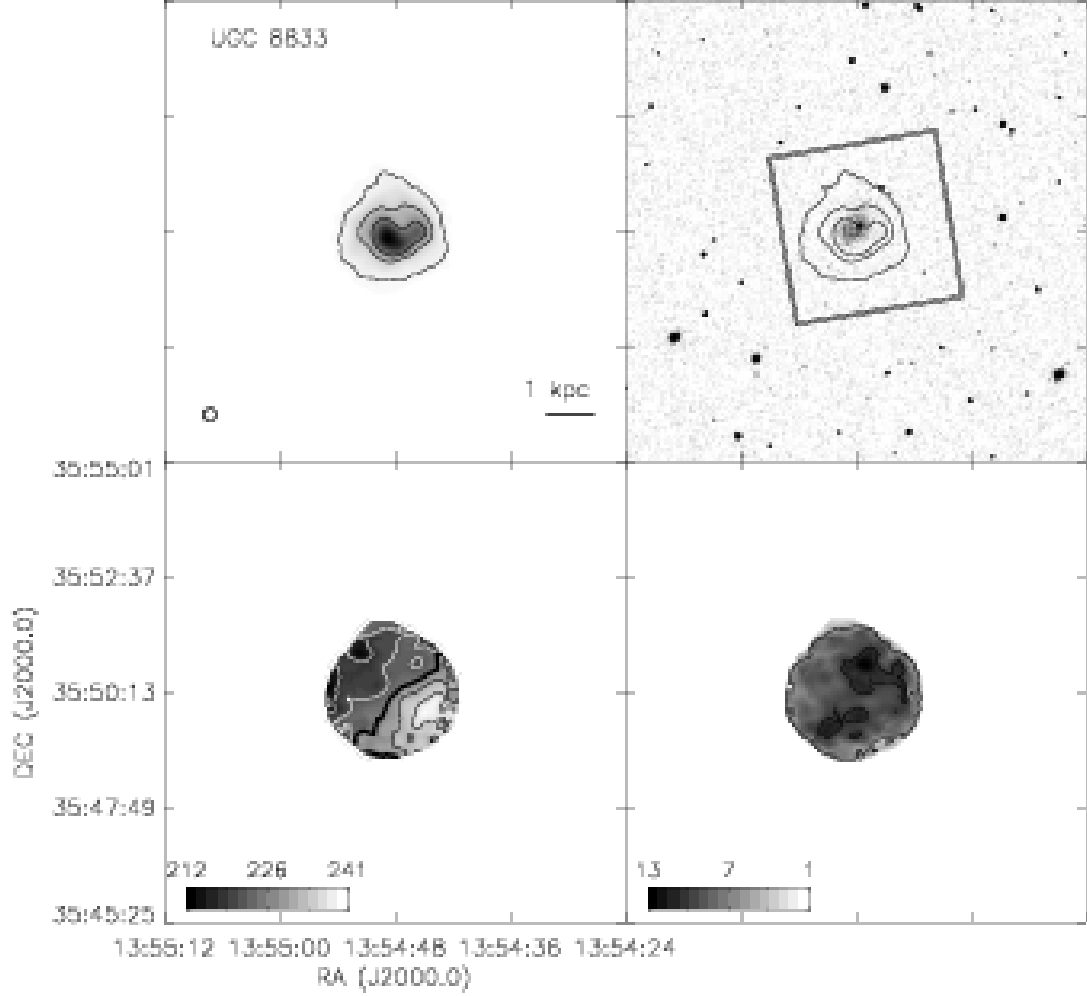


Fig. 28.— continued. *Top left:* The integrated H I intensity map for UGC 8833. The grayscale covers a range from 1×10^{19} to $2.2 \times 10^{21} \text{ cm}^{-2}$ with contours of 1×10^{20} , 5×10^{20} , and $1 \times 10^{21} \text{ cm}^{-2}$. *Top Right:* An optical g-band image from the SDSS with the same column density contours overlaid. The HST ACS footprint is the field covered by the ANGST survey. *Bottom Left:* The H I velocity field. Black contours (lighter gray scale) indicate approaching emission, white contours (darker gray scale) receding emission. The thick black contour is the central velocity ($v_{cen} = 225.9 \text{ km s}^{-1}$) and the isovelocity contours are spaced by $\Delta v = 5 \text{ km s}^{-1}$. *Bottom Right:* The H I velocity dispersion. Contours are plotted at 5 and 10 km s^{-1} . Colorbars are in units of km s^{-1} .

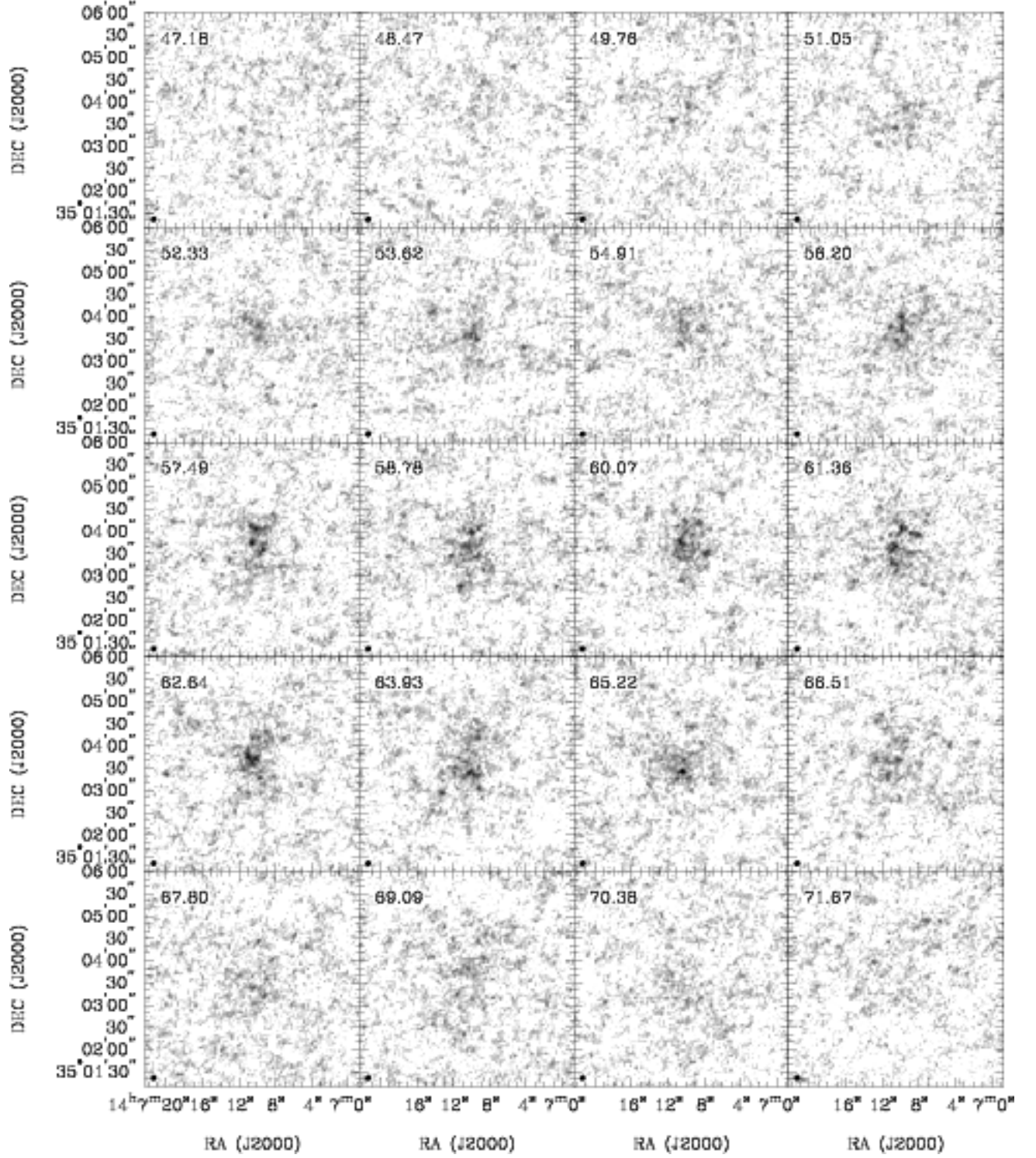


Fig. 29.— **KK 230**: Channel maps based on the natural-weighted cube (grayscale range: -0.02 to $8.2 \text{ mJy beam}^{-1}$). Every channel is shown (channel width 0.6 km s^{-1}) and each map has the same size as the moment maps in the following panels.

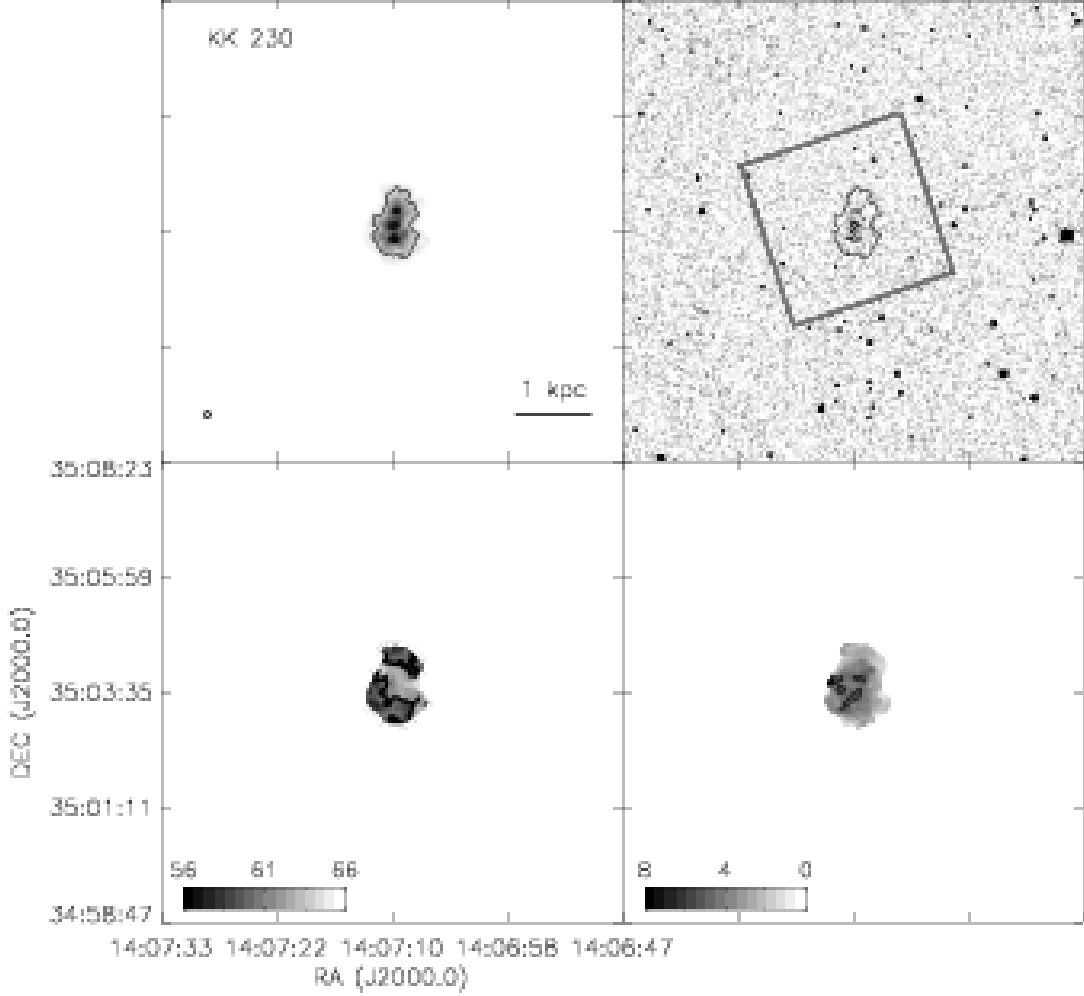


Fig. 29.— continued. *Top left:* The integrated H I intensity map for KK 230. The grayscale covers a range from 1×10^{19} to $6.1 \times 10^{20} \text{ cm}^{-2}$ with contours of 1×10^{20} and $5 \times 10^{20} \text{ cm}^{-2}$. *Top Right:* An optical g-band image from the SDSS with the same column density contours overlaid. The HST ACS footprint is the field covered by the ANGST survey. *Bottom Left:* The H I velocity field. Black contours (lighter gray scale) indicate approaching emission, white contours (darker gray scale) receding emission. The thick black contour is the central velocity ($v_{\text{cen}} = 60.6 \text{ km s}^{-1}$) and the isovelocity contours are spaced by $\Delta v = 5 \text{ km s}^{-1}$. *Bottom Right:* The H I velocity dispersion. A contour is plotted at 5 km s^{-1} . Colorbars are in units of km s^{-1} .

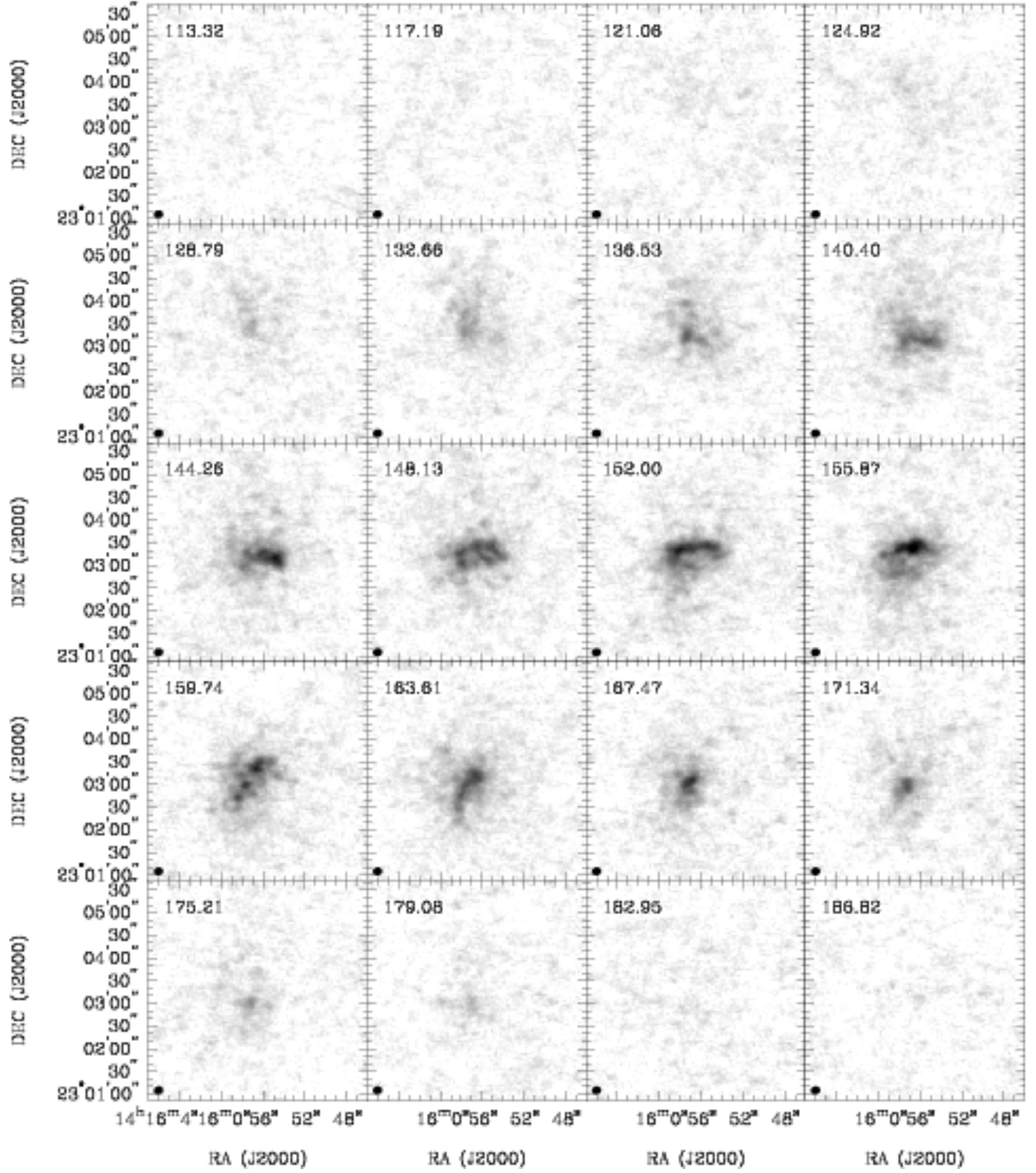


Fig. 30.— **DDO 187**: Channel maps based on the natural-weighted cube (grayscale range: -0.02 to $17.1 \text{ mJy beam}^{-1}$). Every second channel is shown (channel width 1.3 km s^{-1}) and each map has the same size as the moment maps in the following panels.

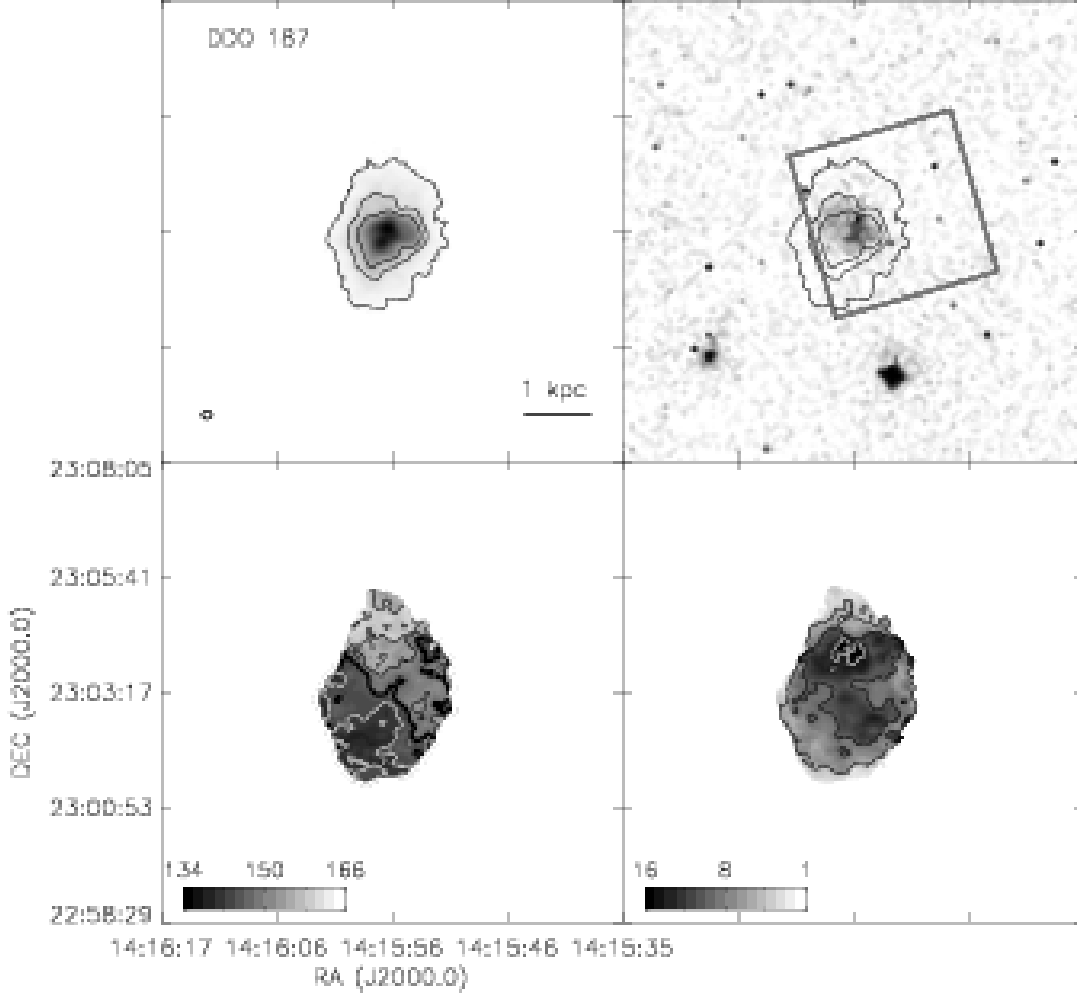


Fig. 30.— continued. *Top left:* The integrated H I intensity map for DDO 187. The grayscale covers a range from 1×10^{19} to $3.2 \times 10^{21} \text{ cm}^{-2}$ with contours of 1×10^{20} , 5×10^{20} , and $1 \times 10^{21} \text{ cm}^{-2}$. *Top Right:* An optical g-band image from the SDSS with the same column density contours overlaid. The HST ACS footprint is the field covered by the ANGST survey. *Bottom Left:* The H I velocity field. Black contours (lighter gray scale) indicate approaching emission, white contours (darker gray scale) receding emission. The thick black contour is the central velocity ($v_{\text{cen}} = 152.2 \text{ km s}^{-1}$) and the isovelocity contours are spaced by $\Delta v = 5 \text{ km s}^{-1}$. *Bottom Right:* The H I velocity dispersion. Contours are plotted at 5, 10, and 15 km s^{-1} . Colorbars are in units of km s^{-1} .

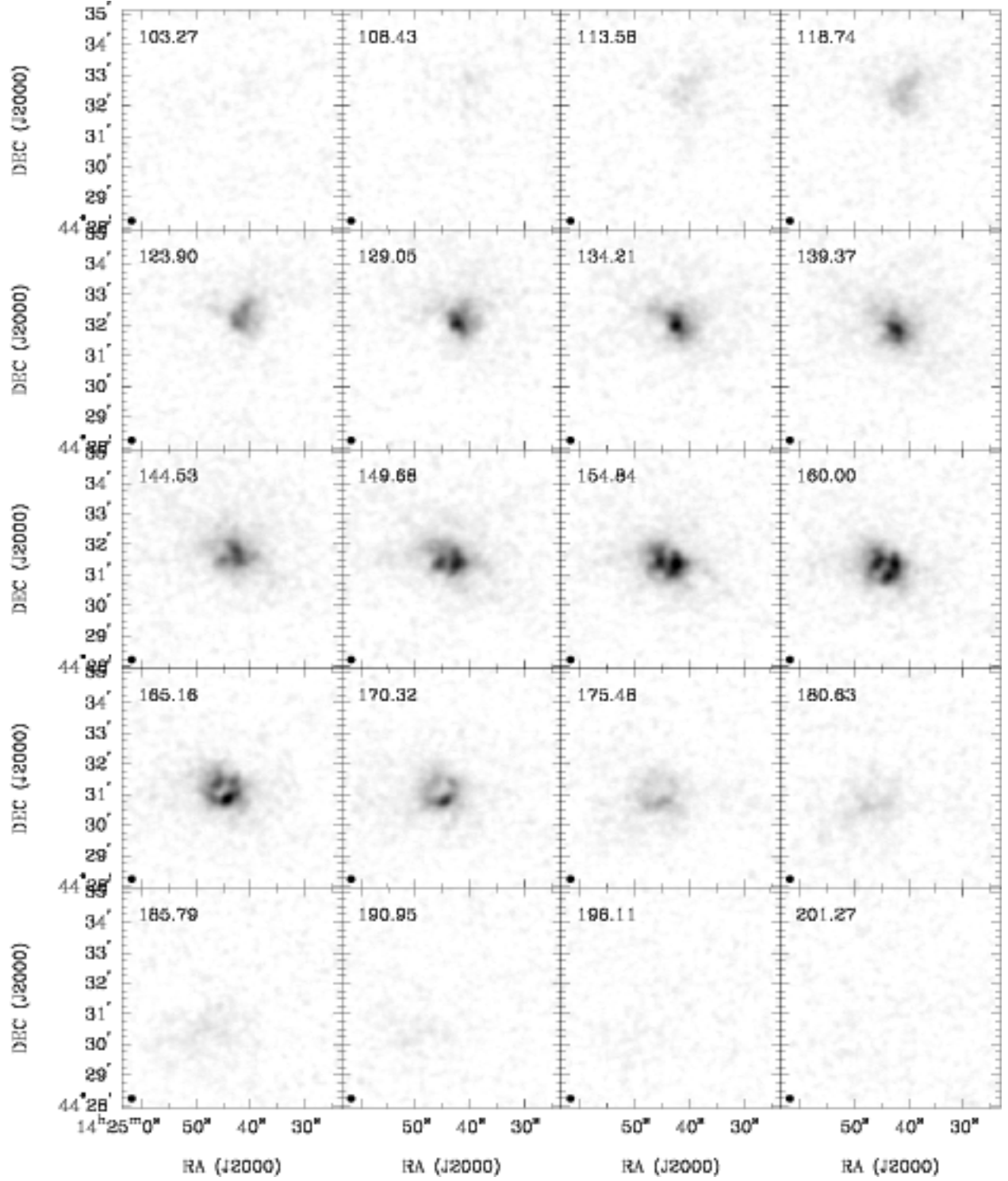


Fig. 31.— **DDO 190**: Channel maps based on the natural-weighted cube (grayscale range: -0.02 to $27.5 \text{ mJy beam}^{-1}$). Every channel is shown (channel width 2.6 km s^{-1}) and each map has the same size as the moment maps in the following panels.

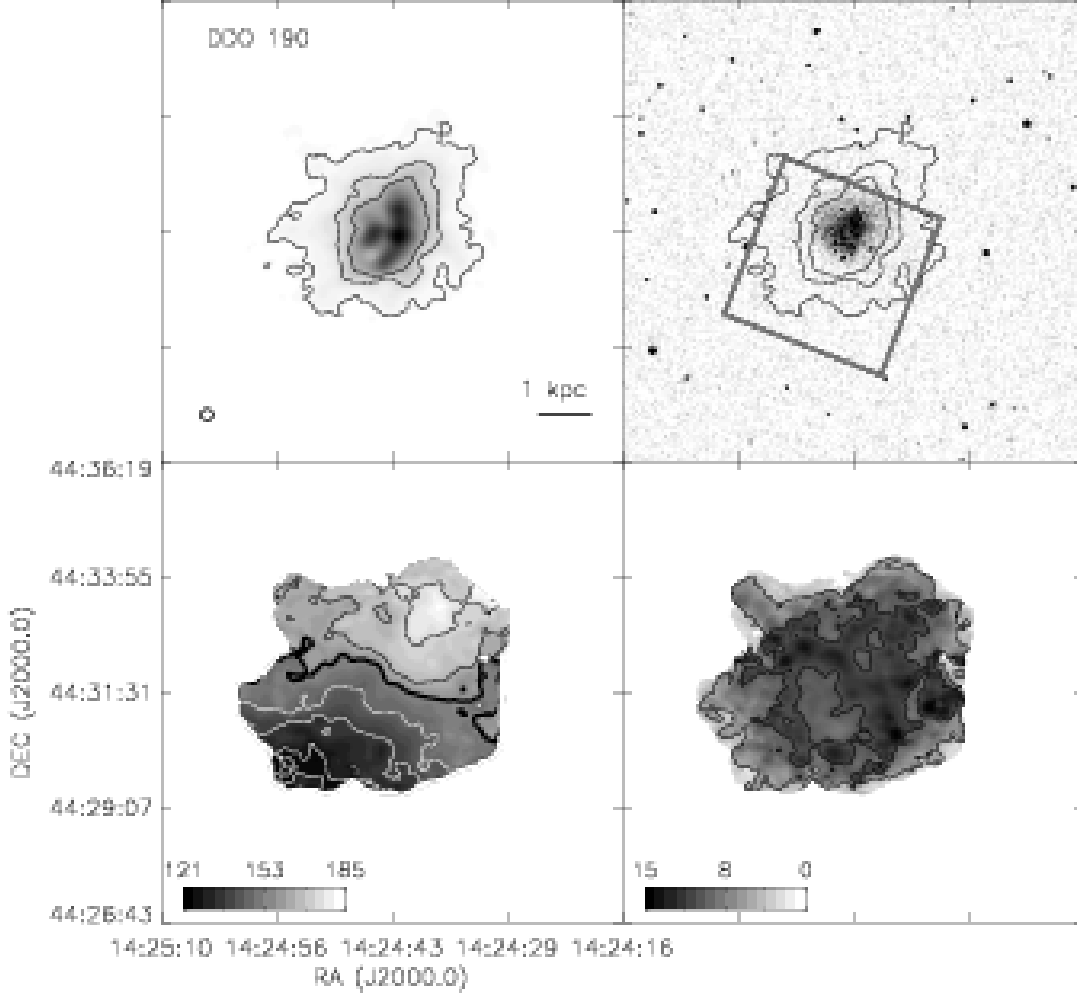


Fig. 31.— continued. *Top left:* The integrated H I intensity map for DDO 190. The grayscale covers a range from 1×10^{19} to $3.6 \times 10^{21} \text{ cm}^{-2}$ with contours of 1×10^{20} , 5×10^{20} , and $1 \times 10^{21} \text{ cm}^{-2}$. *Top Right:* An optical g-band image from the SDSS with the same column density contours overlaid. The HST ACS footprint is the field covered by the ANGST survey. *Bottom Left:* The H I velocity field. Black contours (lighter gray scale) indicate approaching emission, white contours (darker gray scale) receding emission. The thick black contour is the central velocity ($v_{cen} = 148.8 \text{ km s}^{-1}$) and the isovelocity contours are spaced by $\Delta v = 10 \text{ km s}^{-1}$. *Bottom Right:* The H I velocity dispersion. Contours are plotted at 5 and 10 km s^{-1} . Colorbars are in units of km s^{-1} .

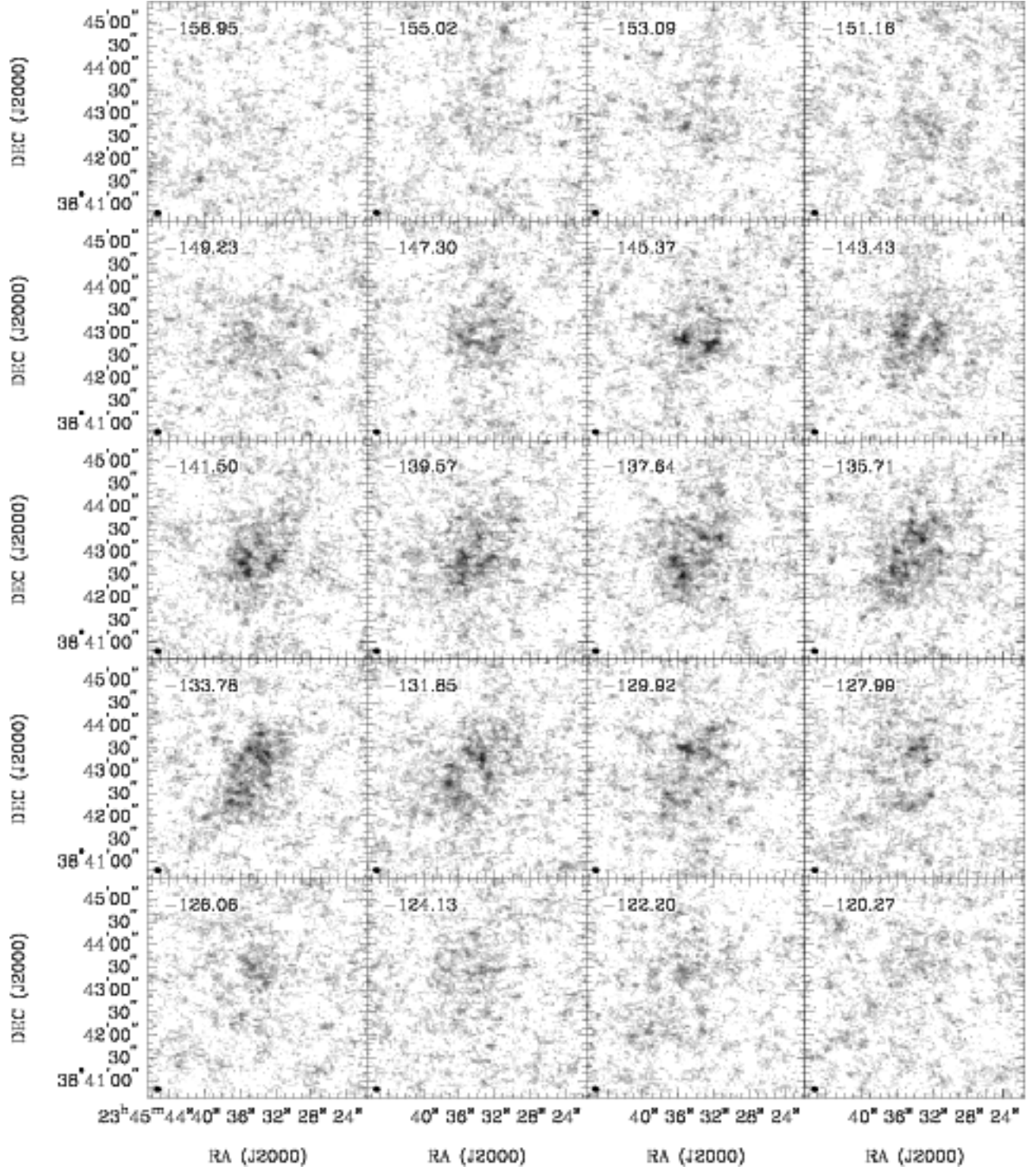


Fig. 32.— **KKH 98**: Channel maps based on the natural-weighted cube (grayscale range: -0.02 to $8.4 \text{ mJy beam}^{-1}$). Every second channel is shown (channel width 0.6 km s^{-1}) and each map has the same size as the moment maps in the following panels.

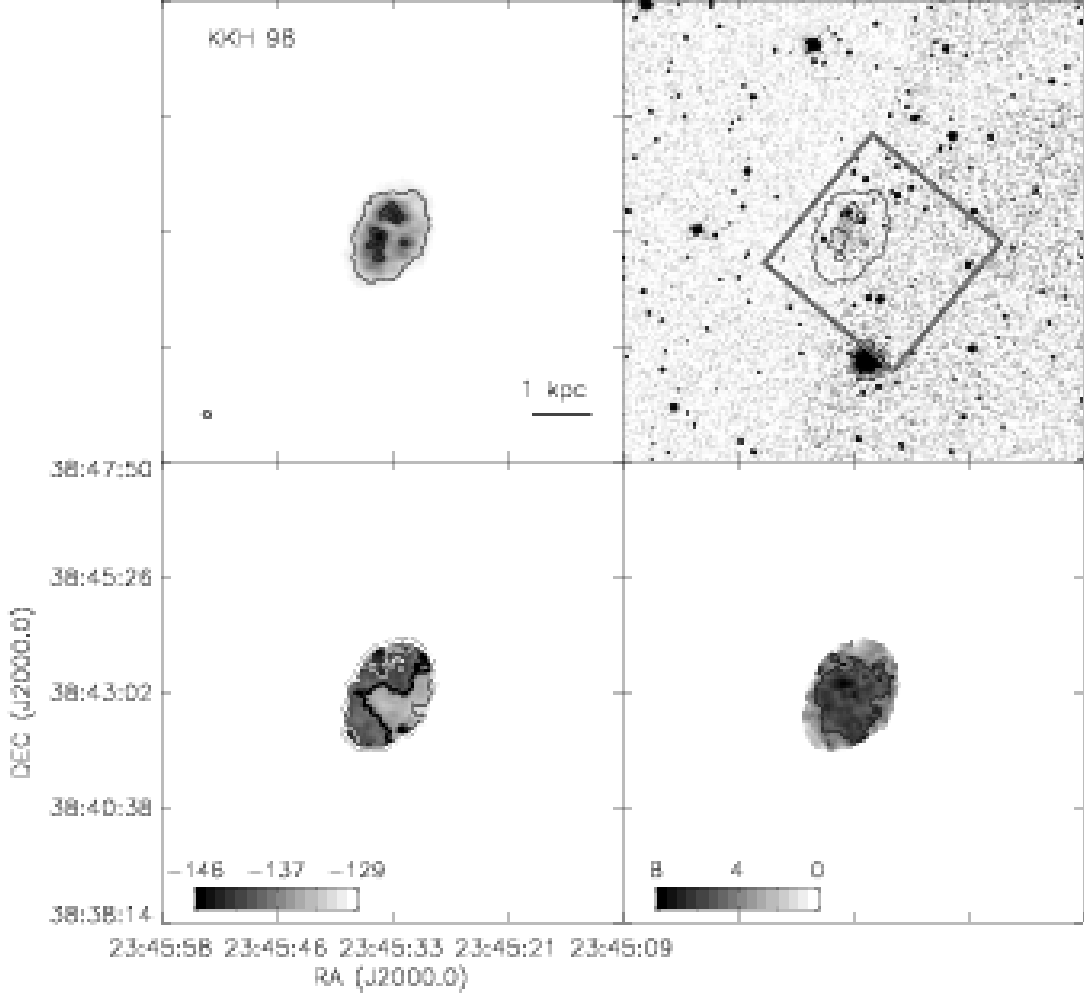


Fig. 32.— continued. *Top left:* The integrated H I intensity map for KKH 98. The grayscale covers a range from 1×10^{19} to $7.7 \times 10^{20} \text{ cm}^{-2}$ with contours of 1×10^{20} and $5 \times 10^{20} \text{ cm}^{-2}$. *Top Right:* An optical g-band image from the SDSS with the same column density contours overlaid. The HST ACS footprint is the field covered by the ANGST survey. *Bottom Left:* The H I velocity field. Black contours (lighter gray scale) indicate approaching emission, white contours (darker gray scale) receding emission. The thick black contour is the central velocity ($v_{\text{cen}} = -137.8 \text{ km s}^{-1}$) and the isovelocity contours are spaced by $\Delta v = 5 \text{ km s}^{-1}$. *Bottom Right:* The H I velocity dispersion. A contour is plotted at 5 km s^{-1} . Colorbars are in units of km s^{-1} .